A design study for a COBRA upgrade to investigate the $2\nu\beta\beta$ decay of ^{116}Cd into the first excited state

Diplomarbeit
Zur Erlangung des akademischen Grades
Diplom-Physiker

vorgelegt von
Wiebke Tenner
geboren in Anklam

Institut für Kern- und Teilchenphysik
Technische Universität Dresden
2010

1. Gutachter: Prof. Dr. Kai Zuber
2. Gutachter: Jun.-Prof. Dr. Arno Straessner
Eingereicht am: 29. September 2010

I hereby declare that I have created this work completely on my own and used no other sources or tools than the ones listed, and that I have marked any citations accordingly.

Hiermit versichere ich, dass ich die vorliegende Arbeit selbständig verfasst und keine anderen als die angegebenen Quellen und Hilfsmittel benutzt, sowie Zitate kenntlich gemacht habe.

$\overline{Ort,\ Datum\ der\ Abgabe}$ $\overline{Unterschrift}$

Abstract

Double beta decays are among the rarest processes in the universe, having half lives of 10^{19} years.
The COBRA experiment, which is currently in the R&D phase, has the aim to detect neutrinoless double beta decays with expected half lives of more than 10^{28} years by using CdZnTe semiconductor crystals.
This thesis is a design study of a new detector component for the COBRA prototype apparatus, aiming to enhance the sensitivity for the detection of neutrino accompanied double beta decays into excited states. Scintillation detectors were investigated as possible solution. In order to design a scintillator upgrade, which meets the demands of the experiment as best as possible, three different Monte Carlo simulations were written. Two of these simulations help to choose the optimal crystal size and the scintillator readout electronics. The third one implemented a designed COBRA upgrade with CsI:Tl into the COBRA simulation framework VENOM. Monte Carlo studies of this upgrade demonstrated that using CsI:Tl for the COBRA experiment is difficult. The cosmogenic ^{134}Cs is expected to be the main background of CsI:Tl and reduces the detection efficiency for the neutrino accompanied decay of ^{116}Cd into the first excited state by one order of magnitude.

Überblick

Doppel-Beta-Zerfälle sind mit Halbwertszeiten von über 10^{19} Jahren, einige der seltensten stattfindenden Prozesse.
Das Experiment COBRA hat den Nachweis der, mit erwarteten Halbwertszeiten von 10^{28} Jahren, noch selteneren neutrinolosen Doppel-Beta-Zerfälle zum Ziel. Das Experiment benutzt CdZnTe Halbleiterdetektoren und befindet sich gegenwärtig in der Entwicklungsphase.
Der Gegenstand dieser Diplomarbeit ist die Entwicklung eines Konzeptes für eine Erweiterung des COBRA-Aufbaus mit erhöhter Photonen-Nachweis-Effizienz. Ziel dieser Erweiterung soll der Nachweis des neutrinobegleiteten Doppel-Beta-Zerfalls von ^{116}Cd in den ersten angeregten Zustand sein. Dafür wurde eine intensive Recherche zu den erhältlichen Szintillationsdetektoren durchgeführt und drei Monte Carlo Simulationen entwickelt. Zwei dieser Simulationen dienten der Bestimmung der optimalen Szintillatorgrösse und der passenden Szintillatorauslese. Bei der dritten Simulation wurde die Geometrie der geplanten Erweiterung in das COBRA Simulationprogramm VENOM implementiert und Zerfallsereignisse im Aufbau simuliert.
Es zeigte sich, dass das favorisierte CsI:Tl mit dem kosmogen aktiviertem ^{134}Cs einen radioaktiven Untergrund hat, der die Messung des gesuchten Zerfalls behindert.

Contents

Chapter 1

Introduction

Neutrino physics plays a fundamental role in modern physics and cosmology. Especially the research of neutrinoless double beta decay is of importance, as it could be the gold plated channel to determine the fundamental character, being Dirac or Majorana type, and the absolute mass scale of the neutrino [1]. This lightest elementary particle was introduced in the standard model of particle physics ad hoc as massless, which was disproved by the SuperKamiokande and SNO experiments, showing that neutrino flavour eigenstates can oscillate and correspondingly, the neutrino mass eigenstates have different masses. During the last ten years various neutrino oscillation experiments determined the mass-square differences of the three neutrino mass eigenstates Δm^2_{ij} to be about $7.6 \times 10^{-5}\,\mathrm{eV}^2$ and $2.4 \times 10^{-3}\,\mathrm{eV}^2$ [2], leading to different possible neutrino mass hierarchies. The neutrinoless double beta decay can exist, if the neutrino is a Majorana particle and its measurement could provide access to the effective Majorana neutrino mass $\langle m_{\nu_e} \rangle$. Its observation will depend on the measured half live, the phase space and the nuclear matrix element.

The COBRA collaboration is investigating various double beta decay isotopes, like the promising ^{116}Cd and ^{130}Te. Additionally the CdZnTe detectors used by COBRA contain ^{106}Cd, which is one of only 6 known $\beta^+\beta^+$ isotopes [3] and can become important for identifying the underlying physics mechanism of double beta decay.
For testing the nuclear matrix element calculations, also measurements of neutrino accompanied double beta decays into the ground and excited states are necessary.

The CdZnTe detectors used by COBRA are $1\,\mathrm{cm}^3$ small semiconductor crystals with a low gamma ray detection efficiency, leading to a correspondingly low detection efficiencies for $\beta\beta$-decays into excited states. The aim of this thesis is to design a COBRA upgrade with improved detection efficiency for $2\nu\beta\beta$-decays into first excited states. These can be done by expanding the current COBRA apparatus with scintillation detectors, providing they are suitable for a low background level experiment.

The particle detection with scintillation detectors is therefore discussed in chapter 4—"Scintillation detectors", after a short introduction into the physics of double beta decays in chapter 2—"Neutrino physics" and into the COBRA experiment in chapter 3—"The COBRA experiment", which explains the demands on a COBRA scintillator upgrade. In chapter 5—"Scintillator upgrade", the work of this thesis will be explained. Two developed simulations, helping to determine the size and kind of scintillation detector, will be presented. In the following, the development and analysis of a Monte Carlo simulation of the designed scintillator upgrade for evaluating the suitability of this upgrade is discussed. A future outlook follows.

Chapter 2

Neutrino physics

The neutrino is the lightest elementary particle. It has no electric charge and is interacting so weakly, that several thousand light years of lead would be necessary for stopping a neutrino beam. On Earth, neutrino fluxes of the order of 10^{10} per cm^2 and second are passing through, without anyone but a few neutrino oscillation experiments noticing. Neutrinos provide unique information about the present processes in the centre of our sun, do announce supernovae and can supply more knowledge about the interior of our earth. However, neither their actual mass, nor their actual particle nature, being Majorana of Dirac, is known yet.

The neutrino was postulated in 1930 by Pauli [4], explaining the seemingly missing energy in nuclear beta decay instead of dismissing the conservation of energy. In 1953 the neutrino was first detected by Cowan and Reines [5], using a nuclear reactor as neutrino source. In the Standard Model of Particle Physics the neutrino was introduced as massless fermion, having three flavours (e, μ and τ) and coupling only to weak left-handed charged currents. More than ten years after its first detection, Davis [6] started the solar neutrino puzzle by detecting only one third of the expected ^{8}B neutrino flux from the sun, to call either his experiment, the Solar Standard Model or the understanding of neutrinos into question. This problem was solved not until 2001 by the measurements of the SNO experiment, confirming Davis's experiment and the Solar Standard Model, by proving the neutrino flavour oscillation and therefore the existence of non-zero neutrino masses. The oscillation experiments are only sensitive the mass-square differences of the neutrino mass eigenstates Δm^2_{ij} and can neither determine the absolute

mass scales nor the neutrino mass hierarchy.
The electron neutrino mass m_{ν_e} could be determined, by investigating the end point energy of the tritium beta decay spectrum, like the Katrin experiment is doing currently.
However, this cannot determine whether the neutrino is a Majorana particle and therewith its own antiparticle or not. In the short term, the measurement of the neutrinoless double beta decay might answer this question and determine the effective neutrino mass $\langle m_{\nu_e} \rangle$.

2.1 Double beta decay

A second order process to the beta decay is the double beta decay. It can be regarded as two subsequent β-decays via a virtual intermediate state.
The double beta decay was first discussed by Goeppert-Mayer in 1935, predicting half lives of more than 10^{17} years [7]. The double beta decay is a nuclear process, changing the proton number Z by two units, while leaving the atomic mass A unchanged. It is allowed in the Standard Model of Particle Physics and can appear with β^-, β^+ and electron capture (EC) processes in four different decay modes:

$$(Z, A) \rightarrow (Z + 2, A) + 2\bar{\nu} + 2\beta^- \qquad [2\nu\beta^-\beta^-] \tag{2.1}$$
$$(Z, A) \rightarrow (Z - 2, A) + 2\nu + 2\beta^+ \qquad [2\nu\beta^+\beta^+] \tag{2.2}$$
$$e^- + (Z, A) \rightarrow (Z - 2, A) + 2\nu + \beta^+ \qquad [2\nu\beta^+EC] \tag{2.3}$$
$$2e^- + (Z, A) \rightarrow (Z - 2, A) + 2\nu \qquad [2\nu ECEC] \tag{2.4}$$

According to the Bethe-Weizsäcker formula, the nucleus mass $m(Z, A) \propto const. + aZ + bZ^2 + \delta_p$ only depends on Z for a given atomic number A and forms a parabola. The pairing energy δ_p for isotopes with odd A is zero, leading to a single parabola with a single stable isotope. The mass parabola splits into two parabolae for even A, separated by an energy of $2\delta_p$ with $\delta_p = \pm 11.46\,\mathrm{MeV}/A^{1/2}$ for odd-odd or even-even numbers of neutrons and protons. Here, the double beta decay nuclei are positioned at the lower parabola, as is shown in figure 2.1. The $\beta\beta$-decay is allowed for nuclei, where the mass of the ground state is larger than the mass of the daughter nucleus: $m(Z, A) > M(Z \pm 2, A)$. As the decay times of single beta decay are much shorter than these of double beta decays, the single beta decay must be forbidden or at least strongly suppressed (case of ^{48}Ca) to make $\beta\beta$-decays visible. For 35 known isotopes the single beta decay is forbidden, because of

$m(Z, A) < m(Z \pm 1, A)$, while the double beta decay is allowed. These are isotopes with even neutron number N and even proton number Z.

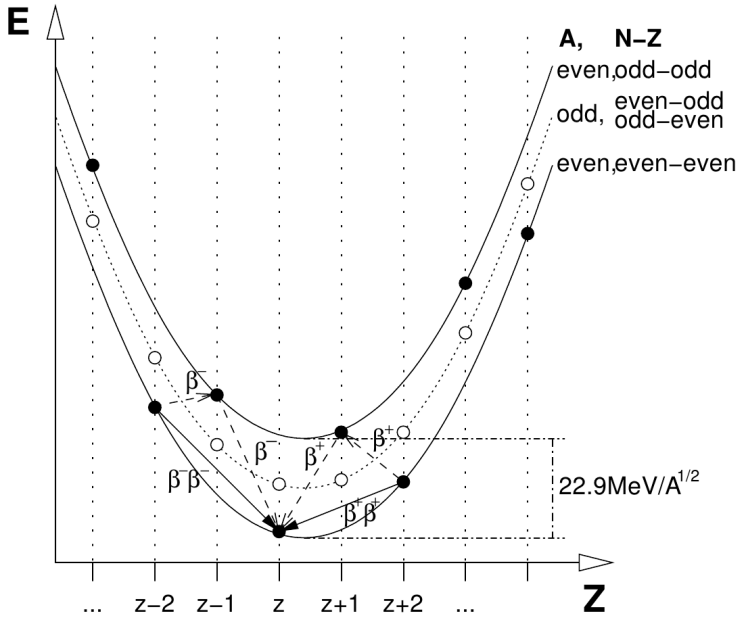

Figure 2.1: The mass parabola for isobaric nuclei are shown, with the single parabola for odd number of nucleons A (dotted line) and the double mass parabola for nuclei with even A (solid lines). Double beta decay isotopes are even-even nuclei (lower parabola), which energetically cannot decay via single beta decay into odd-odd nuclei (upper parabola.) Taken from [8].

$2\nu\beta^+\beta^+$-decays are energetically allowed for only 6 nuclei, as the Coulomb barrier reduces their Q-value by $4m_e$. $\beta^+\beta^+$-decays are always accompanied by $2\nu\beta^+EC$ and the difficult to detect $2\nu ECEC$.

The half lives of double beta decays depend on the phase space $G^{2\nu}$ and the Gamow-Teller and Fermi nuclear matrix elements M as follows:

$$(T^{2\nu}_{1/2})^{-1} = G^{2\nu}(Q, Z) \cdot |M^{2\nu}_{GT} - M^{2\nu}_{F}|^2 \tag{2.5}$$

The phase space of double beta decays and therefore also the half live depends on the Q-value with: $T^{2\nu}_{1/2} \propto G^{2\nu}(Q, Z) \propto Q^{11}$.
The sum energy spectra of the electrons is a continuous spectra, showing a maximum at about $0.32 \times Q$.

Ground states of even-even nuclei have spin 0 and parity +. Transitions between ground states are two subsequent Gamow-Teller transitions with a (1^+) intermediate state. So far, ground state transitions have been observed for about a dozen isotopes.
For some isotopes, the Q-value is large enough to allow the transition into excited states. The subsequent deexcitation of the excited daughter nucleus into the ground state, leads to the emission of one or more gamma rays. The transitions can occur into 0^+ or 2^+ excited states and are suppressed due to a lower Q-value. Transitions into 2^+ are further suppressed [1, 9].

2.2 Neutrinoless double beta decay

In 1939 Furry proposed a double beta decay without the emission of two neutrinos [10]. This neutrinoless double beta decay is only possible if the neutrino has non-zero mass and is a Majorana particle (neutrino = antineutrino). In this process, a neutron emits a right-handed antineutrino $\bar{\nu_e}$, which is absorbed at the next vertex as a left-handed neutrino ν_e.

$$n \rightarrow p + e^- + \bar{\nu_e} \tag{2.6}$$

$$\nu_e + n \rightarrow p + e^- \tag{2.7}$$

Only a massive Majorana (anti)neutrino, being not purely right-handed, can interact via its small admixture ($\propto m_\nu/E$) of left-handed helicity with the second neutron, which is schematically shown in figure 2.2.

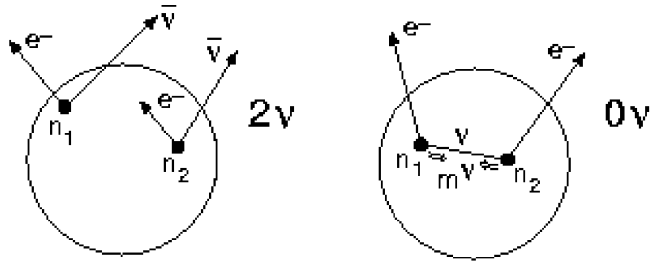

Figure 2.2: Schematic drawing of $2\nu\beta\beta$ and $0\nu\beta\beta$ decay.

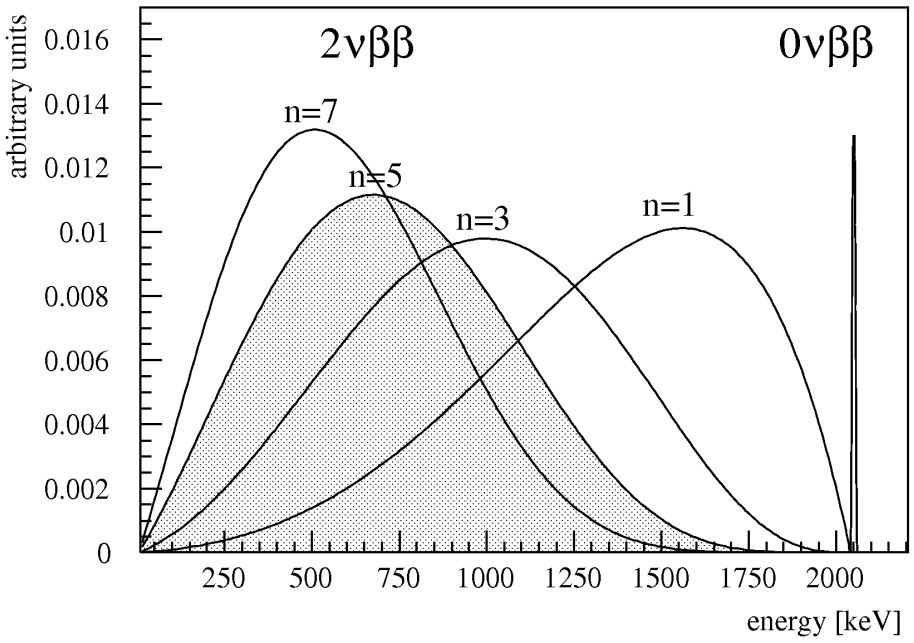

Figure 2.3: Double beta electron sum spectrum of neutrinoless, neutrino-accompanied (n=5) decay and decay modes with Majorons in the final state (n=1, n=3, n=5).

With no neutrinos in the final state, the electrons carry away the hole Q-value, leading to an expected monoenergetic electron sum energy. This process violates the lepton number conservation and is not allowed in the Standard Model. The $0\nu\beta\beta$-decay can be caused by several kinds of interaction beyond the Standard Model, including models with non-Standard-Model particles, like Majorons, in the final state. The expected electron sum energy spectra of $2\nu\beta\beta$, $0\nu\beta\beta$ and $0\nu\beta\beta\chi$ decays accompanied by non standard model particles are shown in figure 2.3.

The half-life of $0\nu\beta\beta$-decays determines the effective Majorana neutrino mass $\langle m_{\nu_e} \rangle$ via:

$$(T^{0\nu}_{1/2})^{-1} = G^{0\nu}(Q, Z) \cdot |M^{0\nu}_{GT} - M^{0\nu}_{F}|^2 \cdot \left(\frac{\langle m_{\nu_e} \rangle}{m_e} \right)^2 \qquad (2.8)$$

with the phase space $G^{0\nu}$ and the Gamow-Teller and Fermi nuclear matrix elements M. The effective Majorana neutrino mass $\langle m_{\nu_e} \rangle$ is the sum of the squared mixing matrix element U_{ei} weighted mass eigenvalues

m_i:

$$\langle m_{\nu_e} \rangle = |\sum_i U_{ei}^2 m_i| \tag{2.9}$$

The decay rate of $0\nu\beta\beta$-decays scales only with Q^5 in comparison to the Q^{11} dependence for $2\nu\beta\beta$-decays [1].

2.3 Experimental status

The double beta decay studies were first made with geochemical methods, searching for an excess of $\beta\beta$-decay products in old ores. These inclusive method is not able to distinguish $2\nu\beta\beta$ and $0\nu\beta\beta$-decays.

Exclusive experiments on $0\nu\beta\beta$ can distinguish both decay modes and are of two different concepts:

$$source = detector$$
$$source \neq detector$$

Calorimeters follow the $source = detector$ concept. They can achieve good energy resolutions, detect the sum of both electron energies, have a very high detection efficiency and can improve the sensitivity by increasing the detector material.
Tracking detectors are representative for the $source \neq detector$ concept. Their advantage is the possibility of identifying separately both electrons, which improves the background level. The drawback is a low detection efficiency and the circumstance that electrons loose already a fraction of their energy in the source material, before leaving it. Tracking detectors achieve also poor energy resolution in comparison with calorimeters. The source material has often the form of thin foils to improve the detection efficiency, but also complicate the increase of the mass of the source material.

About a dozen $2\nu\beta\beta$-decays have been measured yet, using both detector concepts. Two of them, measured with the NEMO-3 detector ($source \neq detector$) are the for COBRA relevant half lives of ^{130}Te ($T_{1/2}^{2\nu} = 7.0 \pm^{1.0}_{0.8} (stat.) \pm^{1.1}_{0.9} (sys.) \times 10^{20}$ years) and ^{116}Cd ($T_{1/2}^{2\nu} = 2.88 \pm 0.04 \pm 0.16 \times 10^{19}$ years) [11].

The $2\nu\beta\beta$-decay to the first (2^+) excited state has not been measured for ^{116}Cd yet. The experimental limit for this decay mode is $T^{2\nu}_{1/2} > 2.4 \times 10^{21}$ years (90% C.L.) and expected half lives were reported as $T^{2\nu}_{1/2} = 2.0 \times 10^{23}$ years [12]. The neutrino accompanied double beta decay is of special interest for the testing of nuclear matrix element calculations. Transitions to ground and excited states (0^+, 2^+) can probe different aspects of matrix element calculations.

A variety of experiments is investigating different promising double beta isotopes. Especially isotopes with already high natural abundance, with expected low half lives, due to a high Q-value and a large nuclear matrix element are the most promising isotopes for a first double beta decay detection. Calorimetric experiments used so far ^{48}Ca, ^{76}Ge, ^{116}Cd and ^{130}Te. The spectroscopic detectors NEMO-3 and ELEGANT investigated isotopes with high Q-value like ^{82}Se, ^{100}Mo and ^{116}Cd.

The best result for the neutrinoless double beta decay was so far achieved by the Heidelberg-Moscow collaboration, presenting a half-live limit of $T^{0\nu}_{1/2} > 1.9 \times 10^{25}$ years at 90 % C.L [13]. A subgroup of this collaboration claimed the observation of the $0\nu\beta\beta$ decay of ^{76}Ge with $T^{0\nu}_{1/2} = (0.69 - 4.18) \times 10^{25}$ years [14].

Currently, there are a lot of double beta decay experiments under progress, some like GERDA already have started or will soon start data taking to prove or disprove the Heidelberg-Moscow claim.
The two large scale Ge-experiments are GERDA and MAJORANA. GERDA plans to use 18 kg of high-purity enriched ^{76}Ge in phase one (already mentioned) and to add another 20 kg in the next phase.
MAJORANA will use 60 kg Ge detectors. Both experiments plan to merge for a future ton-scale experiment by using the best developed and tested techniques from the former experiments.
CUORE is an expansion of CUORICINO, currently under construction. They will use nearly one ton of TeO crystals for investigating the $0\nu\beta\beta$ decay of ^{130}Te.
The SNO+ collaboration (also starting soon) is planning to use 0.1 %Nd in their one kton scintillation detector.
Other planned experiments are for instance CANDLES (^{48}Ca), MOON(^{82}Se), COBRA (^{116}Cd), EXO (^{136}Xe) and SuperNEMO (^{82}Se) [15].

Chapter 3

The COBRA experiment

COBRA, being an acronym for **C**dZnTe-**0**ν-Double-**B**eta-Decay-**R**esearch-**A**pparatus, is a double beta decay experiment, using CdZnTe semiconductor crystals. It was founded in 2001 by K. Zuber and is currently in the R&D phase, hosted with a prototype apparatus at the Laboratori Nazionali del Gran Sasso (LNGS). The COBRA experiment investigates the neutrinoless double beta decay of nine different double beta decay isotopes. Double beta decays, being extremely rare processes, lead to very small event rates in the order of events per day for $2\nu\beta\beta$ decays and even expected events per year in case of $0\nu\beta\beta$ decays in one kg source material. These are covered by background rates in the order of events per second. Accordingly, the background reduction is essential for all double beta experiments.

This chapter will explain the concept of the COBRA experiment and the structure of the current prototype set-up, before motivating the design of a COBRA upgrade with enhanced efficiency for gamma ray detection.

3.1 CdZnTe

COBRA is currently the only double beta decay experiment using CdZnTe semiconductor crystals. These crystals are simultaneously source and detector, leading to excellent detection efficiency for double beta decays.

CdZnTe (CZT) contains nine double beta decay isotopes, which are listed in table 3.1 with their natural abundance, the possible decay mode and the Q-value.

Isotope	Q (keV)	nat. ab. (%)	decay mode
^{64}Zn	1096	48.6	$EC/EC, EC/\beta^+$
^{70}Zn	1001	0.6	$\beta^-\beta^-$
^{106}Cd	2771	1.3	$EC/EC, EC/\beta^+, \beta^+\beta^+$
^{108}Cd	231	0.9	EC/EC
^{114}Cd	534	28.7	$\beta^-\beta^-$
^{116}Cd	2805	7.5	$\beta^-\beta^-$
^{120}Te	1722	0.1	$EC/EC, EC/\beta^+$
^{128}Te	868	31.7	$\beta^-\beta^-$
^{130}Te	2529	33.8	$\beta^-\beta^-$

Table 3.1: Double beta isotopes of relevance for the COBRA experiment, with Q-value, natural abundance and possible decay mode given according to Kiel [8].

The most promising isotopes for the COBRA experiment are ^{116}Cd and ^{130}Te. Their decays have a high Q-value, which is favourable for the expected event rate as it varies with Q^5 for $0\nu\beta\beta$. Additionally, ^{116}Cd has, with 2805 keV, an endpoint energy well over the highest occurring natural gamma line at 2614 keV from the ^{232}Th decay chain [16]. The Q-value of ^{130}Te is between this line and its Compton edge. This leads to a reduced background for their expected $0\nu\beta^-\beta^-$ ground state transitions. A natural high abundance of ^{130}Te provides also relatively high source mass, already without using isotopically enriched material. CZT contains also ^{106}Cd, which is one of only 6 known $\beta^+\beta^+$ decay isotopes.

CdZnTe crystals are intrinsic II-VI semiconductor crystals with a zinc blende structure. They are produced by the High Pressure Bridgman Method with low intrinsic contamination, but also with a limited detector size of a few cm^3. This requires a modular design for reaching high source mass, for which the collaboration investigates the advantages of a coincidence analysis. Owing to a large band gap of 1.6 eV, CZT detectors can be operated at room temperature, which avoids extensive cooling.

Currently, different CZT detector designs are under investigation. These are coplanar grid CZT detectors, which will be discussed further on and two different pixelated designs, which show promising possibilities of a very effective background reduction. For the recent activities

of the collaboration see [17].

3.2 Background shielding

Double beta decay experiments try to identify double beta decays, by detecting the decay products. These are two electrons for expected ground state transitions and one or more additional gamma quanta for possible transitions into excited states. The neutrinos, emitted at $2\nu\beta\beta$ decays, cannot be detected. Other radioactive decays decrease the possibility of identifying double beta decays. Owing to the energy resolution of the detector, it is not possible to distinguish between the expected signal and background events, which deposit a similar energy in the CZT detector. So, especially decays with continuous decay spectra can cover the energy region of interest and overlap the possible signals. Depending on the detector technology, the pile up of background, that means the detection of two or more background events in the same readout time, might not be distinguished from single events with the same energy deposition.

For a flat background in the regarded region of energy, the half-life sensibility for double beta decays scales with experimental parameters as

$$T_{1/2}^{0\nu} \propto a \cdot \epsilon \cdot \sqrt{\frac{M \cdot t}{\Delta E \cdot B}} \tag{3.1}$$

with a and ϵ being the natural abundance and the detection efficiency of this decay. The other parameters are the mass of the source M, the measuring time t, the energy resolution ΔE and the detected background in the energy region of interest B. Besides optimizing the detection efficiency and detector resolution, increasing the natural abundance of the source isotope and the amount of the detector material, an intensive reduction of the background rate is unavoidable for the success of double beta decay experiments.
The main sources of background events in the detector are cosmic radiation, anthropogenic and primordial radionuclides and the intrinsic background. They are further discussed in the following section.

Cosmic radiation consists mainly of high energetic protons. By penetrating the upper atmosphere, they produce a spectrum of secondary particles. Only a reduced flux of these secondary particles reaches the earth at sea level, consisting mainly of muons, neutrons, electrons, protons and pions with relative ratios of about

1420:480:340:13:1 [18].
In contrast to the other secondary cosmic rays, muons cannot be stopped by a few meters of shielding material. The muon flux can only be reduced by going deep underground, where it is for instance reduced by 4 orders of magnitude in the 3500 meters of water equivalent (mwe) deep LNGS. There the atmospheric muons with energies of about 10 GeV up to a few TeV can interact either directly with the detector material or can produce tertiary neutrons near the detector. Their contribution to the background rate can be further reduced with an active muon veto. A more serious impact on low-level experiments have cosmogenic isotopes. These can be produced in materials, which are exposed to cosmic radiation. (n, γ) interactions or spallation processes with the constituent isotopes can produce various radionuclides. Radionuclides with half lives of month or years, being still present in the components, long after these have been installed underground, can be a major problem.

Primordial radioisotopes are isotopes with half-lives of more than 10^9 years, being produced before the formation of the earth. Isotopes from the ^{238}U, ^{235}U and ^{232}Th decay chains and ^{40}K are most likely to find. They are in the laboratory surrounding rock and in smaller or larger concentrations in all detector components. This requires shielding of the detector from the surrounding background decays, where primary the produced neutrons and gamma rays must be shielded. Also, a thoughtful selection of the detector and shielding material and a subsequent careful handling of these, in order to prevent a subsequent contamination of the surfaces, is necessary. With the highest prominent gamma line of 2.614 keV from the ^{232}Th decay chain, these background components are beyond the most interesting Q-values of double beta decays, but can disturb the experiments nevertheless. The noble gas ^{222}Rn is part of the ^{238}U decay chain and can leak out of the surrounding rock, can accumulate in the laboratory air and can diffuse into the experimental set-up. It decays under the emission of a 5.5 MeV alpha particle and is therefore a problem for double beta decay experiments. Additionally, its decay products are also radioactive, can attach themselves to surfaces near the detector and can increase the background level further on [18].

Anthropogenic radioisotopes are mainly fallout from nuclear weapons testing and nuclear accidents, although they can also exist naturally in lower concentrations. Materials, being produced before nuclear weapons testing and especially the

Chernobyl disaster in 1986 can have lower contamination of these isotopes. A prominent representative of the anthropogenic radioisotopes is ^{137}Cs, which leads the emission of a gamma line at 662 keV, owing to the deexcitation of ^{137m}Ba [18].

Intrinsic background for $0\nu\beta\beta$ decay experiments are always the non-avoidable $2\nu\beta\beta$ decays. Thus, even in an experiment, with no contamination of the source material and no external background, the endpoint of the $2\nu\beta\beta$ decay energy spectrum is, due to the finite energy resolution of the detector, always a background of possible $0\nu\beta\beta$ decays.

The detected count rate of the just described background sources can be reduced with a multistage shielding and careful material selection. A COBRA prototype apparatus with a multistage shielding has been established in the LNGS to investigate the major experimental issues of operating CZT detectors under low background conditions. This set-up will be described now.
The current COBRA set-up consist of a neutron, a lead and a copper shield and the CZT detectors are hosted on Delrin holders in a copper case, called Nest. It is shown in figure 3.1 and will be explained in the following.

Gran Sasso: The Gran Sasso mountain shields the experiment with about 1400 m of rock against cosmic rays. This corresponds to about 3500 mwe and reduces the muon flux to about one muon per m^2 per hour in the laboratory. This is no relevant background contribution for the current stage of the prototype set-up, making the installation of a muon veto not necessary yet.
Although the Gran Sasso rock shields cosmic rays, it also contains U and Th, whose decays contribute to the experimental background. Besides the emission of gamma rays and neutrons, which can be shielded, the escape of ^{222}Rn and ^{220}Rn is a more serious background source. Radon activities of about 35 Bq/m^3 were measured in the laboratory cavity [20].

Neutron shield: Neutrons in the laboratory hall are produced by spontaneous fission or (α, n)-reactions of U and Th in the rock. Neutrons are also produced by muon interactions with the rock and lead shield. Due to a high thermal neutron capture cross section of $20 \cdot 10^5$ kb of ^{113}Cd, which is contained with a natural abundance of 12 % in Cd, neutrons can be a severe background component for COBRA. They are shielded by 7 cm of borated polyethylene. Therein neutrons are moderated by elastic scattering with

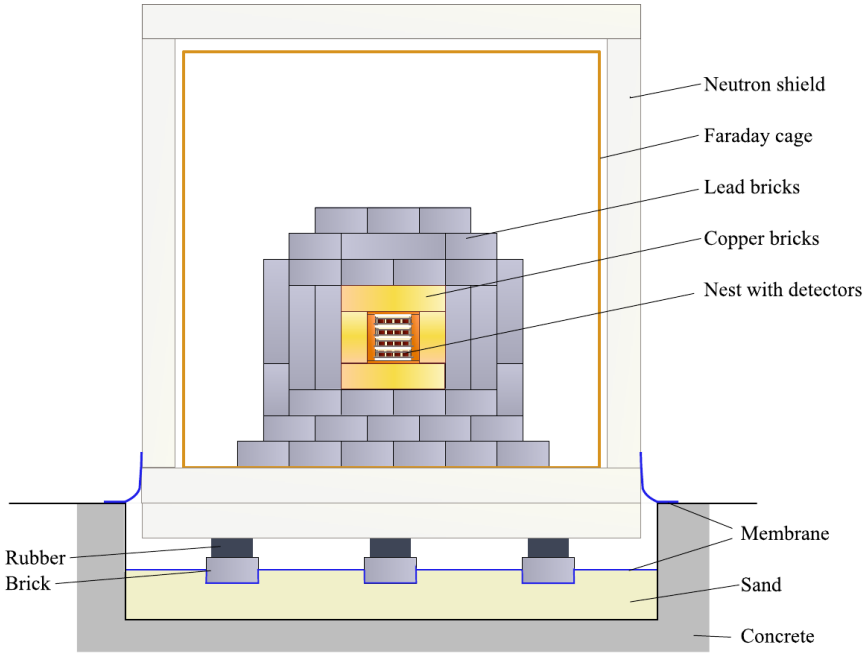

Figure 3.1: Current COBRA prototype set-up at the LNGS, with neutron shield, Faraday cage, lead and copper shield and CZT inside a copper case, called Nest [19].

protons and are subsequently captured by $^{10}\mathrm{B}(n,\alpha)^{7}\mathrm{Li}$ reactions [21].

Faraday cage: The Faraday cage is a $2\times1\times1\,\mathrm{m}^3$ copper box, inside the neutron shield. It is hosting the further shielding assembly and the charge sensitive preamplifier outside the lead shield. It was constructed, to minimize the Rn concentration of the inner set-up, but is not working satisfying and will be improved in the future.

Lead and copper shield: The inner set-up is hosted in the Faraday cage, surrounded by 10 cm of copper and a 20 cm lead layer.
Lead, with its high density of about $11\,\mathrm{g/cm}^3$ and its large atomic number Z of 82, is well qualified for the absorption of high energetic gammas. It also has a low cross section for thermal neutron capture and cosmogenic interaction, but contains the radioisotope ^{210}Pb. Commercial lead can be acquired in different low activity qualities with for instance 40 or minimal 3 Bq/kg [11].
Copper, having a lower Z and density compared to lead, is less suitable for the shielding, but is also less likely to be contami-

nated with primordial nuclei. Therefore, it is used as an additional layer, shielding the decay products emitted by ^{210}Pb and its daughter nuclides ^{210}Bi and ^{210}Po in the lead layer. Although copper can be produced by electrolyse with a low U and Th contamination, it has a rather high cross section for thermal neutron capture and for the cosmogenic production of radioactive isotopes like ^{60}Co. Accordingly, the exposure of copper, used in a low level experiment, at the earth surface should be minimised.

Nest: The inner set-up is a $10\times10\times10\,\mathrm{cm}^3$ copper case, called Nest, where 64 CZT crystals can be installed. These are arranged in a $4\times4\times4$ array, by mounting 16 crystal on each of four delrin holders. This is shown on the right side of figure 3.2.
Five Teflon tubes feed into the central copper casing, being used for flushing the Nest with nitrogen in order to reduce the radon concentration in the inner set-up. Additionally, wire mounted calibration sources can be fed through these tubes into the inner Nest, enabling frequent energy calibration without opening the shielding structure.

The COBRA prototype set-up uses CZT crystals, supplied by eV-Microelectronics (former eV-Products), with dimensions of about $1\times1\times1\,\mathrm{cm}^3$ and a mass of $\approx$6.5 g. These CZT crystals have low radioactive contamination [22] of:

^{40}K: $A < 3.7\,mBq/kg$
^{238}U: $A < 7.3\,mBq/kg$
^{232}Th: $A < 2.2\,mBq/kg$

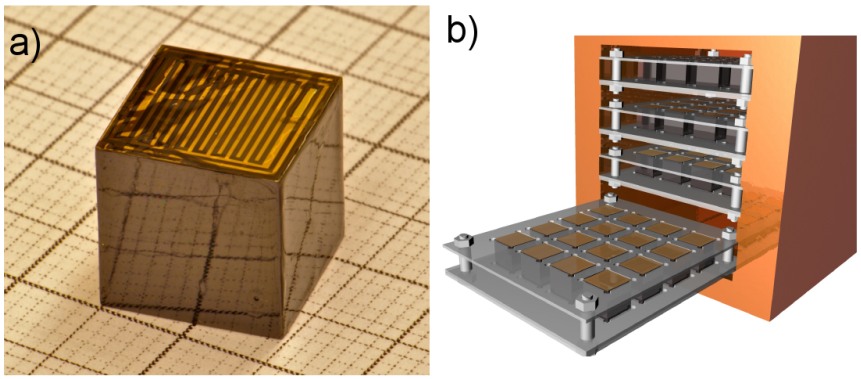

Figure 3.2: a) CZT detector with colourless passivation and coplanar grid anode [23]. b) Inner copper case (Nest), containing 64 CdZnTe detectors on four Delrin holders [19].

They are commercially supplied with a red passivation, which prevents the degradation of the crystal material due to oxidation processes or moisture. This passivation has been identified as the main background source in a former test set-up with 16 crystals. Crystals with a low background optimised colourless passivation had a reduced background level of about a factor 10 [24] and are investigated in the current set-up with eight crystals of two different passivations. The left side of figure 3.2 shows one of 64 CZT detectors with colourless passivation, which will be installed soon.

CZT detectors operate with a high voltage of about one kV/cm, being applied between the cathode (bottom side of crystal in figure 3.2) and a coplanar grid anode (upper side of crystal in figure 3.2). CZT detectors with a common anode have, due to different charge carrier mobilities and trapping times, a signal, which depends on the collection time and point of interaction. Thus, a suitable energy resolution could not be obtained. The coplanar grid anode has been developed as electron-only readout (see [25]) and therewith energy resolutions of under 1 % (FWHM at 662 keV) can be achieved. Typical crystals used for the COBRA prototype set-up have resolutions of around 3-5 % [8].

3.3 Motivation for scintillator upgrade

Besides the $0\nu\beta\beta$ decays, the $2\nu\beta\beta$ transitions are of physical interest as well. The $2\nu\beta\beta$ decay of ^{116}Cd into the first excited state is of interest for this thesis. Figure 3.3 shows the transitions of ^{116}Cd into the ground and first excited state of ^{116}Sn. The decay of ^{116}Cd into the first excited state is accompanied by the emission of a 1294 keV photon.

The current Cobra experiment has a low efficiency for gamma ray detection. Only about every tenth of the in this decay emitted 1294 keV photons interacts with the small CZT detectors and the full energy of these photons is detected for only 1% of the decays. This leads to a small detection efficiency for this double beta decay. Accordingly, an upgrade of the current COBRA setup to enable a better gamma ray detection is desirable.

The aim of this thesis is therefore to develop a design of a COBRA upgrade with a high detection efficiency for the decay of ^{116}Cd into the first excited state. A desired upgrade should achieve high detection ef-

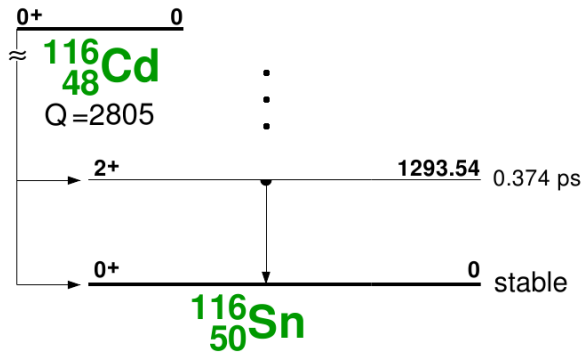

Figure 3.3: Decay scheme of ^{116}Cd into the ground and first excited state of ^{116}Sn [16]

ficiency and a good energy resolution, be compact in size and should have a moderate price and low intrinsic background. The following requirements should be fulfilled:

- The high detection efficiency requires a 4 π solid angle coverage and high absorption efficiency for photons of the detector material.
- Liquid scintillators are not considered, as the safety requirements for liquids at LNGS are very high.
- As double beta decay experiments require very low background count rates, the detector material must be carefully chosen to enable radioactive activities of the mBq/kg level.
- The experiment is hosted in a Faraday cage of around $2\times1\times1\,\mathrm{m}^3$ dimensions. The upgraded setup, including the copper and lead shielding must fit into this housing.

The primary aim of this upgrade is to detect the neutrino accompanied double beta decay of ^{116}Cd into the first excited state. As this is a very rare process, the emphasis is placed rather on high detection efficiency than on a superior energy resolution. As semiconductor detectors can provide a very good energy resolution, but cannot provide high detection efficiency, the future detector component will be a scintillation detector. Scintillation detectors can provide a very high detection efficiency and a 4 π solid angle coverage, but can achieve only energy resolution of more than about 5 % FWHM.

Therefore, a suitable scintillator material has to be found. For this thesis it is necessary to get an overview of the available scintillation detectors, the commercial prices and their properties, making them more or less suitable for this experiment. This is discussed in chapter 4—"Scintillation detectors".
The steps of developing the design for the upgrade are described in chapter 5—"Scintillator upgrade". Further on, the gain of the planned upgrade was determined with Monte Carlo studies of the $2\nu\beta\beta$ decay of ^{116}Cd into the first excited state.

Chapter 4

Scintillation detectors

Scintillation detectors consist of a scintillating material and a readout device, detecting the emitted scintillation light. This scintillation light is a radiation induced luminescence, emitted by dielectric materials. The process, which leads to the emission of scintillation light, consists thereby of a chain of processes, which depend on the atomic, molecular or crystalline properties of the scintillator [26].

Scintillating materials have been used for radiation detection since the beginning of the 20th century. The first application was a zinc sulfide screen, viewed with the naked eye to detect α-particles, developed by Crookes in 1903. The beginning of the modern scintillation detector was the invention of the photomultiplier tube (PMT). In 1944, four decades after the first visual scintillation counter, Curran and Baker detected the scintillation light of a ZnS screen with a PMT connected to an oscilloscope. With such an assembly Blau and Dryfus showed that the PMT current varies with the radiation intensity, making the use as dosimeter possible. Thereafter the search for scintillating materials developed rapidly. In 1947 Browser and Kallman studied the scintillation light produced by α-, β- and γ-rays in various materials like ZnS, $CaWO_4$, $ZnSO_4$ and naphthalene, which was the first organic and large volume scintillator. The good scintillation properties of thallium doped NaI was discovered by Hofstadter in 1948. The development of many scintillators followed quickly and is still ongoing [27, 28].

Today, scintillators are used in a broad field of applications. They are established in the fundamental research of particle and nuclear physics such as high energy physics (BaBar - CsI calorimeters), Dark Matter

search (DAMA - NaI), neutrinoless double beta decay and neutrino detection experiments (SNO+ - LAB). They are also used in commercial fields like medical imaging applications (PET scanner - BGO), container and baggage scanning, industrial gauging and many more.

This chapter will explain in 4.1—"Scintillator crystals" the main characteristics of the scintillation process and will give an overview of the conventional scintillator materials. In 4.2—"Detector assembly" the electronic readout devices and aspects of the detector mounting are discussed.

4.1 Scintillator crystals

The basic part of a scintillation detector is the scintillating material, emitting the scintillation light. The process, which leads to the emission of the scintillation light, starts with ionizing radiation, penetrating a scintillating material. Section 4.1.1—"Interaction of ionizing radiation with matter" therefore discusses how incident radiation gets absorbed or attenuated in the scintillator and deposits energy. The conversion of this energy into luminescence emission is explained in 4.1.2—"Scintillation process". Afterwards an overview of commercial scintillators is given in section 4.1.3—"Scintillating materials".

4.1.1 Interaction of ionizing radiation with matter

For categorization of its interaction with matter, ionizing radiation can be divided into direct and indirect ionizing radiation. Direct ionizing radiation are charged particles. It is convenient to treat particles (like α, p and μ) and electrons and positrons separately. Indirect ionizing radiation are electromagnetic radiation and neutrons. The sources of ionizing radiation were discussed in chapter 3—"The COBRA experiment".

CHARGED PARTICLES like α, p, μ interact mainly through the coulomb interaction with the atomic electrons. The energy loss through elastic scattering with the nuclei is possible, but of minor importance. The collisions with the constituent electrons are inelastic, and momentum and energy are transferred, raising the interacting electron to a higher lying shell (excitation) or remove it completely from the atom (ioni-

sation). The transferred energy in each collision is small compared to the particle energy, but the number of interactions is high on small path lengths, leading to high ionisation densities. The path of these particles in matter is, due to the small energy and momentum per interaction, especially straight. The stopping power, which is the energy loss per differential path length due to ionisation, varies with the density and Z of the material and with the square of incident particles charge. The collisions can also produce high energy recoil electrons (δ- or knock-on electrons), that cause secondary ionisation.

ELECTRONS AND POSITRONS loose their kinetic energy by excitation and ionisation processes and through emission of Cherenkov radiation and Bremsstrahlung. The energy loss by ionisation varies also with the density and Z of the material.The energy loss through Bremsstrahlung rises with Z^2 and dominates the energy loss for electrons and positrons with energies much higher than MeV. The electron path is, in contrast to heavy particles, not straight but tortuous so that the path length is up to 4 times longer than the transversed absorber [28]. Positrons annihilate at the end of their range with an constituent electron and two almost collinear 511 keV photons are emitted. [29]

ELECTROMAGNETIC RADIATION

Photons interact when penetrating a medium by the five fundamental mechanisms of electromagnetic interactions: photon absorption, electron-positron pair production, incoherent and coherent scattering and the nuclear photoelectric effect. They lose energy mainly by the first three processes. For photons with energies $E_{ph} < 100\,\text{keV}$ photo absorption, for $E_{ph} \approx 1\,\text{MeV}$ the Compton process and for $E_{ph} > 2\,\text{MeV}$ the pair production dominates for materials of medium Z like NaI. Figure 4.1 shows the mass attenuation coefficient μ/ρ for these processes in sodium iodide, which is proportional to the cross section.

The photo effect is the absorption of a photon of energy E_{pe} by an atom, which emits a subsequent photoelectron. Such total absorption can only occur if the electron is initially bound to the atom and momentum is conserved by the recoil of the residual atom. In the majority of events, the photoelectron is ejected from a K or L-shell with an energy $T_{pe} = E - B_e$ where B_e is the binding energy of this electron. Subsequent characteristic X-rays or Auger electrons are emitted by the filling of the vacant energy state, left by the ejected photoelectron. The photoelectron and the subsequent emitted photon of Auger electron is also mostly absorbed by the scintillator, so that in the photo effect the complete energy of the incident photon is absorbed.

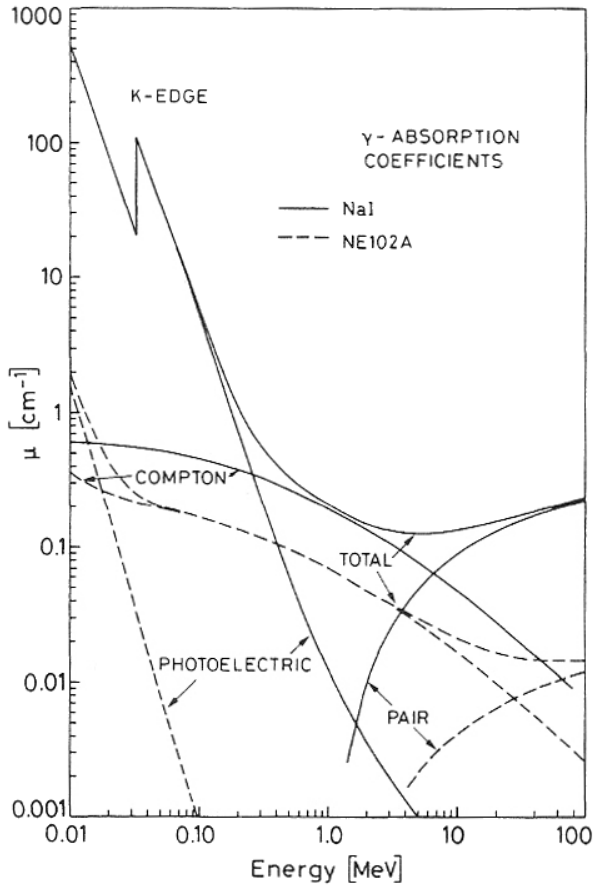

Figure 4.1: Photon mass attenuation coefficients for NaI, figure taken from [27]

The total cross section varies in complex manner with E and Z. The photoelectron cross section for MeV photons varies approximately as Z to the power of 4 or 5, depending on the photon energy. So materials with high Z are preferable for γ-ray detection. Below 0.1 MeV the photo effect cross section is complicated by the presence of absorption edges at which the photoelectron cross section decreases sharply with E. There the photon energy is smaller than the binding energy $B_e = B_K, B_L, \ldots$ and the corresponding electrons stop to contribute to the photo effect [28, 29, 30].

Compton scattering is the incoherent collision interaction of photons

and quasi-free electrons. These electrons can be considered as free if the photon energies E_{ph} are much higher than the binding energy of the electron B_e. In Compton scattering the photon energy cannot be totally absorbed by the free electron. The scattered photon has an energy E'_{ph}:

$$E'_{ph} = \frac{E_{ph}}{1 + \alpha(1 + cos\theta)}, \tag{4.1}$$

which depends on the scattering angel of the photon θ and the initial energy of the photon E_{ph}, with $\alpha = E_{ph}/m_e c^2$. The photon can scatter with different probabilities in all directions, with E'_{ph} being maximal for small scattering angles around 0° and minimal for backscattering of 180°.
Correspondingly, the transferred recoil energy of the electron can have values between zero for (no scattering) and the maximal transferred recoil energy T_{cm} in the case of backscattering. This continuum of recoil energies is called the Compton continuum with T_{cm}, being the Compton edge:

$$T_{cm} = \frac{E_{ph}}{1 + (1/2\alpha)} \tag{4.2}$$

The total attenuation cross section for Compton scattering is energy dependent and can be divided into a component for absorbed energy σ_a and one for scattered energy σ_s. They represent the average fraction of the incident photon energy E_{ph} which can be absorbed in the material after the conversion into the Compton electron of energy T_c or which is scattered in form of a photon in a collision. (see figure 4.1)

When the photon energy exceeds twice the electron mass $2m_e c^2$, pair production is possible. It occurs only in the presence of an electric field of a charged particle, normally of the nucleus, but also of the electron if the photon energy exceeds $4m_e c^2$. The photon is completely absorbed and its energy is converted into the rest mass and kinetic energy $T_{pp} = E - 2m_e c^2$ of an electron-positron pair. The cross section rises approximately with Z^2.

These three effects lead to a spectrum of secondary electrons whose energies depend on the energy of the primary photon. The photoelectrons have energies $T_{pe} = E - B_e$, the Compton electrons have a spectrum of energies T_{cs} from 0 to $T_{cs,max} = E/(1 + m_e c^2/2E)$, and pair production produces an electron-positron pair with energy $T_{pp} = E - 2m_e c^2$. The relative number of each group of electrons depends, for a given material, on the energy of the initial photon. Figure 4.2 shows this energy

spectrum, produced by monoenergetic photons of energy $E > 2m_ec^2$. For detectors, also backscattering peaks, escape peaks and multiple Compton events can be seen in an energy spectrum.

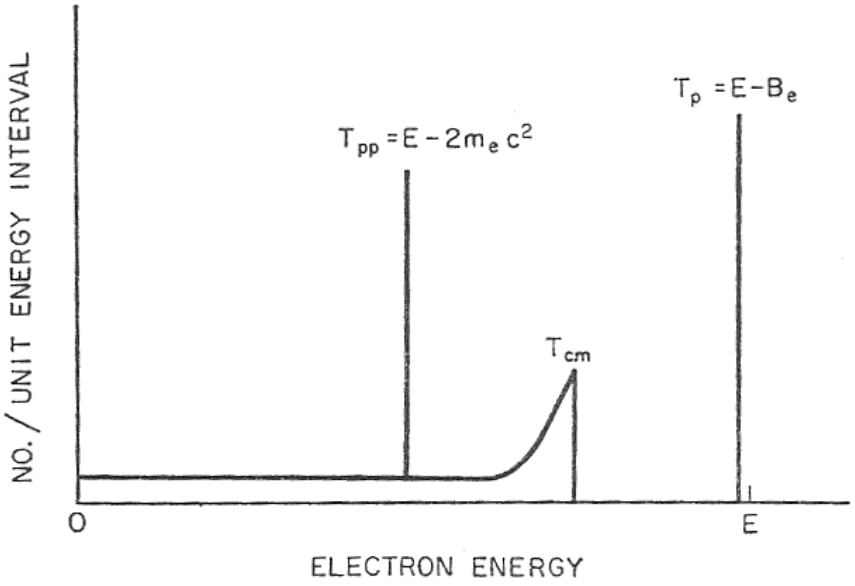

Figure 4.2: Energy spectrum of the primary electrons produced by monoenergetic photons of energy $E > 2m_oc^2$ in an absorber [27].

The residual energy of the scattered photons which is not transferred to electrons or positrons at the primary interaction is present in the scintillator as photons of reduced energy. These are X-rays of energy B_e, photons of energy $E - T_{cs}$ and annihilation quanta of energy m_ec^2. X-rays are usually absorbed by the scintillator and the latter two have according to their reduced energy a higher probability of being absorbed than the primary photons. Consequently a high efficiency for full photon energy detection can not be achieved with absorbers of slightly larger dimensions than the range of the primary photon. This requires absorber sizes were also secondary photons, electrons and positrons are completely absorbed. Simulations considering the optimal absorber dimensions are presented in chapter 5.1—"Monte Carlo studies for the upgrade design".

NEUTRONS interact mainly with the nuclei of the absorber material, rather than with the atomic electrons. As uncharged massive particles they penetrate the electron clouds of the atom and collide with the nucleus. Scattering and absorption are the two possible types of interac-

tion of neutrons with the nuclei. In the former the neutron collides with a nucleus and a fraction of the neutron energy is transferred to the recoil nucleus. In the latter the neutron is absorbed by the nucleus and the excited product may fission or emit gamma radiation or nucleus and thereafter be stable or radioactive. Neutron absorption is more likely to happen for low neutron energies and the absorption cross section depends on the absorber material [26, 27, 28, 29, 30].

4.1.2 Scintillation process

The scintillation process starts with the energy deposition in the scintillating material by penetrating ionizing radiation and leads in a chain of processes to the emission of scintillation light. Scintillation processes are based either on molecular, atomic or crystalline excitations. So, the actual scintillation process depends on the kind of material, being organic or inorganic and solid, liquid or gaseous. As has become clear in the last chapter, materials with high density and high atomic number are needed for efficient gamma ray absorption. Therefore, no inorganic materials with small Z and ρ will be considered. In the following the scintillation process of inorganic crystals will be explained and the characteristics of the resulting emission spectrum will be discussed.

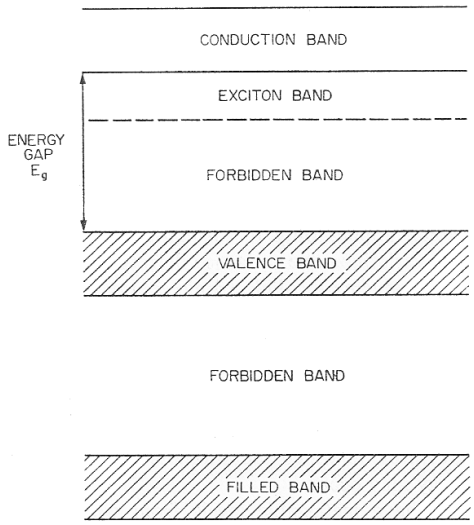

Figure 4.3: Band structure in an ideal insulating crystal with core, valence and conductive band [27].

SCINTILLATION MECHANISM OF INORGANIC CRYSTALS

The luminescence of inorganic crystals is a crystalline property. For its description the band theory of crystalline solids, introduced by Bloch, is needed. It describes the band structure of ideal crystals and must be modified for crystals containing impurities and defects. In an ideal crystal, energy bands, separated by forbidden regions of energy, are formed. Figure 4.3 shows a schematic view of this band structure. The lower bands (core bands) are completely filled, while the higher bands are empty. These bands extend throughout the crystal, where electrons and holes are free to move in them without additional activation energy. The highest filled band (valence band) is separated from the lowest empty band (conduction band) by an energy gap E_g.
The luminescence of inorganic crystals requires the existence of luminescence centres embedded into the crystal lattice. The scintillation emission depends on the kind of luminescence centre and on the energy states determined by the crystal lattice of the host material. The emission centres lead to variations in the energy bands. They can produce local electronic energy levels in the normally forbidden region between the conduction and valence bands.

The emission centres are either interstitial or substitutional impurities, excess atoms or ions, or atoms or ions associated with defects. Thus crystal scintillators can be divided into the three broad groups of the impurity activated (alkali halides activated by heavy metals as thallium or europium), self activated (like $CdWO_4$, CdS and ZnS) and pure crystals (pure alkali halides and diamond). The majority of efficient inorganic luminescent materials are impurity-activated crystals like NaI:Tl and CsI:Tl.

The scintillation process can be explained in five steps, describing the relaxation from the primary high-energy excitation to the final scintillation light emission by the luminescence centres:

1. **Formation of electron-hole pairs:** The scintillation process starts with the production of primary excitations in the scintillator by ionizing radiation. The ionizing radiation will directly or indirectly create electron-hole pairs, by exciting electrons from the valence or deeper bound states to levels in the conductive band. Very high energetic ionizing radiation creates hot electrons in the valence band and mainly deep holes h, being in inner core bands. These excitations produced a large number of secondary excitations through inelastic electron-electron scattering and Auger

processes.

2. **Thermalisation of charge carriers:** The second stage is the thermalisation of the previously formed electronic excitations under phonon emission. This leads to electrons of low kinetic energy in the bottom of the conduction band and holes in the top of the valence band.

3. **Formation of excitonic states:** The thermalised electrons and holes can be involved in several ways into the further scintillation process. In this step the thermalised charge carriers form excitonic states, which can excite the luminescence centres further on. These can be excitons or captured electrons and holes.
   Excitons are electron-hole states with a slightly smaller energy than the band gap energy E_g. They can be formed by direct radiative recombination of an electron and a hole. These excitons can be bound or be free to migrate in the crystal lattice. Electrons, holes and free excitons can also be captured by traps or in the crystal lattice. The trapping of electrons and holes leads to a decorrelation of the electron-hole pairs, but can produce bound excitons after subsequent hole and electron trapping.

4. **Excitation of luminescence centres:** Luminescence centres can be excited by correlated electron-hole pairs, excitons and separated electrons or holes. They lead to an excitation of the luminescence centre through sequential capture of charge carriers or energy transfers.

   In the presence of impurity centres or activator ions, the luminescence emitted by the exciton decay can excite the luminescence centre. Also, the recombination of captured holes with electrons can excite nearby luminescence centres. In these cases, energy is transferred to the luminescence centre.
   The direct capture of free thermalised electrons or holes by activator ions is also possible. The excitation over charge transfer processes with a sequential capture of charge carriers leads to the subsequent formation of excited luminescence centre states. This competes with the previous exciton formation.
   The direct excitation of the activation centres by ionizing radiation is also possible and leads to an important contribution to the scintillation of heavy doped and self-activated scintillators.

   The excitation of luminescence centres competes with the excitation of traps, whose transition to the ground state is forbidden. The excitation of traps reduces the amount of luminescence

emission and leads to a slow component of light, which can be as after-glow an significant source of background.

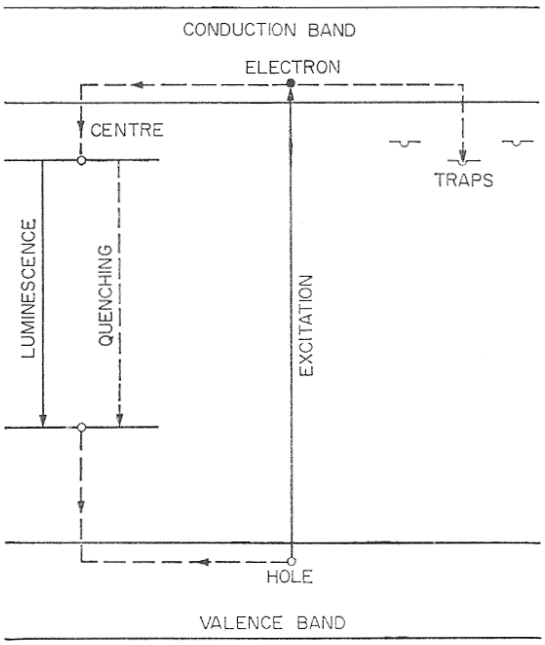

Figure 4.4: Scheme of light emission in an scintillation crystal, with traps, luminescence and quenching mode [27]

.

5. De-excitation of luminescence centres: The emission of light by the luminescence centres is the last step of the scintillation process.

The deexcitation mechanism depends on the electronic structure of the luminescence centre and the surrounding host lattice. Thereby, radiative and nonradiative transitions can compete.
Radiative transitions between excited luminescence centre states and their ground states lead to luminescence emission. Non-radiative transitions are called quenching processes and are possible with intermediate excitation levels between the ground state and the emission level and over multi-phonon emission. Ions like Tl^{+}, Bi^{3+} and Ce^{3+} with a large free gap between their $6p$ or $5p$ emitting level and their ground state are therefore more efficient luminescence centres than ions like Pr^{3+} with many $4f$ levels lying between the $5d$ emission level and the ground state.

These two kinds of de-excitation modes are shown in figure 4.4.

Scintillators can have different coexisting types of luminescence centres and excitons. These can have different excitation probabilities, decay times, energy states and probabilities of luminescence emission. Their excitation probability depends on the density and type of various excitations, temperature, doping and crystal purity.

The just introduced scheme describes the scintillation process for simple ionic crystals with simple energy structure, but is not sufficient for scintillators with a more complicated band structure. Rare earth and cross luminescent crystals need an extended description to account for a possible direct excitation of rare-earth ions and core-valence transitions of cross-luminescent materials [26].

The **SCINTILLATION LIGHT YIELD**

In scintillation processes only a part of the deposited energy is converted into scintillation light. The remaining energy is dissipated radiationless, mainly in form of lattice vibrations of heat. The scintillation light yield L is a measure for the scintillation efficiency of a given scintillator. It stands for the number of emitted optical photons by a scintillator per unit energy deposited by ionizing radiation in the scintillator. L is determined by the amount of radiative transition of excited luminescence centres into their ground state. It is therefore determined by the product of the efficiency of the five steps of the scintillation process.

$$L = N_{eh} S Q \tag{4.3}$$

Accordingly, N_{eh} is the efficiency for converting deposited energy of incident ionizing radiation into thermalised electron-hole pairs and excitons. It depends on the deposited energy E_{dep} and the required energy for producing one electron-hole pair, which are about three times of the band gap energy E_g [27]. S is the probability for exciting luminescence centres:

The mechanism of the excitation of the luminescence centres and its cross section is strongly influenced by the surrounding medium. The energy states of the lattice and the luminescence centre determine the energy transfer between them.

The probability for hole capture is for instance determined by the position for the ground state of the activator and the valence band of the host lattice. To enable the trapping of a hole, the ground state of the

activator should lie energetically above the valence band, but should lie low enough to maintain a high probability for hole capture. Vice versa, this applies for electrons and the energy gap between the bottom of the conduction band and the radiation level of the doping ion. In general, the energy of the excited activator state should be smaller than the bandgap energy E_g to prevent self-absorption of the scintillation light by the host lattice.
Instead of exciting luminescence centres, the electrons, holes and excitons can be bound by traps. These are metastable levels from which the charge carriers may subsequently return to the conduction band by acquiring thermal energy from the lattice vibrations or fall to the valence band by a radiationless transition.
Q is the luminescence quantum yield, which is the efficiency for the luminescence emission of an activated luminescence centre and depends on the kind of excited state of a luminescence centre.
Scintillation yields can be a few thousand to much more than 60.000 photons per deposited MeV for efficient scintillators [26, 27].

The amount of produced photons varies and leads to an intrinsic scintillator resolution. The variation results from three factors. There is a nonproportionality of the number of emitted photons to the incident energy. The importance of this factor depends on the scintillator material and the considered energy region. Also, the electronic excitations of various energies lead to a distribution of light yields, which increase the energy resolution. Additionally, local variations of the light yield are caused by inhomogeneity of the crystal.

DECAY TIME

The time characteristic of the scintillator is determined by the half-life characteristic of the excited states. Mostly, the migration time does not influence the time characteristic, because it is much shorter than the half-life. The impurity configurations are formed essentially after 10^{-12}-10^{-8} sec and then de-excite with the corresponding half-life of typically 50-500 ns. Inorganic scintillators can have more than one decay time, originating from different excitations of luminescence centres. In general, the time evolution of the luminescence emission can be described by one or two exponential decay forms [26, 27, 28, 29].

TEMPERATURE DEPENDENCE

The light output of scintillators also depends on temperature. While organic scintillators have a temperature independent light output, the light output of inorganic scintillators can vary strongly with temperature. As shown in figure 4.5 NaI:Tl has a stable light output between 20 and 40°C, increasing with higher and lower temperature. $Bi_4Ge_3O_{12}$

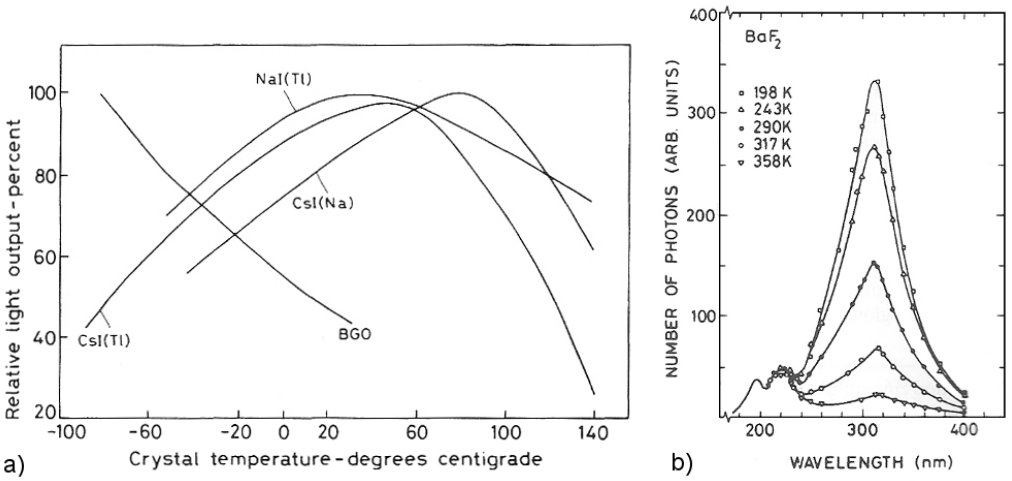

Figure 4.5: a) The temperature dependence of the light output for various scintillators is shown [28]. b) The emission spectra of BaF_2 at various temperatures can be seen. The slow decay component (right peak) shows a strong temperature dependence, in contrast to the fast component (two left peaks) [29].

(BGO) has a maximum light output at low temperatures and $CdWO_4$ (CWO) has the maximum light yield at room temperature ($\approx 20°C$).
The temperature dependence of the light output can be determined by the doping. Pure CsI has a quite different temperature dependence than thallium or sodium doped CsI. Its light output decreases steadily from minus 70°C to room temperature. Whereas CsI:Na has its maximum light output at 80°C and CsI:Tl at around 50°C. The different decay components can also show an independent temperature dependence. As can be seen in figure 4.5, the fast BaF_2 component (220 nm) shows a stable amount of scintillation light over a wide temperature range (-50 to 150°C), while the de-excitation via the slow component depends strongly on temperature [27, 28, 29].

QUENCHING FACTOR

The light yield depends on the energy and the type of incident ionizing radiation. Charged particles like α-particles and charged ions have a higher stopping power dE/dx and produce lower light yield per unit length dL/dx than electrons. This is due to quenching processes, which are nonradiative de-excitation modes. Such states get more often populated at higher ionisation densities. Without quenching, the light yield is proportional to the deposited energy: $dL/dx = S \cdot dE/dx$ with the scintillation efficiency S. Birks proposed a semi-empirical formula to

describe the quenching effect, the "Birks formula" [29]

$$dL/dx = \frac{S \cdot dE/dx}{1 + kB \cdot dE/dx}. \tag{4.4}$$

He introduced the quenching factor k and BdE/dx, which describes the density of excitation centres along the track. kB is also referred to as the Birks factor. Likewise the α/β-ratio is quoted, which is related to the Birks factor as long as the Birks formula is valid for this scintillator. It is the ratio of the light yield for α particles to the light yield for electrons of the same energy.
The quenching factor and α/β-ratio depend on the crystal and the conditions of the experiment. For doped materials the strength of quenching is related to the amount and kind of dopant.
The α/β ratio is 0.66 - 0.67 for NaI:Tl and CsI:Tl and 0.2 for BGO. The light output of inorganic scintillators depends generally less on the particle energy than the light output of organic scintillators, which can have quenching factors of 10 [27, 28, 29].

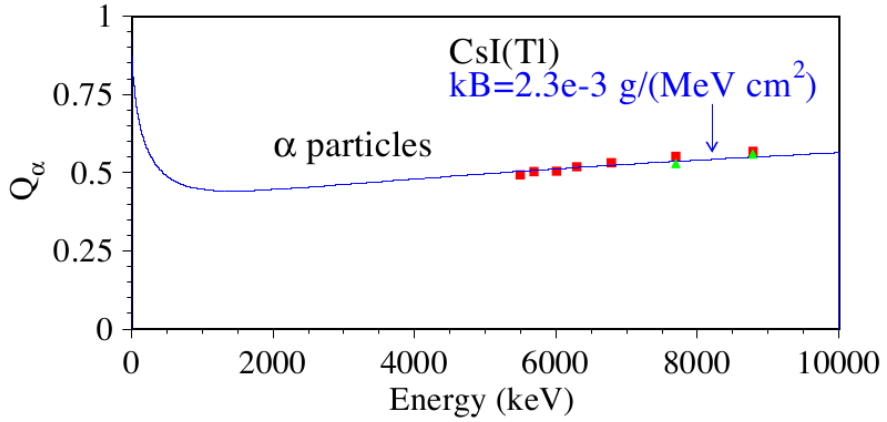

Figure 4.6: Quenching factors for α-particles in CsI:Tl and calculated quenching curve with $kB = 2.3 \cdot 10^{-3}$ gMeV^{-1}cm^{-2} for $\Delta t = 5\,\mu$s [31]

The time Δt of the scintillation signal collection also determines the measured quenching factors. The amplitudes of different scintillation light components depend on dE/dx. As these components have often different decay times, different fractions of these components are collected in different Δt. For α particles in CsI(Tl) with energies between ≈ 0 and 10 MeV the Birks factor was determined to be $1.1{\times}10^{-3}$ gMeV^{-1}cm^{-2} for $\Delta t = 1\mu$s and to $2.3{\cdot}10^{-3}$ gMeV^{-1}cm^{-2} for

$\Delta t = 7\mu$s (figure 4.6). With the time dependence of the amplitude and decay time of the different components Birks factor also varies with temperature. So the α/β ratio increases with decrease of temperature from +20°C to -20°C by 7 % in NaI(Tl), 35 % in CsI(Tl) and 25 % in CsI(Na). An increase of temperature from +20°C to +80°C leads to a decrease of 3 %, 15 % and 30 % in these crystals.
Wrongly chosen collecting times Δt can lead to a seemingly enhancement of the scintillation light instead of quenching for charge particles. In CsI(Tl) $\Delta t = 1\,\mu$s leads to higher light output for 662 keV protons than photons of the same energy, because of a faster scintillation signal of the proton [31].

PULSE SHAPE DISCRIMINATION
For scintillator materials with more than one decay component, the population of these components depend, beside temperature and activator concentrations, also on dE/dx and can show a dependence on the type of radiation in the shape of the scintillation pulse. There it is possible to distinguish heavy charged particles from lower energetic photons or electrons with a pulse shape discrimination. In CsI:Tl the decay time varies from 0.425 μs for α-particles over 0.519 μs for protons to 0.695 μs for electrons [28].

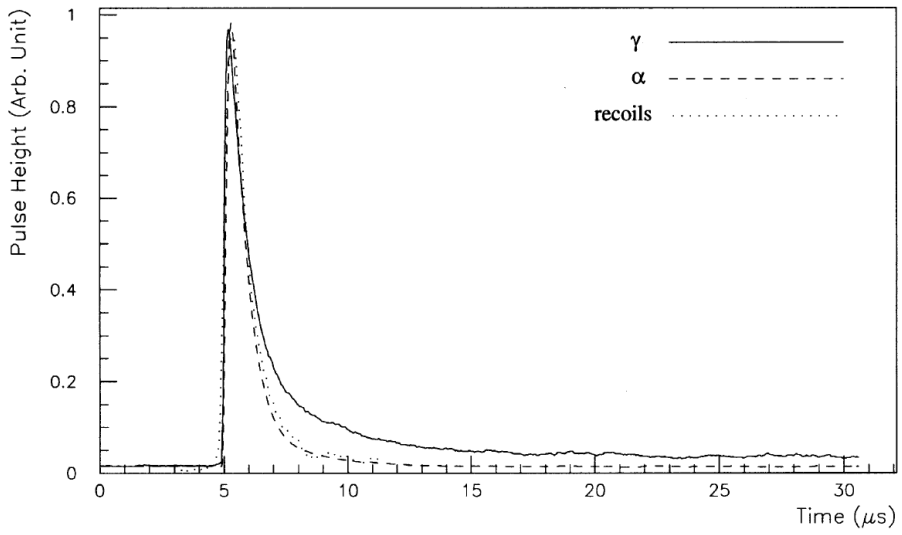

Figure 4.7: Pulse shape of CsI:Tl for events with γ-rays at 660 keV, α-particles at 5.4 MeV and nuclear recoils at 45 keV [32].

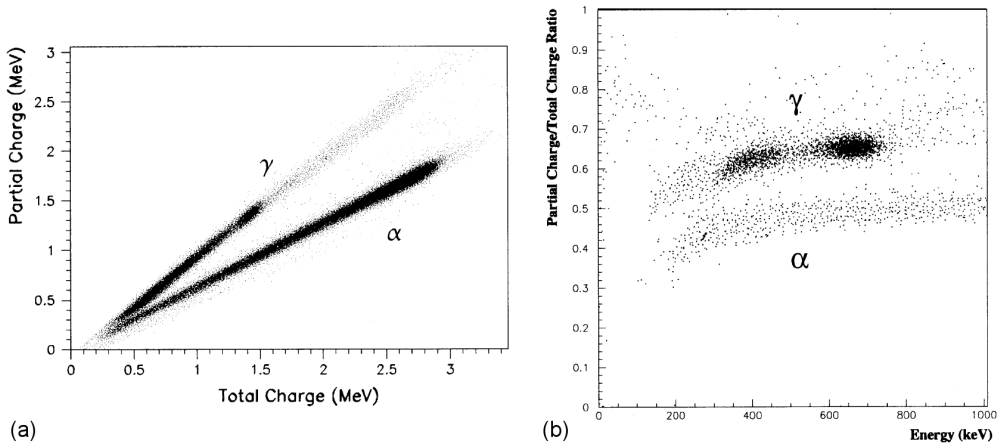

Figure 4.8: Discrimination of γ/α events with double charge method. The partial charge is plotted versus the total charge for high (a) and low (b) energy α and γ events in CsI:Tl [32]

.

The fast and slow decay components arise from the de-excitation of different excited states of the luminescence centres. These states are finally populated in relative intensities, depending on the density and kind of excitations. Here, high ionisation loss leads to a high density for bound excitons [33], which, when captured by an impurity centre, excite the latter to states that causes a fast component. Successively captured single free electrons and holes give rise to excitations of metastable states of the luminescence centres, causing a slow decay component [27, 28, 29].

The TEXONO collaboration achieved with CsI:Tl crystals and PMT readout a efficiency for γ/α discrimination of more than 99 % [32] (figure 4.8). They used the double charge method [34] for the pulse shape discrimination and could maintain this efficiency for events of down to $\approx$ 100 keV electron-equivalent light output. The different decay time constants of γ ($\tau_{fast} = 0.87\,\mu s, \tau_{slow} = 5.20\,\mu s$) and α ($\tau_{fast} = 0.54\,\mu s, \tau_{slow} = 2.02\,\mu s$) events enable the discrimination by comparing the "total charge" (integrated charge over 4 μs) and the "partial charge" (charge integration also over 4 μs, with a delay time of 0.5 μs).
Dinca et al. [33] quoted to obtain the optimum for α/γ discrimination for a short (1 μs) and a long (6 μs) time gate.

SELF-ABSORPTION
The emitted light can be reabsorbed during its path through the crystal volume. This can occur either through the same kind of luminescence centre, which essentially just leads to a longer decay time and it can be absorbed by different luminescence centres. The latter case can reduce the scintillation light significantly, being a problem for large-size scintillators.
The scintillation emission spectrum is shifted, in comparison with the absorption spectra of the host lattice, to longer wavelengths, because the excited states of the luminescence centres have in general smaller energies than the band gap of the host crystal. This leads in the ideal case to no absorption of the emitted photons by the host crystal lattice. If the emission and absorption spectra overlap nevertheless, self-absorption occurs and the crystal is not opaque for its own scintillation light. Such crystals may only be used as small layers.

4.1.3 Scintillating materials

A broad spectrum of scintillating materials has been discovered and developed during the last 65 years. Organic and inorganic scintillators in solid, liquid and gaseous states are available.

Inorganic scintillators can be, like the alkali halides, of high density (NaI=3.76 and CsI=$4.51\,\mathrm{gcm}^{-3}$) and typically consist of high Z elements (I=53, Cs=55). Thus they have a high stopping power, which makes them suitable for gamma ray detection. Inorganic solid scintillators can be crystals, glasses, powder, ceramics, films and polycrystalline materials. Some of these have the highest light output of all scintillators, which is vitally important for a good energy resolution. A by far incomplete abridgment of inorganic solid scintillators and their properties is listed in table A.1.

An important property for low level experiments is the radioactivity of the detector components. Intrinsic and extrinsic radioactive isotopes, being either contaminations or components of the crystal and surrounding material, can reduce the resolution of a scintillator significantly. Especially scintillator materials containing components with high abundance of radioactive isotopes are limited in their use for low background measurements. In general, the main source of radioactive contamination in scintillators are naturally occurring radioisotopes of the ^{235}U, ^{238}U and ^{232}Th decay chains and ^{40}K. Another important

group of radioactive nuclides in scintillators are anthropogenic nuclides like ^{60}Co and ^{137}Cs. Some scintillators consist of elements containing radioactive isotopes like listed below in 4.1.

Scintillator	Radioisotope
$CdWO_4$ (CWO)	^{113}Cd
Gd_2SiO_5 (GSO)	^{152}Gd
$LaCl_3$ and $LaBr_3$	^{138}La
Lu_2SiO_5 and LuI_3	^{176}Lu
$PbWO_4$ (PWO)	^{210}Pb

Table 4.1: List of some scintillation materials and contained radioisotopes [35].

Scintillators based on Pb (except ancient Pb, which is expensive), La and especially Lu can have a radioactivity of 10 and even a few 10000 Bq/kg for Lu [35, 36]. The most radiopure crystal scintillators like $ZnWO_4$, $CdWO_4$ and low background optimised CaF_2:Eu, NaI:Tl and CsI:Tl have low contamination of 0.01-0.1 mBq/kg [35]. However, it is possible to produce crystals from depleted or enriched isotopes, but this will increase the price significantly.

The other aspects of the scintillator, like available size, light yield, price and whether it is hygroscopic reduce the list of possible scintillators further. Scintillators, like ZnS:Ag, $ZnWO_4$, CaF_2:Eu are not available in adequate size. CaI_2 has a high light yield but a low density and it is highly hygroscopic. $Y_3Al_5O_{12}$ (YAG) has a slightly higher density but a low light yield. The same arguments apply for BaF_2 and CaF_2.
From these huge spectrum of available scintillators especially NaI, CsI, BGO and CWO are described more closely and their main properties are listed in table 4.2. They are common scintillators, can be obtained in adequate size, are less expensive than other scintillators, have high density and Z and can be produced with low radioactive contamination.

NaI:Tl is one of the most used scintillators. It can be produced in large dimensions and has a relatively high density and atomic number. Its emission spectrum matches good with common bialkali photo multiplier tubes (PMTs). In this range of wavelength (around 400 nm) NaI:Tl has the highest light yield of all scintillators. High-purity NaI activated by 10^{-3} mole fraction of thallium is a hygroscopic crystal that must be protected from moisture in the air with an air tight enclosure. The crys-

tal is very fragile and can easily be damaged by thermal or mechanical shock. It has a dominant fast decay component of 230 nm and slow component of 0.15 s that contributes 9 % to the total signal. The afterglow can pile up at high count rates or can be resolved with PMTs as single photons at low count rates. NaI:Tl detectors can achieve around 6-7 % FWHM energy resolution at 662 keV [26, 27, 28, 29].
The handling of low background NaI:Tl scintillation detectors was discussed in detail by the DAMA/LIBRA collaboration [37], using ≈250 kg of highly radiopure NaI:Tl scintillator crystals. They achieved to reduce the contamination of ^{232}Th, ^{235}U, ^{238}U and other possible background components to the range of μBq/kg.

CsI:Tl has an even higher light yield than NaI:Tl, is less brittle and is only slightly hygroscopic. Thus it should not be exposed to water or high humidity, it can generally be handled without protection. With 65.000 photons per deposed MeV CsI:Tl has the highest light yield of all scintillators at room temperature. Though the emission peak wavelength lies with 550 nm at the border of the detectable spectrum for bialkali PMTs, the emission spectrum matches better with photodiodes or PMTs with multialkali photocathode. CsI has two decay components, one with a fast decay time of 0.68 μs (64 % for incident electrons) and a slow component of 3.34 μs (36 %). The scintillation light has an exceptional long rise time of 20 ns [26, 27, 28, 29]. Pulse shape discrimination with CsI:Tl is also possible Liu et al. [32]. Zheng et al. [38] quoted an optimum Tl concentration for maximum scintillation light output of 400 ppm Tl. Brose et al. [39] reported a temperature dependence at room temperature of 0.3 %/K for a photodiode (Hamamatsu S2744-08) readout, 0.4 %/K for a PMT with multialkali photocathode (Hamamatsu R669) and 0.6 %/K for a PMT with blue-sensitive photocathode.

Scintillator	Z_{eff}	ρ (g/cm^3)	hygroscopic	λ_{max} (nm)	light yield (ph/MeV)	refractive index at λ_{max}
NaI:Tl	50.8	3.67	yes	415	43000	1.82 [40]
CsI:Tl	54.0	4.51	slightly	560	51800	1.79 [40, 36]
BGO	75.2	7.13	no	505	8200	2.15 [36]
CWO	64.2	7.90	no	495	19700	2.3 [36]

Table 4.2: List of scintillators and their main characteristic wavelength of maximum emission λ_{max} [26].

BISMUTH GERMANATE ($Bi_4Ge_3O_{12}$ or BGO) is a nonhygroscopic scintillator with very high Z and a greater efficiency for photoelectric conversion of gamma-rays than NaI:Tl and CsI:Tl. BGO has high density

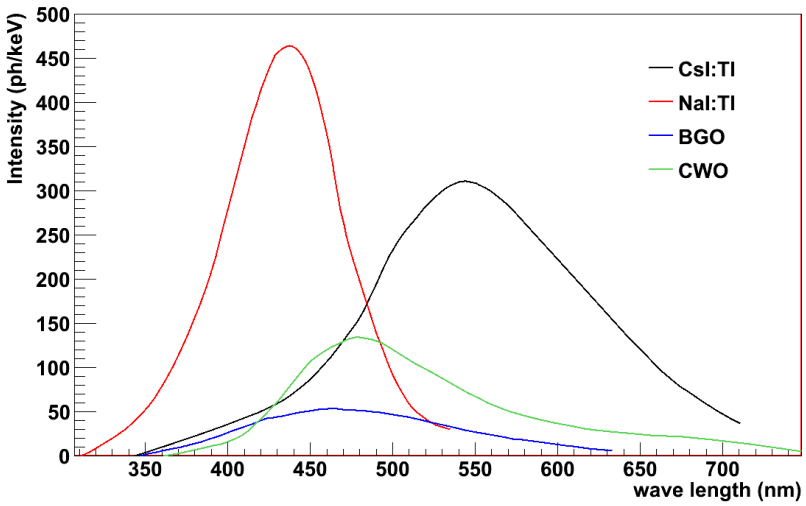

Figure 4.9: Emission spectrum of CsI:Tl, NaI:Tl, BGO and CWO [36]

and large atomic number. It has very little self-absorption and its mechanical and chemical properties make it easy to handle. However its low light yield of just 10-20 % compared to NaI:Tl leads to a resolution of about a factor two worse than NaI:Tl. It also has a high refraction index of 2.15, making the light collection more difficult. BGO is suitable if high gamma ray detection efficiency is more important than a good energy resolution. The primary decay component is 300 ns and an additional fast component (60 ns) has a fraction of 10 %. The emission peak wavelength lies at 505 nm. The light yield increases at low temperatures, so it has a limited use at temperatures higher than room temperature. BGO is two to three times more expensive than NaI:Tl [26, 27, 28, 29].

CADMIUM TUNGSTATE ($CdWO_4$ or CWO) has been known as a scintillator since about 1950, but has been produced only since 1990 with interesting crystal size and good optical properties. The light yield is 40 % of NaI:Tl and the emission peak wavelength is at 495 nm. The density and the effective atomic number are even higher than these of BGO. A pulse shape discrimination is also possible. The use of CWO is, due to its long decay time of 1.1 μs (40 %) and 14.5 μs (60 %) limited for low count rates. With an refraction index of 2.3 the light collection and coupling to readout devices are also difficult. CWO is more expensive than BGO [26, 27, 28, 29].

4.2 Detector assembly

The other important component of a scintillation detector is the electronic readout. It converts the part of the scintillation light that reaches the device, typically just a few hundred photons, into a usable electric signal. This can be done with photomultiplier tubes or diodes. In the following section, possible devices are introduced, afterwards the aspects of detector mounting and the light collection are discussed in section 4.2.2—"Detector mounting" and finally the energy resolution of scintillator is discussed in section 4.2.3—"Energy resolution".

4.2.1 Electronic readout devices

PHOTO MULTIPLIER TUBES (PMTs) are evacuated glass or metal tubes, consisting of a front glass with photocathode, followed by the dynode string that multiplies the photoelectron (electron cascade) and an anode that collects the multiplied electrons. The final PMT signal is proportional to the number of incident photons, until a saturation at high photon fluxes.

Roughly every fourth initial photon that hits the photocathode produces a photoelectron. In this case the initial photon is absorbed by the cathode material and its energy is transferred to the atomic electrons. The electrons can then migrate towards the surface and escape from the photocathode if their energy is higher than the work function of the material. Higher quantum efficiencies are achieved with cathode materials that have a negative electron affinity (see Knoll [29] p. 271). The quantum efficiency of modern photocathodes, which is the ratio of emitted photoelectron per incident photon, is 20 to 30 %. It is mainly limited by the escape width of the photoelectrons, because photocathodes of this thickness are still semitransparent for photons.
The resolution of PMTs can be limited for low count rates by dark current. At room temperature $10^6 - 10^8$ electrons per $m^2 s$ are emitted from the photocathode. This number increases with temperature. Especially large diameter PMTs can have less resolution due to variations of the thickness of the photocathode. The quantum efficiency also depends on the wavelength of the incident photon. The detection of photons with long wavelength is limited by the height of the potential barrier and at short wavelength by the opacity of the entrance window material. The cut-off lies for glass at 350 nm and for fused silica or quartz at 160 nm. This is shown in figure 4.10. Multialkali (Na_2KSb) cathodes

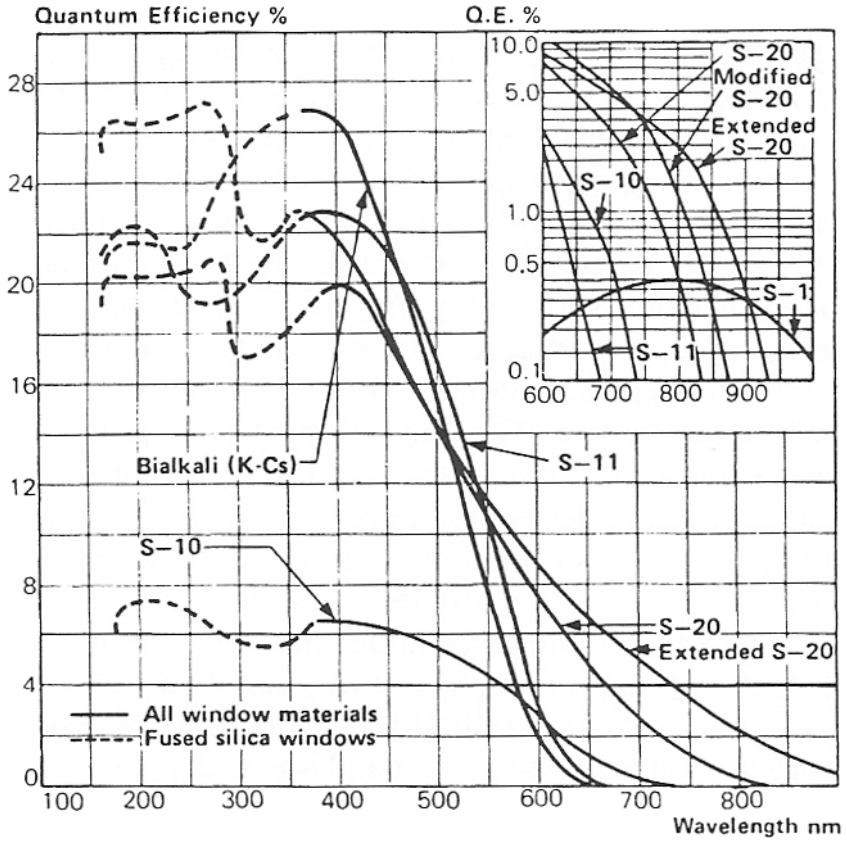

Figure 4.10: Quantum efficiencies of various photocathode materials [28].

have quantum efficiencies of up to 30 %. The common used bialkali cathode (K_2CsSb) has even higher quantum efficiencies in the blue region and a lower noise level, but smaller quantum efficiency in the red and the infrared region.

The photoelectrons are emitted with less than 1.8 eV and then accelerated to the first dynode. A voltage of up to 2000 V is applied between cathode and anode with a stepwise changing potential along the dynodes. The impact of a single electron leads to the emission of 4 to 6 secondary electrons at typical interdynode voltage differences of a few hundred volts. BeO, MgO and Cs_3Sb are usual dynode materials. Dynode materials with negative electron affinity like heavily doped GaP can have multiplication factors (number of emitted secondary electrons/initial electrons) of up to 50 for a 1 kV dynode voltage. These

secondary electrons are accelerated to the second dynode and so on. PMTs have typically 9 to 16 dynodes and an overall multiplication factor (gain) of 10^6 up to 10^9. The final electron pulse is collected at the anode and has a time delay of 20-50 ns and a width of a few nanoseconds. The detection of single photons is possible. The Hamamatsu PMT R669 shows a temperature coefficient of -0.3 %/K at 550 nm [39]. The time resolution of a PMT is mainly determined by the escape velocity of the photoelectron and the distance between the emission point and the hitting point at the first dynode. It is typically below one ns [28, 29, 30].

PIN diodes consist of a p-doped primary material that is heavily n-doped on one surface. A controlled diffusion of the donator atoms leads to a n-doped layer at the surface and an internal i-region, with nearly intrinsic properties. There the number of acceptor and donator atoms is identical and the specific resistance of $10^5\,\Omega$cm corresponds to the intrinsic resistance of silicon. The depletion zone must be thick enough so that incident particles can create enough ionisation in the sensitive region to form a larger signal than the noise level. The thickness of the depletion zone is limited to 10 to 15 mm and is much bigger than that of diodes with pn-junction. This is suitable for beta or low-energy photon detection. The small p-layer of the diode is the entrance window. The incident ionising particles can produce direct or indirect electron hole pairs. Those are produced in the i-region and the induced charge is processed to an attached preamplifier to produce the output signal at the anode. With a required energy for excitation of 3.6 eV in Silicon and 2.8 eV in Germanium, they are able to detect the typical scintillation light of 3-4 eV with a high quantum efficiency of 60-80 %. Only in the best case, as much electron hole pairs as incident scintillation photons are produces. These are typically just a few hundred. Without any multiplication process the signal is 8 orders of magnitude lower than that of PMTs. Electronic noise is a problem due to this very small signal. PIN diodes have a factor 2 worse resolution than PMTs and can compete only for high energetic particles [29]
The temperature dependence of photodiodes (Hamamatsu S2744-08) is very small with 0.01 %/K at 550 nm [39].

The greater sensitive region leads to a greater thermal noise than normal diodes. Thus cooling is necessary to gain a high resolution. The dark noise can also be reduced by using materials with a larger band gap than silicon, like mercury iodide crystals. Such PIN diodes are superior to PMTs and achieve energy resolutions of 4.58 % with CsI:Tl scintillators [28, 29, 30, 41].

AVALANCHE PHOTO DIODES (APDs) are diodes with an internal multiplication process. The small amount of charge, which is produced in conventional diodes, is increased with the avalanche effect. The charge carriers are accelerated sufficiently between collisions with the lattice to produce additional electron hole pairs. The gain is independent of the amount of incident light for applied voltages higher than the breakdown voltage. APDs are used with applied reverse voltage near below the breakdown voltage. There, the gain is proportional to the applied voltage. With a gain of a few hundred a signal is produced that is bigger than the electronic noise level. The quantum efficiency is 80 %. The signal level is very sensitive to temperature and the applied voltage. Statistical variations of the avalanche effect lead to considerable fluctuations in the multiplication process. These are larger than the fluctuations in the multiplication process of PMTs and can significantly contribute to the energy resolution. It becomes usually inferior to conventional silicon photodiodes. A better energy resolution for lower particle energies, as can be achieved with conventional diodes, is nevertheless possible, because the noise level of the preamplifier is usually much higher than the noise level of diodes. The dark current depends on the diode size and is between 0.5 and 50 nA [29, 41].

SI-PMT are pixelated avalanche diodes used in Geiger mode. This is the operation at break down voltage, where the gain is independent of the bias voltage. Si-PMT are with a gain of 10^5 to 10^6 competitive to PMTs. The signal of a Si-PMT is the sum of each APD pixel output. Single photons produce detectable charge avalanches. This allows the counting of single photons or the detection of pulses of multiple photons. Due to the limited pixel number, saturation occurs for high count rates. Room temperature operation is possible. They have good time resolution and can work in magnetic fields.

4.2.2 Detector mounting

Having a scintillator and an electronic readout device, the latter must be mounted onto the scintillator in a way that allows the detection of as much scintillation light as possible. Self-absorption and losses at the scintillator surfaces impede the collection of the entire produced scintillation light. The amount of self-absorption depends on the scintillator size and opacity. It becomes a non-negligible factor for scintillator length that is in the order of the attenuation length of the crystal. This can be, depending on the quality of the crystal, up to meters.

advantages	PMT	PIN	APD	Si-PMT
quantum efficiency	20-30%	60-80%	60-80%	60-80%
gain	$10^6 - 10^9$	1	500	10^6
big active area	✓	-	-	-
compact size	-	✓	✓	✓
disadvantages				
sensitive to magnetic fields	✓	-	-	-
bias/supply voltage	✓	-	-	-
high temperature dependence	✓	✓	✓	-
high voltage dependence	✓	✓	✓	-
high noise level	-	✓	✓	-

Table 4.3: Advantages and disadvantages of different readout devices

Scintillation light is emitted isotropically from the track of the ionizing particle and only a small fraction reaches the photocathode or diode directly. The rest impinges at the boundary and is reflected or transmitted. The total internal reflexion occurs for light with incident angles greater than the Brewster angle $\theta_B = sin^{-1}(n_{out}/n_{scint})$ with n_{scint} and n_{out} the refraction index of the scintillator and the surrounding material. For smaller angles partial reflection occurs where a part of the light is reflected and the remainder is transmitted. This losses reduce the efficiency of scintillation light detection and consequently the energy resolution. They also lead to a non-linearity of the detected signal depending on the point of emission. There are several methods to increase the efficiency of light collection.

SCINTILLATOR WRAPPING AND SURFACE FINISH. The amount of reflected light can be increased by using a reflector that redirects the light back into the scintillator volume where it reaches the readout directly or via more reflections. With each reflection some degradations occur due to absorption and transmission, thus the number of reflections is limited. The reflector surface can be specular or diffuse. At specular reflexion the incident angle θ_i equals the reflection angle θ_r. At diffuse reflexion θ_r is independent of θ_i and follows Lambert's cosine law $dI/d\theta_r \propto cos\theta_r$ with I the intensity of reflected light. Common aluminium foil is used as specular reflector and MGO, TiO_2 and aluminium oxide are good diffuse reflectors.

The difference between specular and diffuse reflection is small and depends on the scintillator geometry. Care must be taken for scintillator with emission spectrum smaller than 400 nm. The reflectivity of TiO_2

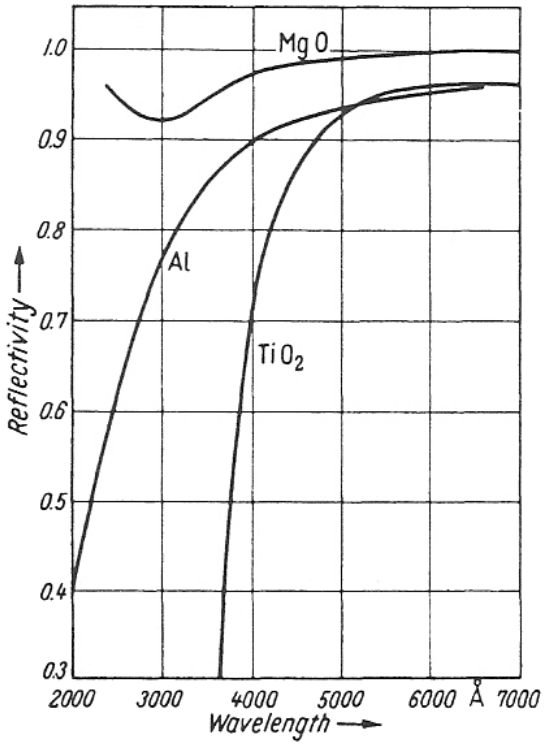

Figure 4.11: Reflectivity of various reflector materials [28].

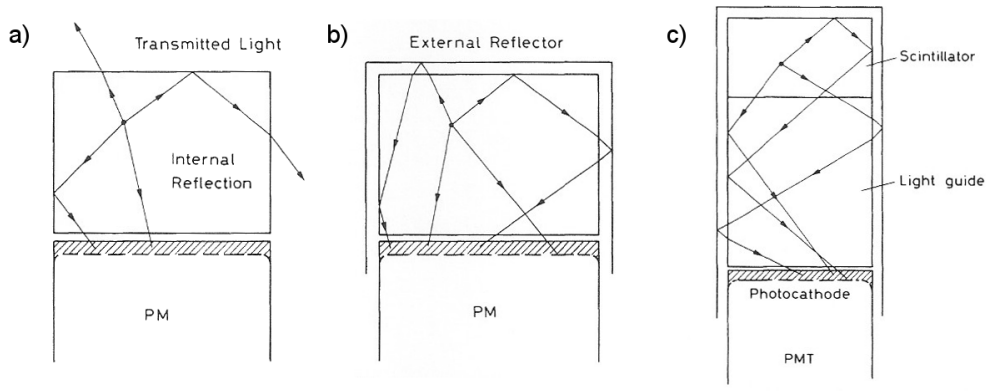

Figure 4.12: Scintillation detector with and without reflector, coupled directly or via a light guide to a PMT.

drops sharply at 400 nm and the reflectivity of Al also decreases (figure 4.11). MgO is a suitable reflector also for light of lower wavelength. These external reflectors yield a good light collection efficiency which can be further improved by increasing the internal reflection. The material surrounding the scintillator should therefore have a low refractive index. A gap of air between the scintillator and the refractor is a convenient and effective solution. With such an assembly θ_B reduces to 42° for $n_{scint} = 1.5$. The surface of the scintillator can be polished or ground leading to diffuse or specular internal reflection [29, 28].

OPTICAL COUPLING. The coupling between the scintillator and the electronic readout should transmit as much light as possible. A layer of air in between should be avoided. A small air gap between a CsI:Tl crystal ($n_{CsI:Tl}$=1.79) and a photodiode (n_{PD}=1.5) reduces the electron yield by 15 % [39]. An optical glue, grease or oil with an refraction index between the scintillator and the PMT or diode window is the optimal optical coupling (see [39] for more details). The PMT window mostly consists of glass or quartz with an refraction index of n_{window}=1.5. The refraction index of silicon matches very good with organic scintillators. Finding a suitable optical grease for inorganic scintillator is more complicated [28, 29].

LIGHT GUIDES are coupled in between the scintillator and the readout. They are used if the direct coupling is impossible or not desired due to lack of space, an inconvenient scintillator shape, the presence of magnetic fields or for a reduction of the radioactive background induced by the readout electronics. Photons, entering the light guide reach through internal reflexion to the readout. The light guide surface is often polished and good results are obtained with external reflectors. R. L. Garwin declared with phase space arguments that the photon flux density in light guides is not compressible. Accordingly, due to the Liouville Theorem a flux of light with the intensity I_{in}, incident at an area A_{in}, cannot be compressed into a smaller cross section area at the output A_{out}. Due to loss, the light intensity at the output is only in the ideal case $I_{in} \cdot A_{out}/A_{in}$ and in general smaller. [28, 29, 30]

WAVE LENGTH SHIFTER (WLS) play an important role for big scintillator volumes. They permit the collection of scintillation light from big areas and enable the detection of the scintillation light with readout electronics of smaller area. Wave length shifters are essentially light guides with an admixture of a fluorescent wave length shifting material. They absorb incident scintillation light and reemit light with a longer wavelength. The WLS is coupled optically to the electronic readout, but is usually separated from the scintillator crystal by an air

gap. Though this reduces the transmission from the scintillator to the WLS, it also reduces the transmission of the re-emitted light into the scintillator and increases so the part of detected light. Whether WLSs improve the detected signal depends strongly on the scintillator geometry and produced scintillation light. For scintillators with an emission spectrum higher than the optimal wavelength of the readout electronic a shift can improve the detection efficiency significantly. A stepwise shifting with more than one WLS, to reduce the readout area further, is also possible.

SIZE OF SENSITIVE AREA. The just discussed techniques do improve the detected signal. Nevertheless, especially for big scintillators, the only way to obtain a usable signal is often to increase the readout area. Therefore either more or bigger readout devices are necessary. Multiple readout devices at opposite scintillator sites improve the uniformity of light collection. With coincidence analysis, background due to dark current of the readout devices can be reduced. Moreover a position reconstruction in addition to an energy detection is also possible with more than one readout device. Lee et al. [42] reported position accuracy of less than one cm with 40 cm long CsI:Tl coupled to two red enhanced PMT.

4.2.3 Energy resolution

The energy resolution of a scintillation detector depends on the resolution of the scintillator, the collection efficiency of the scintillation light and the intrinsic resolution of the electronic readout device.

The resolution of the scintillator is determined by the amount of produced scintillation photons and their variation. Thereby, the efficiency of radiation absorption limits the amount of ionizing particles which can deposit their full energy. This is especially for gamma ray detection at low count rates a limiting factor and materials with high Z and high density are preferred.

Non-uniform distributions of the luminescence centres in the lattice produce local variations of the intrinsic scintillation efficiency. As was discussed previously, L also depends on dE/dx. Accordingly, the light yield for photons of the same energy varies in dependence of the amount and energy of produced photo, Compton, pair and Auger-electrons. Initially produced photoelectrons have higher energies than Compton electrons and a subsequent photoelectron, produced by inci-

dent photon of the same energy. The scintillation yield L/E decreases with increasing particle energy E. This leads to more produced scintillation photons for Compton scattered gamma rays than for photons absorbed directly by the photo effect. The full energy line width depends on the contribution of Compton scattering and the photo effect. It gets wider the more both processes contribute. With an increasing scintillator size the contribution by Compton effect rises. Therefore the intrinsic resolution decreases while the amount of fully absorbed gamma rays increases. For high count rates scintillators of small crystal sizes have better energy resolution.

The efficiency for the collection of scintillation light depends in general on the scintillator dimensions, the size and position of the readout device and the opacity of the crystal. Thus, it also depends on the wave length of the emission spectrum, the refractive index of the scintillator, on the optical coupling, on the refractor and on the entrance window of the readout device at these wavelengths. Ultimately, absorption and loss reduce the detectable scintillation light and worsens the resolution. Readout devices at opposite sides of the scintillator increase the collection efficiency in general and increase the uniformity of the light collection, leading to decreasing variance.

Birks [27] quoted that larger crystals have worse resolution due to difficult uniform light collection. Non-proportional scintillator response contributes in the same order of magnitude to a decrease in resolution as nonuniform light collection.

The intrinsic resolution of the readout device is determined by the photoelectron emission efficiency and the electron multiplication process. The quantum efficiency of the photocathode limits the amount of produced photoelectrons. It depends on the wavelength of the incident photon and on the point of impact. A nonuniformity of the photocathode leads only for very low count rates to a wider line width and does not contribute otherwise. Thus large diameter PMTs should be avoided in this case. Finally variations in the multiplication process of the photoelectron in the case of PMT, APD and Si-PMT contribute to the resolution. All readout divices loose resolution due to dark current and PIN diodes especially due to electronic noise [27, 30].

For the simulation, described in the next chapter, the energy resolution, reported by Kim et al. [43], was used. The KIMS Collaboration used CsI:Tl crystals with surfaces from 55x55 to 70x70 mm^2 and 300 mm length. The crystals were wrapped in two 0.2 mm thick Teflon layers and couplet to two three inch PMT's type D726UK, with RbCs

photocathode, fabricated by Electron Tubes Ltd.. The energy resolution at 662 keV was around 4.2 % (RMS) and the resolution curve was parametrised by $\sigma = 0.58 \cdot \sqrt{E\,(keV)} + 0.0191 \cdot E\,(keV)$. The relative standard derivation was evaluated with radioactive sources like ^{55}Fe, ^{241}Am, ^{57}Co, ^{137}Cs, ^{22}Na and ^{60}Co positioned in the centre of the crystal and a ^{60}Co source with collimator positioned in 5 cm distances. In this way the energy dependent and also position depending resolution due to doping nonuniformity and different collection efficiency was regarded [43].
The announced standard derivation σ determines the FWHM of any Gaussian through the relation FWHM$= 2\sqrt{2ln2}\sigma \approx 2.35\sigma$.

The requirements for the COBRA upgrade are, as is discussed in the previous chapter 3, a low radioactive contamination, a high energy resolution, a moderate price and a high detection efficiency at compact size.

The four scintillators NaI:Tl, CsI:Tl, BGO and CWO can provide some of these properties.
All four scintillators can have low radioactive contamination, depending on the used scintillator powder and crystal production process.
CWO contains the intrinsic ^{113}Cd, which has a low Q-value, BGO can contain ^{207}Bi, which has a problematically high Q-value and CsI:Tl contains the anthropogenic radioisotope ^{137}Cs. CWO and BGO have high density and high Z, but a lower light yield than NaI:Tl and CsI:Tl. Especially NaI:Tl has low density and Z, whereas the level of radioactive contamination can be very small. The drawback of NaI:Tl is also the emission spectrum, matching well with bialkali PMTs. CWO, BGO and CsI:Tl can be read out with semiconductor readouts. The reached energy resolution depends, beside the light yield of the scintillator and the matching of the scintillation emission spectrum with the quantum efficiency of the readout, also on the crystal and readout dimensions. It is not possible to deduce the reachable energy resolution of a scintillator of several hundred cm^3 from the resolution obtained with a small scintillator. The required compact size of the planned COBRA upgrade favours the scintillator readout with semiconductors, providing, the detection efficiency and energy resolution are high enough and the background contamination is small enough. The consideration, which of these scintillators is most suitable, requires studies, which are presented in the following chapter.

Chapter 5

Scintillator upgrade

After discussing possible scintillator materials and readout devices in the previous chapter, this chapter will determine the kind of designed scintillation detector. Therefore, Monte Carlo simulations were performed to optimize the design of the scintillator upgrade. These simulations help to choose the optimal crystal size and readout electronic and are described in 5.1—"Monte Carlo studies for the upgrade design".

Accordingly, in 5.2—"The design" a detector upgrade with scintillation detectors is presented and the detection efficiency for a COBRA set up with a CsI:Tl detector component was studied with Monte Carlo simulations, described in 5.3—"Monte Carlo studies of the designed upgrade".

For this thesis, three Geant4 simulations were written, two independent Geant4 applications ("ScintBlock" and "CsI") and one package within the Venom simulation framework. The simulations were performed with the Geant4 software toolkit for detector simulations. The resulting simulated data were analysed with the ROOT data analysis framework.

Geant4 is an object-oriented toolkit for the simulation of the passage of particles through matter, written in C++. It provides a realistic reproduction of physical processes for an energy range from 250 eV up to a few GeV [44].
The Geant4 toolkit includes facilities for the handling of geometry, the tracking, the detector response and the visualization. The software is used by research projects at application areas including high en-

ergy physics and nuclear experiments, medical, accelerator and space physics studies.
The version geant4.9.2.p01, was used. It is available at `http://geant4.cern.ch/`.

ROOT is an object orientated programming framework, which provides tools and methods for data handling, analysis and plotting. It was developed at CERN and can be found at `http://root.cern.ch`. The ROOT version V5.20.00-sl5-x86_64.gcc4.1.2 was used during this thesis.

5.1 Monte Carlo studies for the upgrade design

The aim of this thesis is to develop a design of a COBRA upgrade with a high detection efficiency for the decay of ^{116}Cd into the first excited state. Besides having a low intrinsic background, the scintillation detector should achieve a high detection efficiency and a good energy resolution, be compact in size and should have a moderate price.

The number of possible scintillating materials was reduced in the previous chapter to NaI:Tl, CsI:Tl, BGO and CWO. This section evaluates the optimal crystal size, for these scintillators. Simulations with the application "ScintBlock" determined the efficiency of different scintillator sizes for absorption of photons and are presented in 5.1.1—"Scintillator size". Price researches for considered scintillator crystals are presented in 5.1.2—"Price research". The high light yield of CsI:Tl, its easier handling compared to NaI:Tl and the good matching with the compact semiconductor read-outs favours this scintillation material. The section 5.1.3—"Electronic readout" determines the optimal readout device for CsI:Tl crystals, considering in the previous section determine crystals dimensions.
The influence of the size of the active area and the quantum efficiency of the readout device were estimated with the simulation "CsI", considering the optical properties of the crystal.

5.1.1 Scintillator size

Finding an affordable scintillation detector with adequate detection efficiency requires the consideration of different aspects. In favour of

cost and the amount of needed shielding material, smaller scintillators would be preferable. Whereas, a good detection efficiency for gamma rays requires bigger scintillators. For finding an optimal size of NaI:Tl, CsI:Tl, BGO and CWO crystals, the absorption efficiency of different scintillator crystals for gamma rays was determined with the simulation "ScintBlock".

GEANT4 APPLICATIONS "SCINTBLOCK"

The setup of this simulation consists of a volume of $2.5\times2.5\times5\,m^3$ filled with air. Within this, a cage of $2\times2\times4\,m^3$ containing nitrogen gas and, as default, a $1\times1\times1\,m^3$ CsI scintillator block is positioned. The user can change the size and the material of the target interactively via the commands `/SB/det/setScintLength` and `/SB/det/setScintMat`.

The kind of the simulated particles and the physic processes are set in the PhysicsList class. All electromagnetic processes are defined for photons, charged leptons and charged hadrons. The primary kinematic consists of a single particle which hits the target perpendicular to the input face. The type of the particle and its energy are set in the PrimaryGeneratorAction class, and can be changed via the G4 build-in commands `/gun/particle` and `/gun/energy` of the ParticleGun class. As default a single 511 keV photon is initialised.

SIMULATION AND DATA ANALYSIS

Initially, a record of the number of the event (event ID), the number of the particle in the respective event (track ID), the kind of the particle (particle), the initial energy (E_i), the place of the interaction (x,y,z), the energy deposited in the scintillator (E_{dep}), the kind of the interaction (process) and the amount of recorded steps (step) was printed for every step with an interaction in the scintillator volume. In order to understand the tracking of a particle, this detailed output was used to reconstruct samples of simulated events.
An event of the simulation of a 500 keV gamma ray in NaI is shown in table 5.1. The initial photon is back-scattered and produces three Compton electrons (track ID 4, 3 and 2) before leaving the scintillator. This is recorded as transportation process (trans). The Compton electrons number 4 and 3 loose their energy by ionization processes (eIoni) and the electron number 2 emits Bremsstrahlung (eBrems) before being absorbed. The Bremsstrahlungs photon is absorbed by the photo effect (phot) and the produced photo electron (track ID 6) is stopped nearby.

In total 840 simulations with different macros were started, changing the photon energy, the crystal material and the crystal size. For each simulation, the impact of 50000 monoenergetic photons (one after the

event ID	track ID	particle	E_i	E_{dep}	x	process	step
6	1	gamma	500.00	0.00	31.83	compt	10
6	1	gamma	202.62	0.00	31.55	compt	10
6	1	gamma	131.54	0.00	15.92	compt	10
6	1	gamma	130.54	0.00	0.00	trans	10
6	4	e-	0.991	0.99	15.92	eIoni	10
6	3	e-	71.09	71.09	31.55	eIoni	10
6	2	e-	297.38	152.73	31.93	eBrem	10
6	2	e-	108.59	108.59	31.90	eIoni	10
6	5	gamma	36.06	1.56	25.24	phot	10
6	6	e-	34.49	34.49	25.24	eIoni	10

Table 5.1: Detailed output from simulation "ScintBlock" of one 500 keV photon in NaI, whereas y and z values of interaction points are missing in this list.

other) on a scintillator block with 1 m lateral length and 21 different width, ranging from 1 mm to 1 m was examined. Thereby photons with 10 different energies from 200 to 2000 keV were initialised. Due to the arguments from chapter 4.1.3—"Scintillating materials" only NaI, CsI, BGO and CWO crystal were considered.
For every data file, the total amount of interacting photons and the full-energy events were counted.

RESULTS

In table 5.2 the peak and total absorption efficiency for scintillators of different width for different photon energies, which was obtained with this simulation, is listed. The peak absorption efficiency is the efficiency for absorbing the full energy of the incident photon and the total absorption efficiency is the total efficiency of the initial photon for interacting with the scintillator material. This was mapped for incident 1200 keV photons, as can be seen in figure 5.1. The total and peak efficiencies of the four scintillators are shown in A—"FIRST APPENDIX" in figure B.1 - B.7.

NaI has the smallest density of these scintillators and correspondingly the smallest absorption efficiency. CWO has higher density but a smaller effective atomic number Z_{eff} than BGO. This leads to different total and peak efficiencies for BGO and CWO. The efficiencies depend on the density and atomic number of the absorber material and the energy of the initial photon.

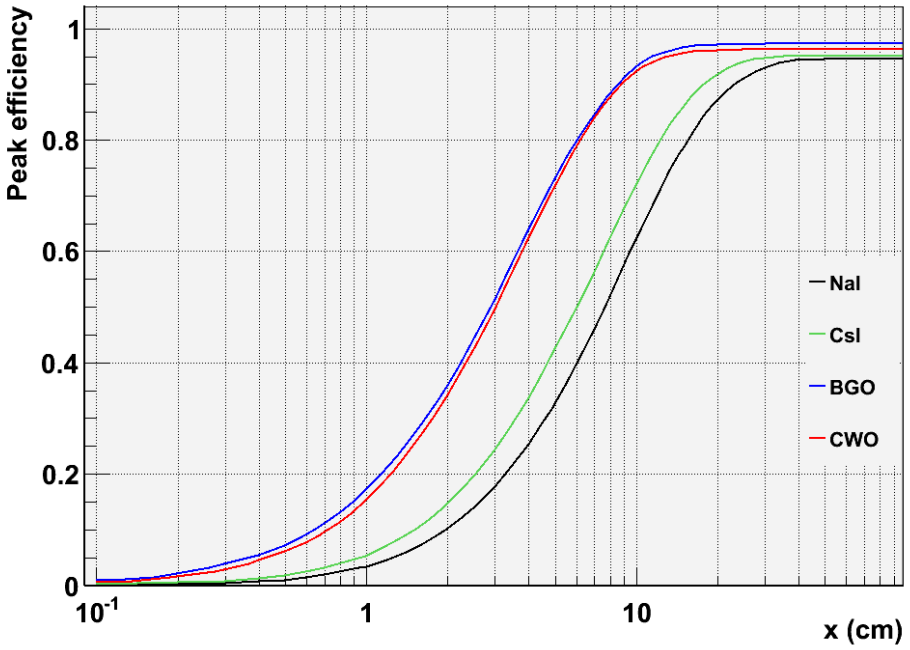

Figure 5.1: Ratio of 1200 keV photons, depositing full energy in the scintillator to total simulated photons, after various width of NaI, CsI, BGO and CWO

5.1.2 Price research

For a price estimation of the scintillator upgrade, quotations from Scionix [45] and SaintGobain [36] were solicited from EKM, the German distributor for Scionix and GCTechnology Messgeräte Vertriebs GmbH, the German distributor for SaintGobain. The prices are listed in table 5.3.

The analysis, discussed in the previous section, investigated the absorption efficiencies for different scintillators. An efficiency for absorbing the full energy of 90 % of the incident photons requires 23.2 cm of NaI:Tl, 18.6 cm of CsI:Tl, 9.0 cm of BGO and 9.2 cm of CWO. Due to the high cost for such big scintillator crystals, smaller detection efficiencies are inevitable.

In addition to the costs of the scintillation detectors itself, it is necessary to acquire new shielding material. The provided space in the Faraday

E_{photon} (keV)	200	400	600	800	1000	1200	1600	2000
Peak efficiency for								
5 cm NaI	0.962	0.730	0.550	0.444	0.377	0.328	0.263	0.221
10 cm NaI	0.967	0.912	0.817	0.740	0.675	0.622	0.539	0.486
5 cm CsI	0.969	0.833	0.661	0.549	0.476	0.421	0.340	0.294
10 cm CsI	0.969	0.946	0.886	0.825	0.766	0.718	0.642	0.587
5 cm BGO	0.977	0.971	0.929	0.862	0.793	0.730	0.635	0.575
10 cm BGO	0.977	0.974	0.971	0.963	0.948	0.928	0.883	0.843
5 cm CWO	0.974	0.958	0.905	0.837	0.770	0.715	0.636	0.575
10 cm CWO	0.974	0.966	0.961	0.952	0.938	0.920	0.880	0.846
Total efficiency for								
5 cm NaI	0.987	0.864	0.765	0.702	0.659	0.615	0.569	0.535
10 cm NaI	0.991	0.976	0.943	0.912	0.881	0.851	0.810	0.782
5 cm CsI	0.991	0.921	0.834	0.773	0.729	0.689	0.635	0.607
10 cm CsI	0.991	0.989	0.969	0.948	0.924	0.903	0.867	0.844
5 cm BGO	0.990	0.992	0.974	0.940	0.907	0.874	0.827	0.796
10 cm BGO	0.990	0.994	0.996	0.994	0.990	0.983	0.970	0.957
5 cm CWO	0.991	0.990	0.969	0.942	0.913	0.884	0.844	0.816
10 cm CWO	0.991	0.994	0.995	0.994	0.991	0.986	0.976	0.968

Table 5.2: Efficiencies of 5 and 10 cm CsI, NaI, BGO and CWO for gamma ray detection and gamma ray energy absorption.

material	crystal size	quantity	distributor	price apiece (Euro)
BGO	50x50x50 cm^3	8		1420
	50x50x200 cm^3	12	EKM	4840
NaI:Tl	with stainless steel housing, two assembled 3" PMT Typ ETL 9265			
	150x150x400 cm^3			16820
	100x150x400 cm^3			12480
	100x100x150 cm^3		EKM	5400
CWO	50x50x140 cm^3		Vsiliev [46]	6000
CsI	100x100x300 cm^3	8		15000
	50x50x200 cm^3	12		2300
	50x100x100 cm^3	2	Qian [47]	2500
CWO	50x50x100 cm^3	24		5822
	50x50x50 cm^3	8	GCT	2911
BGO	50x50x200 cm^3	12		6250
	50x50x50 cm^3	8	GCT	1875

Table 5.3: Quotations for scintillators

cage is also limited. It is therefore favourable to build a compact scintillation detector.

The advantages and disadvantages of these four different scintillators for the planned COBRA upgrade are listed in table 5.4. NaI:Tl, although being a common used scintillator with a very high light yield and low radioactive contamination, has for this project a to low density and atomic number. Additionally, the required PMT readout and the difficult handling of this hygroscopic scintillator is not suitable. An upgrade with BGO can be used with diode readout and is compact in size, but BGO has a low light yield, leading to a low energy resolution and the contained radioisotope ^{207}Bi (Q-value = 2.3 MeV) can be a serious background component for the searched signal. CWO is a suitable scintillator for this upgrade, but is nearly twice as expensive as BGO. CsI:Tl has the highest light yield, a readout with diodes is possible and the radioactive ^{137}Cs is not expected to be a serious background for the $2\nu\beta\beta$ signal of transitions into the excited state. Although it is not as compact as BGO or CWO, this upgrade is also less expensive.

scintillator	light yield	size	handling	diode readout	radioactivity
CsI:Tl	✓✓	✓	✓	✓✓	✓
CWO	✓	✓✓	✓✓	✓	✓
BGO	-	✓✓	✓✓	✓	-
NaI:Tl	✓✓	-	-	-	✓✓

Table 5.4: Advantages (✓) and disadvantages (-) of different scintillators.

Accordingly, 5 cm of CsI:Tl were considered as a compromise between cost and detection efficiency. Due to its much higher light yield than BGO and CWO and, in comparison to NaI:Tl, more easy handling, it was chosen as the most promising scintillator material for this upgrade.

5.1.3 Electronic readout

The Cobra Nest will be surrounded by a layer of 5 cm CsI crystals. For a high detection efficiency and smaller amounts of needed scintillator material, the scintillator should be placed as close as possible to the Nest with as little material as possible between the CZT and the scintillators. The scintillator readout device is therefore placed at the outer sides of the scintillator layer. Additionally, electronic devices nearby the CZT detector increase the background level. In general, all six outer sides of the layer could be used for placing the readout. The front and

back side of the scintillator layer are favoured by the restricted space inside the Faraday cage. A readout from only two sides also reduces the amount of needed readout devices. For such a readout, 12 crystals of $20\times5\times5\,\mathrm{cm}^3$ dimensions and 8 cubes of $5\times5\times5\,\mathrm{cm}^3$ are necessary. The crystal bars are placed at the right, left, top and bottom side of the Nest. The readout will be attached to the front faces of the crystals. The front and back side of the Nest will be covered by four cubic crystals each. The scintillation light of the cubic crystals can be detected from only one side.

The optimal readout device should provide a good energy resolution with CsI:Tl crystals, have low radioactive contamination and be compact in size. Reported resolutions of other experiments using CsI:Tl crystal with different readout devices help to estimate the expected energy resolution.

However, the listed resolutions in chapter 4.2.3—"Energy resolution" can give only an orientation for these crystal sizes. Especially comparisons between different readout devices for scintillators of less than one cm^3 are not valid for crystals of a few hundred cm^3. The limited dimensions of semiconductor readout devices in comparison to the crystal surface worsens the energy resolution.

GEANT4 APPLICATIONS CSI

The Geant4 application "CsI" contains a PhysicsList similar to the previous described "Scintblock". An OpticalPhysicsList was introduced as additional class for simulating the scintillation process. It defines a new particle class, the optical photon, and new processes, like the absorption Process (G4OpAbsorption()), Rayleigh scattering (G4OpRayleigh()), boundary processes (G4OpBoundaryProcess()), scintillation (G4Scintillation()), Cerenkov radiation (G4Cerenkov()) and wave length shifting (G4OpWLS()). These classes are described in [48, 49].

A single CsI crystal ($5\times5\times20\,\mathrm{cm}^3$) was constructed in a volume filled with air. It is wrapped in a layer of MgO and attached to a readout device at the two narrow faces of the scintillator. The readout device is simulated by a thin glass plate of 0.625 mm and an Al layer of the same width.

The incident photons are initialized outside of the scintillator material and hit the crystal surface in the middle between the two readout devices, perpendicular to the surface. The introduced optical photons are produced in the scintillating material after the deposition of energy by

the incident ionizing particle. Therefore, the scintillation properties of a material must be defined. These properties are the spectral distribution of a possible slow and fast component of the scintillation light, the refractive index and the absorption length as a function of the photon energy. The scintillation light yield, fast and slow time constants and the ratio of these time constants must also be defined. The values of the wavelength dependent material properties are linked to the corresponding momentum of the optical photon. The emission spectrum is between 1.2399 eV (1000 nm) and 4.1329 eV (300 nm) [36]. The index of refraction increases over this range of energy from 1.760 to 1.979 [50]. A quenching factor of kB = $2.3{\cdot}10^{-3}$ gMeV^{-1}cm^{-2}, as quoted by Tretyak [31] for CsI:Tl, was used.
Corresponding to these definitions, a number of Gaussian-distributed optical photons are initialized isotropically at the point of interaction. These photons can be absorbed or reach the crystal surface. At medium boundaries, optical photons can be reflected or refracted. For a perfectly smooth surface between two dielectric mediums, the refractive index is sufficient. All other surfaces must be defined separately. The Geant4 surface can be of two types, a skin surface (surrounding one logical volume) and a border surface (being the boundary between two logical volumes). An optical surface requires the definition of a G4OpticalSurfaceModel, a G4OpticalSurfaceFinish (polished, ground, polished- and ground-, back- or front-painted) and to specify the surface as boundary between dielectric-metal, or dielectric-dielectric materials. The reflectivity of the surface can be defined between 0.0 (no reflection) and 1.0 (no transmission). In this simulation, a 0.5 mm layer of MgO surrounds the crystal. This boundary surface was defined as polished-frontpainted (polished surface with reflector attached without air gap) with a reflectivity of 0.98 for MgO [28]. The optical photons can reach the readout device directly or after several reflections at the crystals boundary.

The Al layer, presenting the photo cathode, is defined as sensitive detector volume. The detection of optical photons differs from that of other particle classes. The optical photons are not detected after absorption, but in the optical boundary process by passing the boundary surface. The detection is based on the definition of the detection efficiency on the skin of the sensitive volume. The boundary between the glass and the Al layer is defined as polished and dielectric-metal. The reflectivity is zero and the absorption efficiency is defined as shown in figure 4.10.

The quantum efficiencies for seven readout devices are defined, which are shown in figure 5.2. There are quantum efficiencies belonging to

three different PMTs, one PIN diode, one APD and two Si-PMT. The implemented PMTs correspond to Hamamatsu R669 (borosilicate window, extended red photocathode), R6094 (borosilicate window and bialkali photocathode) and a R5900 with UV Glass and multialkali photo cathode. The PIN diode is a 2x1 cm^2 S2744-08, the APD a S8664-1010 (10x10 mm^2) and the Si-PMT correspond to S10985-050C (MPPC-050C) with 6x6 mm^2 active area and four times 900 pixels and the S10985-100C (MPPC-100C) with four times 3600 pixels.

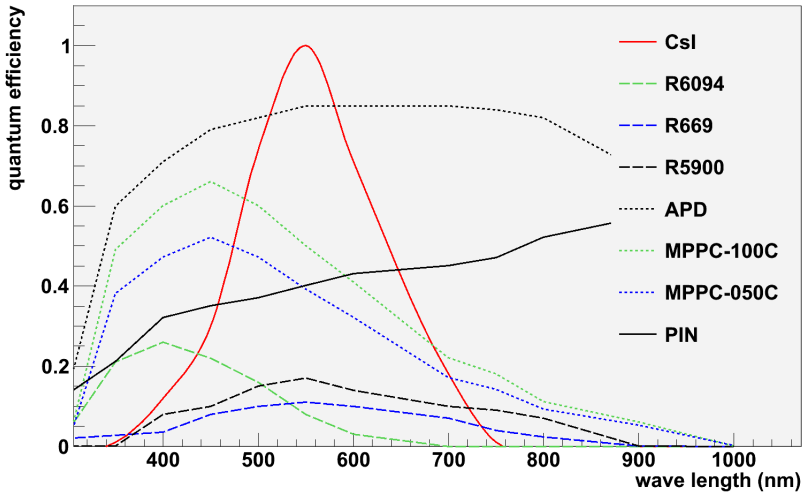

Figure 5.2: Quantum efficiencies for photo absorption of various electronic readouts in comparison to CsI:Tl emission spectrum [41].

In this application, the default geometry can be changed with messengers, redefining the crystal size, the amount of placed readout devices and the size of the readout devices. Also, optical properties, like the housing finish of the crystal surface can be set to polished with the parameter ID (1), polished-frontpainted (2), polished-backpainted (3), ground (4), ground-frontpainted (5) and ground-backpainted (6). Available quantum efficiencies are these of the PMT R669 (1), the PMT R6094 (2), the APD (3), the MPPC-100C (4), the MPPC-050C (5), the PIN diode (6) and the PMT R5900 (7). These parameters can be changed by using these commands:

```
/CsI/detector/dimensions 20.00 5.00 5.00 cm
/CsI/detector/pmtRadius 2.5 mm
/CsI/detector/nx 0
```

```
/CsI/detector/ny 1
/CsI/detector/nz 1
/CsI/detector/housingfinish 6
/CsI/detector/reflectivity 0.98
/CsI/detector/qe 7
```

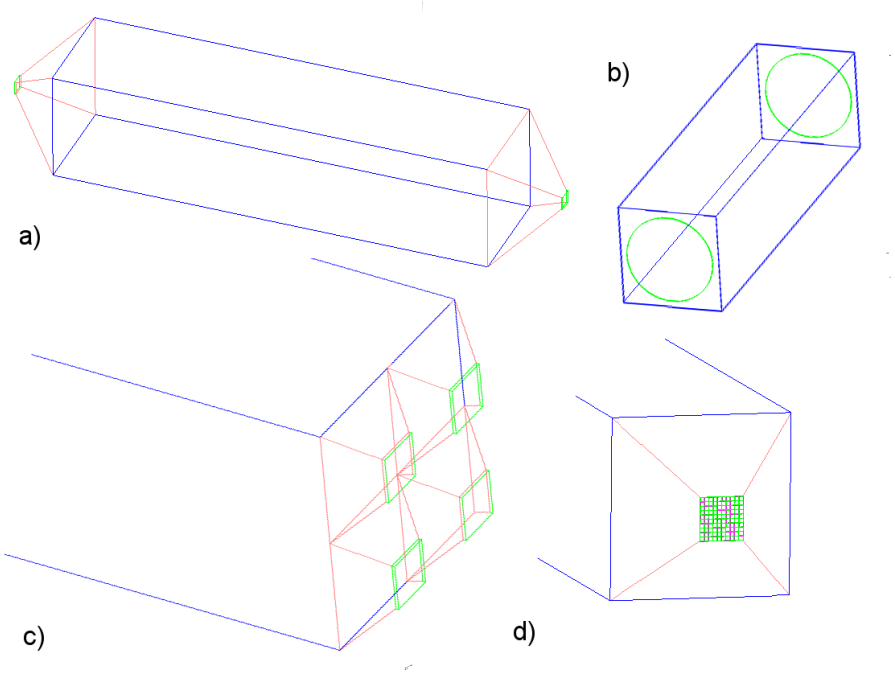

Figure 5.3: Visualisation of the constructed CsI crystal geometry. a) 5x5x20 cm^3 crystal with attached lightguide and APD. b) Crystal with round PMT. c) Crystal with 4 lightguides and APDs. d) Si-PMT with only 100 pixels, attached via a light guide to the crystal.

The glass plate is placed directly at the crystal surface and the Al layer is placed behind the glass plate. It will always be placed in the middle of the crystal side, multiple readout devices are placed regularly on the surface. Si-PMTs are realised as one device with quantum efficiencies, taking the dead layers between the pixels into consideration. The simulation of pixelated Si-PMT is also possible, by setting the corresponding pixel number and size. The command `/CsI/detector/mppc` enables a placement side by side in the middle of the crystal side.

The command `/CsI/detector/lightguide` places one or more light guides between the crystal and the glass. The front side of the light guide will decrease with an angle of 60° towards the readout de-

vice. The length of the light guide depends on the number of devices and the readout size. A visualisation, using the visualisation system Heprep, is shown in fig. 5.3.

With this developed Geant4 application, different aspects of the scintillation detector preparation were studied.

DATA ANALYSIS

Before starting the comparison between the readout devices, the influence of the housing finish, reflectivity and absorption length was studied. Therefore all 6 different kinds of housing finish were simulated with a PMT readout, covering the front faces of the crystal. The finish "polished" yields highest amount of photo electrons. Ground, ground- and polished-frontpainted yield around 75 % of the previous amount of photo electrons. The ground- and polished-backpainted finish only around 60 % of the photo electron yield, obtained with a polished surface.
The influence of the surface finish on the uniformity of the signal for different source positions was not studied, but a higher uniformity of light collection for ground, than for polished surfaces is expected [29].
The further simulations were carried out with a ground surface finish and a reflectivity of 0.98.
As main examination, the amount of photo electrons detected by different readout devices was evaluated. Therefore these 7 readout devices were simulated with different sizes of active area. In a first simulation, the readout devices covered the entire front facing crystal side, in another simulation, only commercially available sizes for the readout devices were taken into account. 10000 events with 662 keV photons were simulated and the amount of produced photo electrons was only recorded if the incident photon was completely absorbed. This was the case for about 5900 events. The mean values of the recorded photo electron number and the relative standard deviation for the different readout areas and quantum efficiencies are listed in table 5.5.

RESULTS

The crucial point of this simulation is the limited knowledge about the actual optical properties of individual crystals. This simulation can therefore give only an estimation of the expected numbers of detected photo electrons. Properties, like the optical absorption length, depend on the crystal quality and production process. The increase of the optical absorption length from 10 cm to 100 cm, improves the simulated amount of detected photons significantly by almost a factor of 10. This simulation is nevertheless useful for comparing the spectral matching and the influence of the size of different readout devices.

kind of out device	device number	size of active area	pe/keV	σ/pe (%)
PMT	R6094	25 cm^2	4.05	2.07
PMT	R5900	25 cm^2	4.50	1.99
PMT	R669	25 cm^2	2.60	2.52
APD	S8664-1010	1 cm^2	1.96	2.87
Si-PMT	S10985-100C	0.36 cm^2	1.71	3.16
Si-PMT	S10985-050C	0.36 cm^2	1.34	3.57
PIN	S2744-08	4 cm^2	3.39	2.26
APD'	S8664-1010	25 cm^2	24.53	1.13
Si-PMT'	S10985-100C	25 cm^2	15.11	1.29
Si-PMT'	S10985-050C	25 cm^2	11.83	1.39
PIN'	S2744-08	25 cm^2	11.76	1.40

Table 5.5: Photo electron yield and relative standard deviation of the photo electron yield at 662 keV for quantum efficiencies of different readout devices. Different sizes of active areas were considered, by using size of one commercial device (A) and size of 25 cm^2 (A').

In table 5.5, it is shown, that semiconductor readout devices, especially the APD are superior to PMTs with the same active area. The APDs produce more photoelectrons than silicon PMTs and PIN diodes, due to a higher quantum efficiency than PIN diodes and a larger active area than Si-PMTs, which have dead layers between individual pixels.

If only one commercially available readout device is attached to the crystal, the PMT, having by far the biggest active area, can detect more photo electrons than the other readout devices.

This correlates with the relative variation of the amount of detected photo electrons, which has the main influence on the obtained energy resolution. The smallest relative variation of produced photo electrons have 25 cm^3 APDs with 1.13 % (RMS) and PMTs of about 2 % for commercial sizes. Single APD have a photo electron yield variation of 2.9 %, which is about one third more than the variation of PMTs. It can be seen, that PMTs with bialkali photo cathode still detect more photons than commercial APDs and Si-PMTs.

The obtained photo electron yield variation considers the statistical variation of the production of optical photons, the variations of the col-

lecting efficiency and the variation of the production of photo electrons in the readout device. It can be enhanced by nonisotropic emission centre densities, which depend on the crystal quality.

The multiplication process of photo electrons within the readout device contributes to the final energy resolution, but it was not considered here. PMTs usually have smaller variations in the multiplication process than APDs. For all APDs and especially PIN diodes electric noise can deteriorate the reachable energy resolution. This must be taken into account for further considerations, but was not possible to study during this thesis.

Also, position dependent collection efficiencies were not considered in this simulation, as the particle source was a beam, hitting always the crystal centre. The linearity of the photo electron yield in dependence of the photon source position should be investigated further. Therefore the influence of different readout dimensions, crystal wrapping and the use of light guides can be studied in order to obtain a detector assembly with high light yield and good linearity.

Altogether, this comparison between the different readout devices cannot predict the energy resolution of the final scintillation detector, but can provide an informative basis to understand the processes leading to the variation of the photo electron production. Although the APD and PMT are expected to provide superior resolution in comparison with single Si-PMTs, which have a higher photo electron yield variation, due to their small size. For a final decision measurements are nevertheless necessary. Besides the PMTs, which are too big and contain too many radioactive isotopes to be used at the experiment, APDs are the favoured option, provided the strong temperature dependence of the gain can be handled.

It must be considered, that simulations of optical photons can enhance the simulation time significantly, because the path of several 10000 optical photons per MeV must be simulated.

5.2 The design

The considerations of the previous section 5.1—"Monte Carlo studies for the upgrade design" lead to an design with twelve $5\times5\times20\,\mathrm{cm}^3$ and eight $5\times5\times5\,\mathrm{cm}^3$ crystals. These are arranged as shown in figure 5.4. Four scintillator blocks are placed on a ground plate. A newly designed Nest is placed on the inner two scintillators. The Nest is surrounded by two crystal blocks on the left and right side and four crystal cubes on the front and back side. The crystals are place on top of one another. The upper four scintillators are placed on a delrin plate, being fixed with pins at the outer side of the crystals. The four cubic crystals on the front side will have a reduced height, to allow the high voltage and signal cables of the CZT detectors and Teflon tubes to lead through. The necessary size for the cable feed is not yet known, owing to still running studies to decide the cable types.

The new Nest was designed by Ebert [51]. It consist of 2 mm thick delrin plates and delrin holders of 10 mm edge length. Five Teflon tubes will feed into the side walls of the delrin Nest, being used for calibrations and nitrogen flushing. The tubes are bond to the Nest and lead between the layer, horizontally from the front left to the back right edge of the Nest, passing the middle over or under a CZT layer. This way, wire-moved calibration sources can be inserted into the setup without opening the apparatus. The tubes will also be used to flush the Nest with nitrogen in order to reduce the radon level and to cool down the inner Nest. The proposed Nest is shown in fig. 5.4.

The Nest will be housed in a layer of copper, which again will be surrounded by lead. Beyond this the Faraday cage and neutron shield will not change from those described in [52].

5.3 Monte Carlo studies of the designed upgrade

In this step the efficiency for detecting the expected double beta decay signal is estimated. Therefore the COBRA Geant4 application VENOM was expanded. Afterwards the neutrino accompanied double beta decay of ^{116}Cd and expected background was simulated. The CsI crystal background will be discussed in more detail, whereas the background from ^{222}Rn in the Nest air, and contamination of the CZT passivation and the glass of possible readout electronics was analysed only quali-

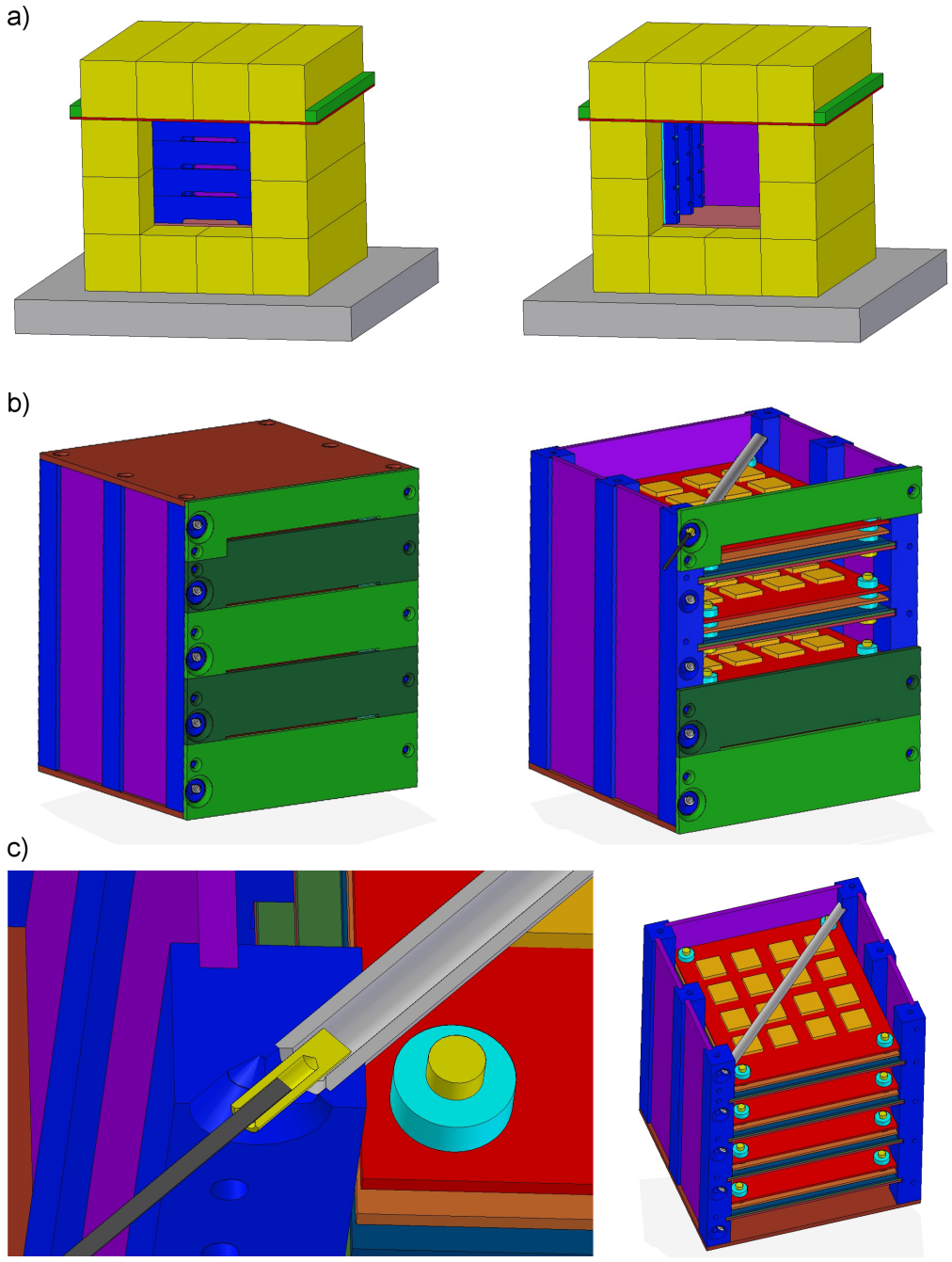

Figure 5.4: Planned scintillator assembly with delrin Nest, containing 64 CZT detectors. a) Twelve CsI:Tl blocks, surrounding the delrin Nest, can be seen, with the upper four scintillators lying on a delrin plate. b) Planned delrin Nest, with cable feed through at the front side and CZTs visible inside the Nest on delrin holders. c) Five Teflon tubes for calibration and nitrogen flushing will feed into the Nest. Drawings from Ebert [51]

tative.

5.3.1 Implementation of CsI detectors in Venom

VENOM is the Cobra simulation framework, first developed by H. Kiel [8] and redesigned by J. Wilson and B. Morgan [53]. It is a Geant4 application, enabling reproducible simulations of signal and background physics processes in the detector for all COBRA collaborators. Venom contains packages, which can be added and extended by the user. All packages use the same physics class (`VXPhysicsList`) and material class (`VXMaterials`). Geometry, action, readout and generator classes can be added by writing new packages.

THE SCINT64 PACKAGE was written as part of this diploma thesis. It is a new Venom package, constructing a simplified scintillator upgrade design. The simulated construction does not consider the cable and Teflon tubes, neglects the delrin layers, that hold the upper CsI crystals and simplifies the read out electronics of the scintillators. In the Geant4 simulation, twelve scintillator blocks of $5\times5\times20\,\mathrm{cm}^3$ and eight cubes of $5\times5\times5\,\mathrm{cm}^3$ surround a delrin Nest. These are attached to one (for cubes) or two (blocks) borosilicate glass, representing the PMT window. The other four or five sides of the scintillator are painted with a 0.5 mm thick MgO layer. Only a preliminary Nest-design, instead of the current design is implemented. It consists of 2 mm delrin plates and has an open front side. A visualisation of the constructed assembly is shown in figure 5.5.

The Scint64 package uses the PhysicsList of Venom. It considers therewith a wide range of physical processes [53], without considering optical photons. The simulations of the previous section showed, that simulations of a few 10000 optical photons per deposited MeV particle energy, do enhance the simulation time significantly. As the background estimations for rare processes can require the simulation of several hundred million of events, a description without optical photons was preferred. The energy deposition in each crystal is recorded separately. This data is called raw Venom data and provides no energy resolution.
In this package, the quenching of the scintillation light output for alpha particles is also considered and used a Birks factor of $kB = 2.3 \cdot 10^{-3}\,\mathrm{gMeV}^{-1}\mathrm{cm}^{-2}$ for CsI:Tl as reported by Tretyak [31].

At run time, a reduced energy of the alpha particles, according to their

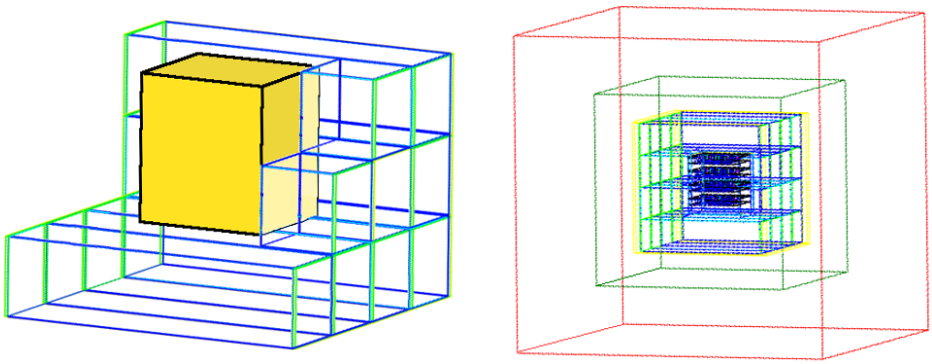

Figure 5.5: Heprep visualisation of scint64 with (left) scintillator crystals and inner cavity, containing the Nest and Nest air and (right) whole constructed assembly with (from out to inside) lead and copper shield, scintillator crystals, delrin Nest, containing delrin crystals holders and CZT crystals.

stopping power, is recorded after each step.
The kind of the ionising particle is also important for a possible background reduction with pulse shape discrimination. 99 % of all alpha particles in the CsI scintillator can be identified with a pulse shape discrimination [32]. The particle type information can therefore be used to veto the majority of all alpha decays in the scintillator volume. It is recorded in this package in addition to the energy and scintillator ID for the sensitive scintillators, but not used in this analysis.

Different kinds of radioactive decays in the extended COBRA detector can be simulated with VENOM, using macros. These macros define the used VENOM package, change the constructed geometry, define the kind of particle gun and confine the area, where events are initialised. A set of macros for the Scint64 package, which can be further used as set of default macros, were prepared. Accordingly, they initialise the Scint64 geometry, which is not changed by other commands. Three different particle guns are used for initialising double beta decays (Decay0), decays of the natural decay chain (Chaingen) and events caused by decays of single isotopes (Bkkgen). The area of these decays can be confined to certain geometric areas, points or logical volumes. The double beta decays are initialised in the CZT detector volumes. For this thesis, the background sources were only initialised in the CsI detector volumes, the CZT detector passivation, the Nest air and the PMT glass volumes. Of these, only the contamination of the CsI detector volumes were considered in detail and the other sources were just studied super-

ficially. A more detailed background study, as done by M. Heine [54] and previous works was not performed. They require a more detailed knowledge about the efficiency of the nitrogen flushing and the CZT colourless paint and scintillator read out contamination level. These examinations or not necessary at the current stage, where primary the suitability of the scintillator is to be determined.

Detector processes, leading to an energy resolution or even position dependent energy resolution are not implemented in VENOM. The energy spectra, produced by VENOM, were convoluted by a Gaussian with an energy dependent standard deviation for each detector type.

The used detector resolutions for the CZT and CsI:Tl detectors are:

$$\text{CZT}: \ \frac{\sigma}{E} = \frac{3.787286}{E} + 0.013377 \quad [54] \tag{5.1}$$

$$\text{CsI}: \ \frac{\sigma}{E} = \frac{0.58}{\sqrt{E}} + 0.019 \quad [43] \tag{5.2}$$

The CsI resolution function was published by Kim et al. [43] for similar crystal sizes and PMT readout. It was used for both sizes of scintillation detectors. Although the upgrade is planned with semiconductor readout, this resolution was used to estimate the expectable efficiency. The used resolution function of the CZT crystals is expected to be worse than the resolutions of the soon installed 64 CZT crystals.

For this study, the raw VENOM data is convoluted with a Root routine. Afterwards the convoluted data is analysed with regard to the amount of deposited energy in a single or all detectors and the number of involved detectors. It is analysed in order to find cuts with high detection efficiency for the decay signal and a low background count rate. The emphasis lies on coincident events in the CZT and CsI detector, which are unlikely to be imitated by the majority of background sources.

5.3.2 $2\nu\beta\beta$ signal

At first the signal, the neutrino accompanied double beta decay of ^{116}Cd into the first excited state, was studied.

$$^{116}\text{Cd} \rightarrow ^{116}\text{Sn}(2^+) + 2e^- + 2\bar{\nu}, \ E^* = 1294\,\text{keV}. \tag{5.3}$$

This transition was not measured for ^{116}Cd yet. The current upper limit of the half life is $2.4 \cdot 10^{21}$ years (90 %C.L.) [12]. Accordingly, the amount

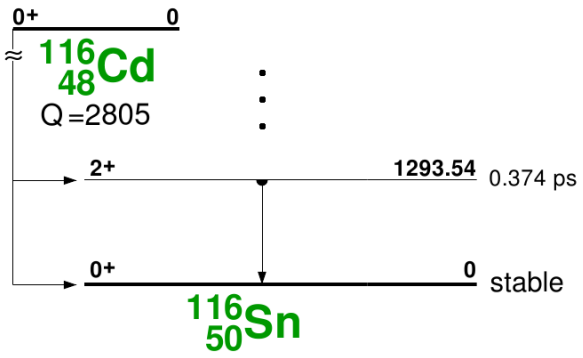

Figure 5.6: Decay scheme of ^{116}Cd [16]

of these decays in all 64 $Cd_{0.9}Zn_{0.9}Te$ of each 6.5 g is expected to be smaller than 20 events per year.

The Q-value is 2805 keV and the end point of the sum energy spectrum of the e^- pair is 1511 keV. The first excited state of ^{116}Sn is at 1294 keV, which is a 2^+ state with a twofold forbidden transition to the ground state and a half life of 0.37 ps [16].

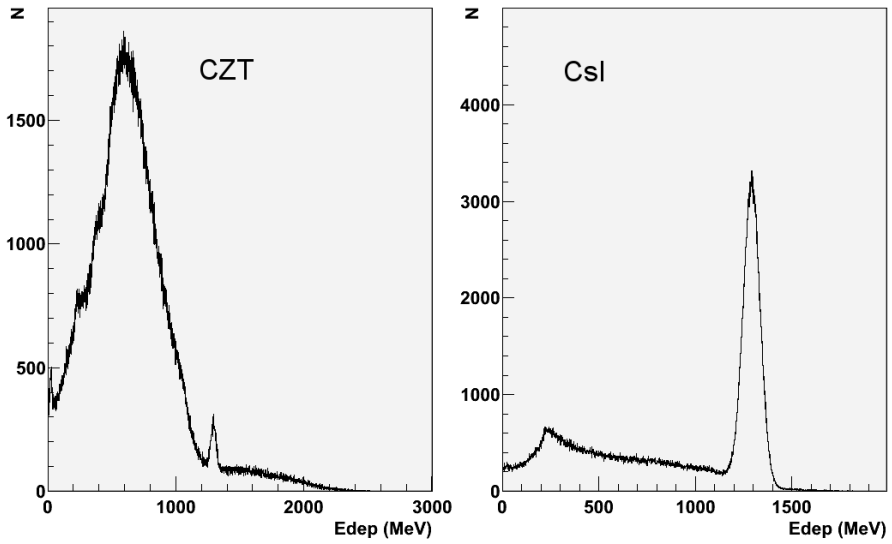

Figure 5.7: Spectrum of deposited energy in CZT detectors and sum of the deposited energy in CsI detectors.

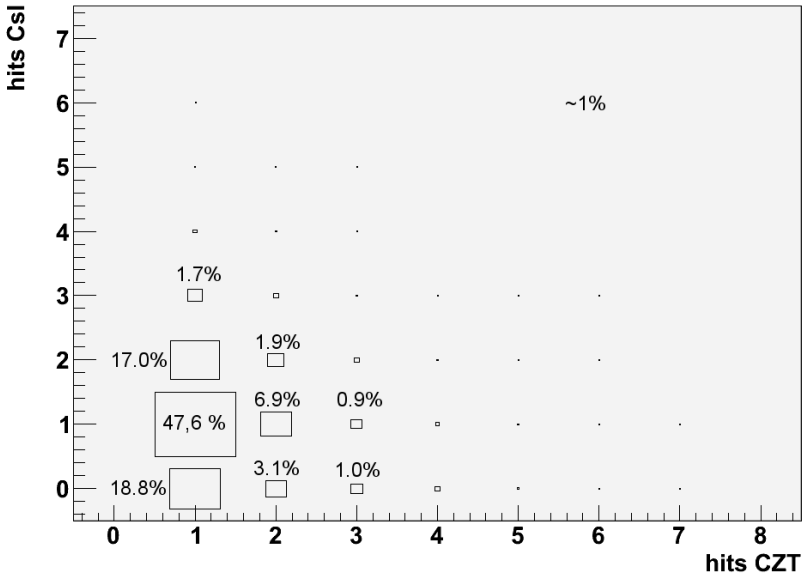

Figure 5.8: Distribution of the number of involved CZT and CsI crystals for ^{116}Cd decays into the first excited state of ^{116}Sn.

One million decays were simulated in the CZT crystals. The spectrum of deposited energy in all CZT crystals (left side of figure 5.7) shows the energy deposition of both electrons in the source CZT crystal up to 1511 keV, with the maximum around the expected $0.32 \times Q$. The full energy peak of the 1294 keV gamma ray, absorbed in a second CZT, and the deposition of the electron and a part of the gamma energy in the source crystal is visible. The CsI sum spectrum (right side of figure 5.7) shows the 1294 keV full energy peak and a Compton spectrum up to 1080.7 keV, overlaid with the backscatter peak at 213.3 keV. It can be assumed, that hardly any electrons leave the CZT crystal.

The distribution of events, depositing energy in the CZT and CsI crystals is plotted in figure 5.8. 23.2 % of all events are not detected in the CsI crystals. This correspond with the from section 5.1.1—"Scintillator size" determined ≈70 % total efficiency, which was determined only for photons, hitting a flat scintillator perpendicular to the input face and is therefore expected to be higher for this geometry.
A simulation of 1294 keV photons, being initialised in the CZT detectors, showed that 17.7 % of these photons are interacting neither with the CZT, nor with the CsI detectors.

In 3.1 % of the simulated double beta decay events, two CZT and no CsI crystals were involved. 1 % of all double beta events deposit energy in a 3σ interval around 1294 keV in one CZT crystal and an energy of less than 1511 keV in another CZT crystal.

76.77 % of all ^{116}Cd decays into the first excited state produce coincident hits in the CZT and scintillation detectors. 47.60 % and 17.00 % of all events deposit energy in one CZT and one or two CsI crystals. Further studies will consider coincident hits with one CZT and one or two CsI detector hits, being 64.6 % of the total amount of events. Coincident hits are defined in the simulation as hits in the CZT and CsI detectors, that belong to one event, whereas in the experiment these will be hits (belonging to a single decay or not) in multiple detectors within a time window of several tens of μs. For low count rates and small time windows, random coincidences are strongly suppressed.

Events with deposited energy of up to the electron endpoint energy of 1511 keV in one CZT detector and an energy deposition of around 1294 keV in the CsI detectors are the majority of all coincident events. By considering an interval of 3σ (5σ) around the 1294 keV gamma line in the CsI detectors 43.4 % (50.8 %) of all coincident (1CZT and 1&2CsI) events and 28.0 % (32.9 %) of all signal events are included.

In figure 5.9 the deposited energy of the CZT is plotted against the energy entry of the scintillation detectors, if only one CZT and one or two CsI crystals were involved.
The red lines mark a distance of 3σ to the expected full energy deposition of the 1294 keV photon in the CsI crystal. The standard derivation from equation (5.2) at 1294 keV was used. The interval between the red limes contains 99.7 % of all energy depositions with an expected value of 1294 keV.

Cut	E_{CZT} (keV)	$E_{CsI}(keV)$	$E_{CZT} + E_{CsI}$ (keV)	ϵ (%)
A-3σ	-	1231-1357	-	28.0
A-5σ	-	1190-1398	-	32.9
B-3σ	-	1231-1357	>2200	2.9
B-5σ	-	1190-1398	>2200	3.4
C-3σ	300-900	1231-1357	-	26.2
C-5σ	300-900	1190-1398	-	27.6

Table 5.6: Efficiencies for different cuts for events in one CZT and one or two CsI detector.

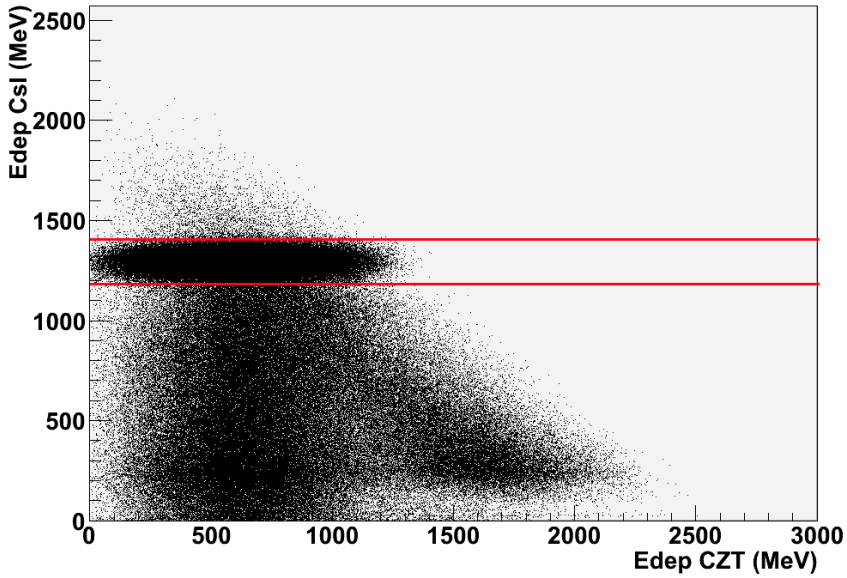

Figure 5.9: Energy deposition of about 6.5×10^5 coincident ^{116}Cd events in one CZT and one or two CsI detector, with marked 5σ interval around the 1294 keV entry in the CsI detectors.

5.3.3 Background contamination in CsI crystal

Several radioactive isotopes can be found in CsI crystals. The KIMS collaboration [42] investigated the contamination levels of commercially available CsI(Tl) crystals. The main contamination were ^{137}Cs, ^{134}Cs and ^{87}Rb, whereas isotopes of K and Na were negligible [43]. Lee et al. [42] describe the reduction of internal background of CsI:Tl crystals and achieved contamination levels listed blow [55].

Contamination levels for ^{238}U and ^{232}Th of only 0.75 ppt and 0.38 ppt

isotope	commercial contamination level	first reduced contamination level [42]	second reduced contamination level [55]
^{137}Cs	18-210 mBq/kg	15.5±2.6 mBq/kg	7.5 mBq/kg
^{134}Cs	38-586 mBq/kg	27.4±4.6 mBq/kg	14.1 mBq/kg
^{87}Rb	3.2-816 ppb	20±1 ppb	11.8 ppb

Table 5.7: Contamination levels of commercially available CsI:Tl detectors and of achieved resolution in 2006 and 2007 [42, 55].

were reported [55]. Of these contamination only ^{134}Cs and events of the U and Th decay chains have high enough energy for concealing the double beta signal. The influence of ^{137}Cs and ^{87}Rb were considered nevertheless, because their signals can pile up with other background sources.

^{134}**Cs** is an anthropogenic isotope with a half life of 2.06 years, but can also be produced by the ^{133}Cs$(n,\gamma)^{134}$Cs reaction with a thermal neutron capture cross section of 25.8 barn [56]. The beta decay of ^{134}Cs (Q=2.059 MeV) can be observed by detecting correlated 604.7, 795.8 keV γ rays and an electron with the endpoint energy of 658.1 keV. Other decay modes are also possible, see figure 5.10.

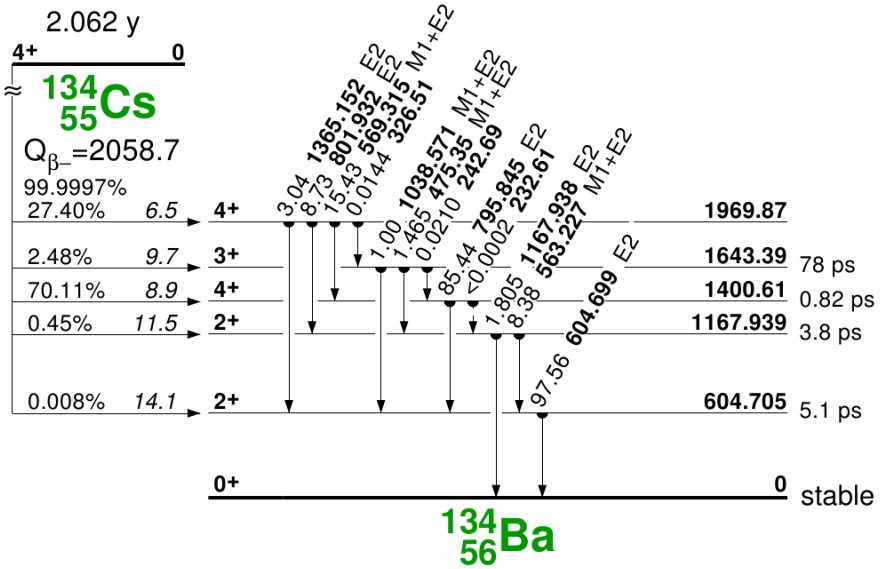

Figure 5.10: Decay scheme of ^{134}Cs [16]

Lee et al. [55] measured a contamination level of 14.1 mBq/kg, leading to 1.2×10^7 ^{134}Cs events in the proposed COBRA upgrade during the first year.

The entries in the CZT detectors occur only in 3.16 % of all ^{134}Cs decays. In the case of coincident events in the CZT and the CsI detectors, mainly one CZT and one (0.43 %), two (1.08 %) or three (0.79 %) CsI detectors are involved. The CZT crystals have full energy peaks for the 604.7 keV and 795.8 keV gamma ray and entries up to 2000 keV. The energy deposition in the CsI detectors shows mainly the prominent two

gamma lines and a beta spectrum, overlapping with these lines to energies of up to 2300 keV. Figure 5.11 shows the deposited Energy in CsI (plotted at the abscissa) and CZT (plotted at the ordinate) for coincident events.

number of involved detectors	absolute number of ^{134}Cs events	ϵ (%)
1CZT&1CsI	5.20×10^4	47.66
2CZT&1CsI	1.38×10^4	6.89
1CZT&2CsI	1.29×10^5	17.01
2CZT&2CsI	2.31×10^4	1.91

Table 5.8: Absolute numbers of ^{134}Cs background events in the first year and the detection efficiency for the ^{116}Cd decay into the first excited state.

Table 5.8 lists the numbers of ^{134}Cs background events in the first year and the detection efficiency for the ^{116}Cd decay into the first excited state in dependence of the number of involved detectors. For coincident events in CZT and CsI detectors, the combinations of 1 and 2 CZT and CsI detectors were listed. The total detection efficiency for the regarded double beta decay and coincident CZT and CsI events is highest for 1CZT&1CsI. It has a ^{134}Cs background rate of 5.20×10^4 events in the first year. The efficiency at 1CZT&2CsI is with 17 % the second highest, but the background is nearly three times higher. Events in 2CZT&1CsI have a 7 times smaller efficiency, but only a nearly 4 times smaller background than 1CZT&1CsI events. 2CZT&2CsI events have lower efficiencies and higher background than the previous 2CZT&1CsI events. In order to decide whether the detection of this double beta decay events is possible, only events in 1CZT&1CsI and 1CZT&2CsI configurations are now regarded further, being together the majority of the simulated double beta events.

Applying the cut from figure 5.9, being within the 5σ energy interval of the 1294 keV line in the scintillator, 0.29 % of the ^{134}Cs events survive, being nearly 35000 events per year. This background component is therefore very harmful. An additional cut, demanding a sum energy of the entries in the CsI and CZT detector of more than 2200 keV, reduces this background to zero. This cut also reduces the detection efficiency for the double beta decay significantly from former 33.13 % to 3.14 %, making even a direct detection of the maximum expected signal of around 20 events per year difficult.

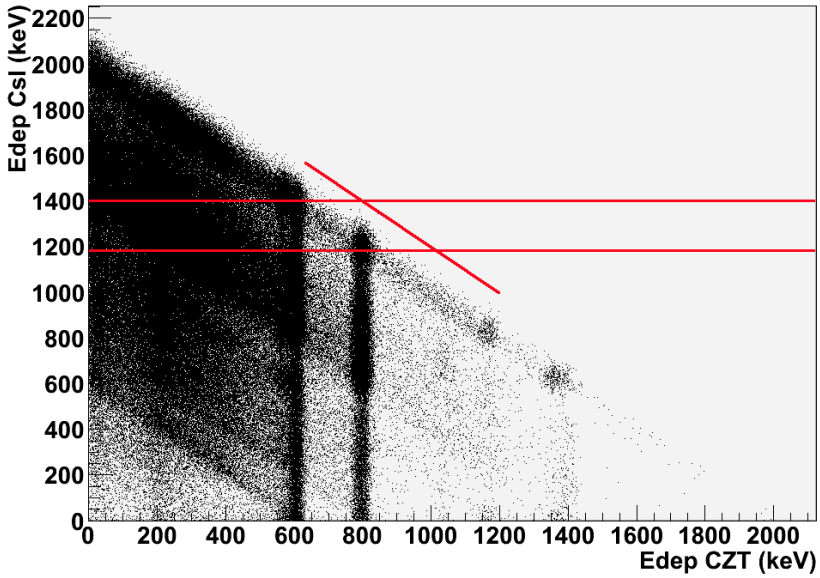

Figure 5.11: Energy deposition of about 1.8×10^5 coincident ^{134}Cs events in one or two CZT and CsI detectors, with marked 5σ interval around the 1294 keV entry in the CsI detectors.

The background contribution of ^{134}Cs for events with more than two involved detectors can be reduced by considering the angle correlation of the subsequent gamma rays. After a ^{134}Cs decay, the majority of gamma rays are emitted at a $4^+ \rightarrow 2^+ \rightarrow 0^+$ transition with a correlation of the emitting angle between both photons of $W(\theta) \propto 1 + \frac{1}{8}cos^2\theta + \frac{1}{24}cos^4\theta$. This favours emission in the same or opposite directions. Up to now, the only information of the interaction position is the involved detector number. An analysis, considering the angles between the in one event involved detectors is, owing to the big dimensions of the CsI crystals in comparison to the small distance between different detectors, not possible. However, the distribution of hits in neighbouring and not neighbouring CsI crystals was studied. It showed, that the regarded double beta decay leads to more hits in neighbouring and next neighbouring CsI crystals (for events, involving one CZT and two CsI crystals) than ^{134}Cs decays. Four categorisations are distinguished, being neighbouring crystals, which have a joint surface (N), next neighbouring crystals with a joint edge (NN), crystals at opposite sides of the Nest, having joint surfaces with the Nest (O) and crystals, being not in the former categorisation (R). The distribu-

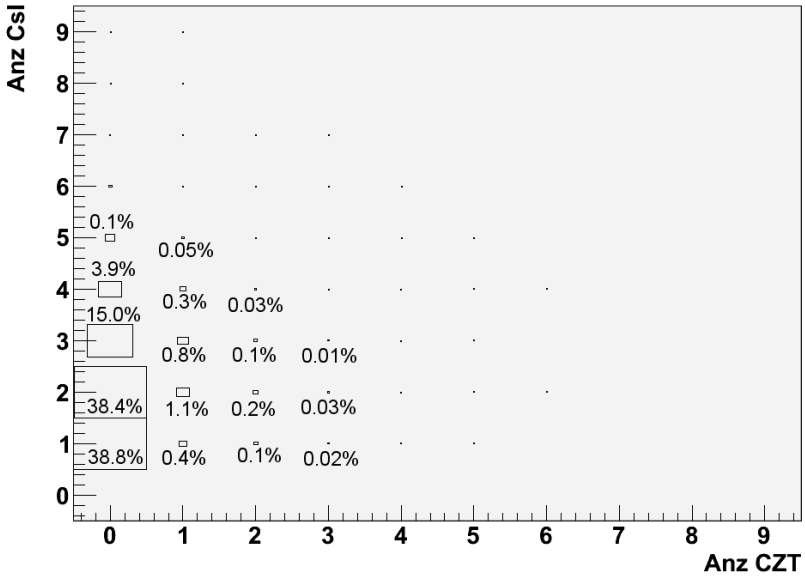

Figure 5.12: Distribution of the number of involved ^{134}Cs events

tion of events is listed in table 5.9. The restriction to neighbouring CsI crystal reduces the detection efficiency for the regarded double beta decay from 17.01 % to 13.31 %, while reducing the background rate by a factor 2 to 6×10^4 counts/year for this configuration and without further cuts. Regarding also the source CZT crystal position improves the background reduction further, but not significantly with the bad position information for events in CsI crystals.
The background reduction, using the information of angle correlated gamma rays, is more efficient for events with better position resolution, like multiple CZT detector hits. Kim et al. [43] cited position resolutions of less than 1 cm for the crystal length. For the scintillator blocks, this reduces the position information from an former volume of $20 \times 5 \times 5\,\mathrm{cm}^3$ to a volume of $1 \times 5 \times 5\,\mathrm{cm}^3$. It should be studied whether this can reduce the background rate sufficiently.

Kim et al. [56] reported their studies about contamination and inhibition of ^{134}Cs in CsI powder. In contrast to ^{137}Cs, the inhibition of ^{134}Cs does not occur due to the water used during the CsI powder processing, which could contribute only a few μBq/kg. The contamination were already present in the pollucite before the Cs extraction and can also be produced in the CsI crystals and powder by the neutron cap-

crystal positions	^{134}Cs events	^{116}Cd events
N	48.32 %	78.31 %
NN	17.01 %	15.26 %
O	8.69 %	1.75 %
R	25.98 %	4.68 %

Table 5.9: Contribution of $2\nu\beta\beta$ decay of ^{116}Cd into the first excited state and background contribution of ^{134}Cs, for events with one involved CZT and two CsI detectors, categorised by positions of involved CsI crystals. Neighbouring crystals, which have a joint surface (N), next neighbouring crystals with a joint edge (NN), crystals at opposite sides of the Nest, having joint surfaces with the Nest (O) and crystals, being not in the former categorisation (R) are distinguished.

ture process on ^{133}Cs. The measured ^{134}Cs contamination in the pollucite powder of around 12 mBq/kg corresponds to an exposure time of one year of neutron flux at see level. The saturated contamination after infinite exposure with a typical thermal neutron flux at see level was reported to be about 50 mBq/kg for pollucite powder and around 80 mBq for CsI powder. Accordingly, the ^{134}Cs contamination can only be reduced by limiting the exposure to thermal neutrons. This can be achieved by storing the crystals as soon as possible underground, having short crystal production times and by storing and transporting the powder or crystal protected from thermal neutrons.

^{238}U: With a reported contamination level of less than 0.75 ppt [55], there will be only around 10000 decays from the ^{238}U chain in the extended COBRA detector (assuming secular equilibrium). One million of the events from the nat. ^{238}U decay chain were simulated and they produce only 0.13 % coincident entries in single CZT and one or two CsI detectors (1CZT-1&2CsI). This lead to about 13 expected coincident events in the detector and to about 1 event in three years in the 3σ region around the 1294 keV line in the scintillator. The ^{238}U contamination in the scintillator are therefore negligible, compared to the other background sources.

^{232}Th: An even lower ^{232}Th contamination level of 0.38 ppt was reported by Lee et al. [55], leading to around 1600 decays per year in the scintillation detectors. Of these only 0.2 % produce coincident entries in one CZT and one or two CsI detectors. These are 3 coincident events per year, and about one in 5 years in a 3σ region.

For calculations, ^{238}U and ^{232}Th decay chains in equilibrium were assumed. For the case of CsI crystals, this is not likely to be, as the different chemical and physical properties of the elements of the Th and U decay chain will lead to a broken equilibrium or single impurities and their short-lived progenies. However, as this is a background estimation, it was considered to be sufficient as an upper limit.
An analysis, considering the background reduction of 99 % of all events, emitting alpha particles in the scintillator, with a pulse shape discrimination was not used here, owing to the already small event rates. Such analyses should consider the effect of δ-electrons, which are produced by alpha particles, but lead to an electron-event like pulse shape.

^{137}Cs is an anthropogenic radioactive isotope. It is a beta-emitter, decaying with 94.4 % branching ratio and a half live of 30.07 years, to the metastable state of ^{137m}Ba. The emitted electron has an endpoint energy of 514 keV. After half life of 2.55 min ^{137m}Ba deexcites to the ground state under emission of a 661.7 keV γ. Both particles are not coincident in time. In 5.6 % ^{137}Cs decays directly to the ground state of ^{137}Ba, emitting an electron with an endpoint energy of 1175.6 keV. Deniz et al. [57] announced to reduce the ^{137}Cs contamination in CsI:Tl powder by using purified water instead of usual processing water which contained 0.1 mBq/l.

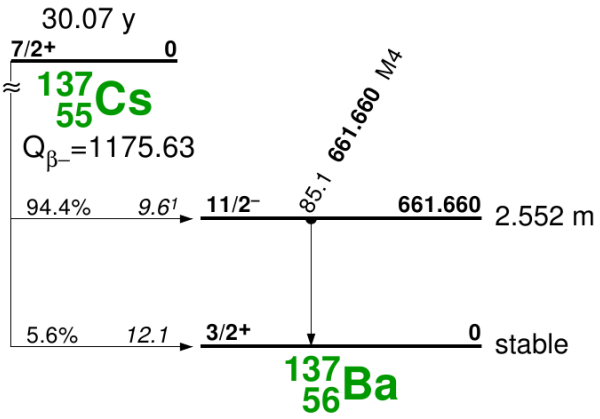

Figure 5.13: Decay scheme of ^{137}Cs [16]

The ^{137}Cs contamination is no serious background for the double beta signature. The main decay channel produces a noncoincident electron

and gamma ray which have each a much lower energy than the signature. The direct transition of ^{137}Cs to the ground state of ^{137}Ba can have only a signature similar to the double beta decay event with very low electron energy.

Simulations of a background level of 7.5 mBq ^{137}Cs, corresponding to 7.5×10^6 ^{137}Cs decays per year in the planned scintillators, producing 14.5×10^6 noncoincident events per year. This number of events was simulated and all events deposit energy in one or more CsI crystals. The majority of these events deposit energy in one (28.5 %), two (10.8 %) or three (1.6 %) scintillators. Only 1.23 % of all ^{137}Cs events have also coincident entries in the CZT detectors. 0.39 % have entries in one CZT and one CsI and 0.53 % in one CZT and two CsI.

The coincident deposited energy in CZT and CsI detectors can in figure 5.14. The energy deposition in the CsI detectors is except for small energy depositions in the CZT detectors, below the 3σ interval around 1294 keV. The maximum deposited energy in the CZT detectors around 662 keV, corresponding to the full energy deposition of the 662 keV gamma ray. The pure ^{137}Cs background contribution can already be excluded with the general CZT energy threshold of a few hundred keV. The ^{137}Cs contamination is therefore of minor importance, as long as the background level of the hole experiment is small enough to avoid a pile up with other background sources.

^{87}RB is a primordial nucleus, decaying with a half life of $4.75 \cdot 10^{10}$ years through beta decay with a Q-value of 282 keV. Natural Rb includes 27.8 % ^{87}Rb and Kim et al. [56] located contamination of 1 to 1000 ppb in different CsI powders. A reduction to 1 ppb was possible with recrystallisation of the powder with pure water. Without further reduction a contamination level of 11.8 ppb (corresponding to 12.14 mBq/kg) was reported. Accordingly 12×10^6 decays per year are expected in the extended COBRA detector. The single decays of ^{87}Rb are no serious background, but might contribute as background by pile up with other background sources.

RESULTS

These estimations show, that CsI crystal, which have not been stored underground for a few decades, cannot be easily used for searches of the neutrino accompanied double beta decay of ^{116}Cd into the first excited state of ^{116}Sn. These estimations were made for already background reduced crystals. For crystals that are not background reduced,

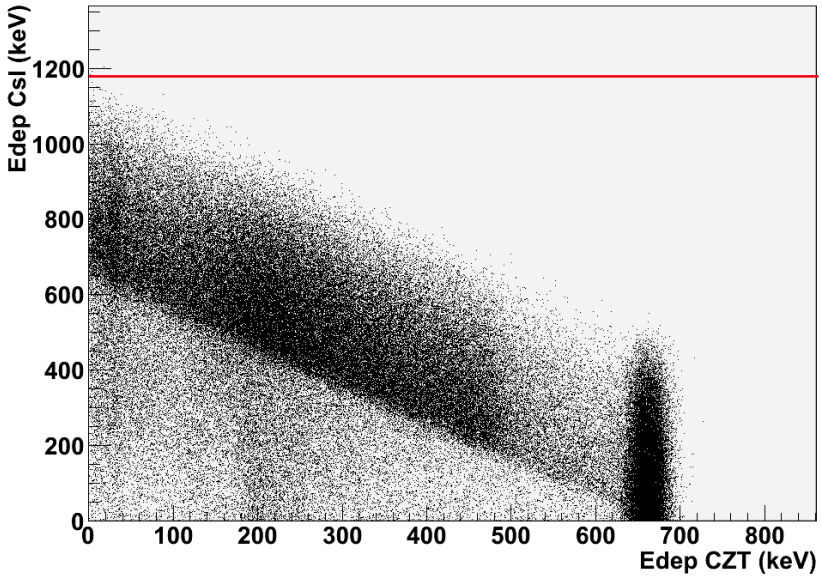

Figure 5.14: Energy deposition of about 1.8×10^5 coincident ^{137}Cs events in CZT and CsI detectors.

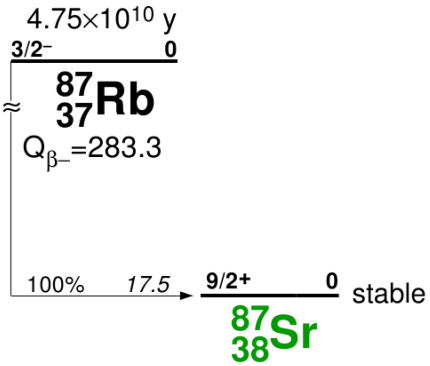

Figure 5.15: Decay scheme of ^{87}Rb [16]

background levels can be up to 40 times higher.

Background	^{134}Cs	^{238}U	^{232}Th
activity	14.1 mBq/kg	0.75 ppt	0.38 ppt
events/year	12×10^6	1×10^4	2×10^3
1CZT-1&2CsI	2×10^5	13	3
cut A-3σ	19237	<1	<1
cut B-3σ	0	<1	<1
cut C-3σ	8055	<1	<1

Table 5.10: Efficiencies for different cuts of the CsI crystal background, with <1 being one event in several years.

5.3.4 Background contamination in PMT, paint and Nest gas

PMTs with low background quartz glass windows have ^{40}K background levels of 504 mBq/PMT, 78.2 mBq/PMT from the ^{238}U decay chain and 25.5 mBq/PMT from the ^{232}Th decay chain [55]. This would result in nearly 3.2×10^8, 5×10^7 and 1.7×10^7 decays of these sources in the planned COBRA detector. Only 10^5 events of each of these sources was simulated.
^{40}K is a primordial nucleus and decays mainly into the ground state of ^{40}Ca, emitting an electron with a maximal energy of 1311 keV. 10.7 % of all ^{40}K decays lead to the first excited state of ^{40}Ar, which deexcites after about one ps into the ground state and emits a 1460.8 keV gamma ray. Its decays produce 0.04 % coincident (1CZT-1&2CsI) entries with

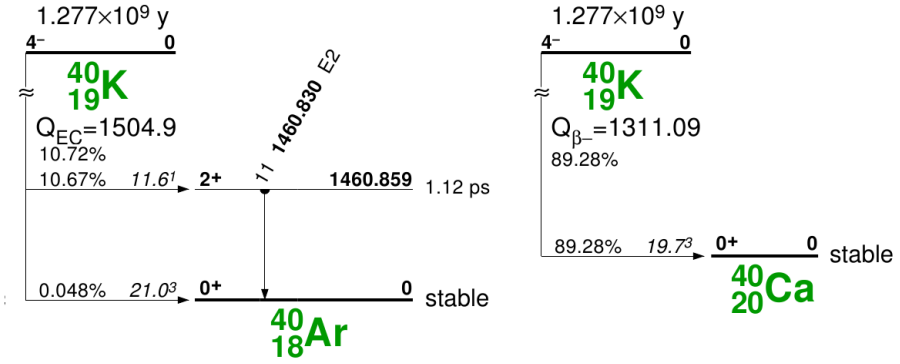

Figure 5.16: Decay scheme of ^{40}K [16]

a sum energy of up to 1550 keV, being still around 130000 coincident events per year. These are 5 times more events than ^{134}Cs events, covering the lower part of the double beta decay signal. The ^{238}U and ^{232}Th

decay chains produce 0.03 % and 0.04 % coincident (1CZT-1&2CsI) entries, being about 15000 and 7000 coincident events.
Accordingly, the PMTs could become a main source of background and their use should be avoided.

PAINT: The upper limit for contamination in the colourless paint for the CZT crystal was measured to be lower than 1.5 mBq/kg for ^{238}U, 0.6 mBq/kg for ^{232}Th and 50 mBq/kg for ^{40}K [58], resulting in less than about 220000, 11000 and 55000 decays per year (paint mass of 0.027g/CZT crystal). Less than 5 % of these decays produce coincident entries, whereas about 100 are in the cut C-3σ region.

^{222}**RN** decays with a half-life of 3.82 days, but feeds into ^{210}Pb with a half-life of 22 years. The last gamma active nuclei in the ^{222}Rn decay chain is ^{214}Bi. As Rn is a gas, it diffuses into every area with lower partial pressure. The decay product will be charged and accumulate on all surfaces. The air in the Gran Sasso laboratory can have radon activities of 35$\pm$2 Bq/m^3 [20]. The cavity in the Nest contains roughly $4{\cdot}10^{-4}$m^3, yielding about 15 mBq or half a million ^{222}Rn decays in one year. These is a maximal estimation, without nitrogen flushing. Simulation of one million events of the ^{222}Rn decay chain in the Nest air were produced. 3 % of these decays produce coincident (1CZT-1&2CsI) entries. These decays will produce about 520 events in the C-3σ region, being less than 7 % of the minimal expected ^{134}Cs background.

RESULTS

Background	PMT (K/U/Th)	Paint (K/U/Th)	^{222}Rn
activity	504/78.2/25.5 mBq/PMT	4/0.1/1 Bq/kg	35 mBq/m^3
events/year	318/50/17$\times10^6$	0.2/0.1/0.06$\times10^6$	0.5$\times10^6$
1CZT-1&2CsI	0.04/0.03/0.04 %	?/3.2/4.6 %	2.95 %

Table 5.11: List of different background sources

The detection of the neutrinoless double beta decay into the first excited state is not possible or at least very difficult with CsI crystals. The background of ^{134}Cs is more than one order of magnitude higher than the upper limits of the paint and ^{222}Rn background.

As alternative scintillator CWO or BGO should be studied. NaI:Tl is due to is small density and the preferred read out with PMTs no solution, as even background optimised PMTs are expected to be a main

source of background. For more detailed studies about the background sources beside these in the scintillation detector, further studies with more simulated events and a better knowledge of the contamination levels are necessary.

Chapter 6

Summary and future work

In this thesis possible scintillators for a COBRA upgrade were investigated. Emphasis was laid on inorganic crystal scintillators with high light yield, high stopping power, moderate price and low intrinsic background contamination. The scintillator materials NaI:Tl, CsI:Tl, BGO and CWO were short-listed. A Monte Carlo simulation and a price research helped to choose the optimal crystal size. CsI:Tl seemed to be the most promising choice and was studied further. A strong dependence of the scintillator energy resolution from the crystal dimensions, the readout area and the spectral matching of the scintillator emission spectrum and readout quantum efficiency required further studies. A second Monte Carlo simulation compared different readout devices and indicates, that a readout of CsI:Tl with APDs is possible for this crystal size. A COBRA upgrade with CsI:Tl was designed and implemented into the COBRA simulation framework VENOM. Monte Carlo studies of this upgrade demonstrated that CsI:Tl is not as suitable as anticipated for the COBRA experiment. The cosmogenic ^{134}Cs is expected to be the main background of CsI:Tl and reduces the detection efficiency for the neutrino accompanied transitions of ^{116}Cd into the first excited state by one order of magnitude. This prevents a direct detection of the $2\nu\beta\beta$-decay of ^{116}Cd into the first excited state even for half-lives, being equal to the lower half-life limit. The background contribution was reduced by considering the position of involved CsI crystals, for events with one involved CZT and two involved CsI detector. A further background reduction for all events with more than two involved detectors, by considering the angle correlations between the detectors is expected. With the current simulation, this is only promising for events with multiple CZT hits, owing to the lager CsI crystal

dimensions. Therefore, the event position reconstruction for the CsI crystals should be investigated and implemented into the Venom simulation. A background reduction for events with only one involved CZT and CsI detector, being the majority of all coincident events, but providing no angle information, should be investigated further.

The resolutions of the CZT and CsI:Tl detectors should be adjusted for following more detailed studies. For this thesis, the CZT resolution used in the analysis of Heine [54] was used and is expected to be larger than the resolution of the new installed 64 CZT crystals with colourless passivation. The position dependent resolution of the CsI:Tl crystals should be determined for both crystals sizes with semiconductor readout.

The achievable half-life limits with a CsI:Tl COBRA upgrade has to be studied in a more detailed analysis. Additionally, a future investigation of an upgrade should study CWO, comparing achievable half-life limits and prices with a CsI upgrade. CWO is with its relatively high light yield and easier handling more suitable than NaI:Tl and BGO.

To study CWO, the written Geant4 applications can be used, but has to be expanded. The application CsI must be adjusted for CWO. To add new scintillator materials, their optical properties must be implemented. This application can provide information about the possibility of attaching diodes via wavelength shifter to the CWO crystal. Due to the lower maximal emission wavelength of CWO in comparison to CsI:Tl, this might be an option.
The VENOM package Scint64 has to be adjusted also. Here, no optical properties must be implemented, but a change of the scintillator material and the geometry for smaller crystals is necessary. The already implemented Birks factor must also be adjusted for CWO. An analysis, using pulse shape discrimination is as well possible for CWO.
Further studies with this package could use different resolutions for the two different scintillator sizes or even for individual crystals. A corrected energy, depending on the point of interaction in the scintillator could also be added by later package developers.

Appendix A

FIRST APPENDIX

In this appendix, an incomplete list about the properties of various scintillating materials is presented in A.1—"Scintillator matrials". In A.2—"Reports about CsI:Tl detectors" reports about CsI:Tl detectors, concerning the achieved resolutions with different crystal sizes, readout devices and aspects of the detector mounting are listed.

A.1 Scintillator matrials

Table A.1 shows the properties of various scintillating materials. This list gives an incomplete overview about the obtainable scintillators.

Scintillator	Density (g/cm^3)	Light yield (photons/keV)	refractive index at λ_{max} [36]	λ_{max} (nm)	Hygro scopic
NaI:Tl	3.67	43	1.85	415	yes
CsI:Tl	4.51	52	1.79	560	slightly
CsI:Na	4.51	38.5	1.84	420	yes
CsI (pure)	4.51	17	1.95	315	slightly
CaI_2	3.96	86		410	highly
CaI_2:Eu	3.96	86		470	highly
BGO ($Bi_4Ge_3O_{12}$)	7.13	8 10	2.15	480	no
Gd_2O_2S:Ce	7.34	40		580	no
GSO:Ce (Gd_2SiO_5:Ce)	6.71	12.5		430	no
YAG:Ce ($Y_3Al_5O_{12}$:Ce)	4.55	11		550	no
YAG:Pr	4.55	9		310,380	no
($Y_3Al_5O_{12}$:Pr)					
YAP:Ce ($YalO_3$:Ce)	5.35	16		347	no
LYSO(Ce) ($Lu_{1.8}Y_{0.2}SiO_5$:Ce)	7.10	32	1.81	420	no
LuI_3:Ce	5.60	50		475. 520	
$LaCl_3$:Ce	3.85	49	1.8	350	yes
$LaBr_3$:Ce	5.29	61		380	yes
BaF_2	4.88	2	1.54	220(195)	slightly
BaF_2	4.88	10	1.50	310	slightly
CaF_2:Eu	3.18	21.5	1.47	435	no
$CdWO_4$	7.90	20	2.3	495	no
$ZnWO_4$	7.87	21.5		480	
$CaWO_4$	6.10	6		430	
$PbWO_4$	8.28	0.1		420	
$PbWO_4$ (ancient)					
$PbMoO_4$					
$CaMoO_4$:La	4.25	7.5		530	
$ZnMoO_4$					
ZnS:Ag	4.09	≈50		450	no

Table A.1: List of scintillators and their main characteristics from Lecoq [26],

Activity (mBq/kg)	Z_{eff}	photo abs. Coeff 511 keV cm^{-1}	X_0 (cm)	Decay time (ns)
1 [35]	50.8	0.058	2.56	230
20 [35]	54.0	0.090	2.43	1000
20 [35]	54.0	0.090	2.43	630
20 [35]				16
	51.1	0.065	2.29	550
	50.6	0.065	2.29	790
7-3000 [35]				300
	61.1	0.214	1.13	2100
1200 [35]	59.4	0.175	1.36	60. 600
1 [35]	32.6	0.017	3.28	70
1 [35]	32.6	0.017	3.28	23
1 [35]	32.0	0.019	2.20	30
$17{\cdot}10^{6}$ ^{176}Lu [35]				41
$17{\cdot}10^{6}$ ^{176}Lu [35]				31. 400. 3
21000 (^{138}La) [35]				28
21000 (^{138}La) [35]				16
2000 [35]				0.6 0.8
2000 [35]				630
10 [35]	16.4	0.045	3.72	940
600 [35]	64.2	0.262	1.21	2000
1 [35]	62.5	0.266	1.19	22000
930 [35] (Rn)				600
50000-80000 [35]	75.6	0.485	0.89	6
4 [35]				
192000 [35]				
10 [35]	35.2	0.02	1.97	18000
				110

Table A.2: if not otherwise quoted.

A.2 Reports about CsI:Tl detectors

Scintillation detectors are common used detector systems and plenty of reports describe the assemblies and achieves resolution. With an final focus on CsI:Tl scintillation detectors of this thesis, mainly reports of these crystals, comparing between different readout devices, couplings and crystal wrapping are presented.

For the BARBAR collaboration Brose et al. [39] reported photoelectron yields of CsI:Tl crystals with different crystal wrapping and readout. They used crystals of 6x5 cm^2 front face, 6x6 cm^2 rear face and a length of 36 cm.
The crystal wrapping improved the light yield and uniformity. A crystal wrapping with two layers of DuPont Tyvek 1056 D (160 μm) or three layers of 38 μm thick Teflon PTFE improves the light yield by 4 times compared to no wrapping. One layer Al foil around the two layers of DuPont Tyvek 1056 D yields an improvement of the light yield of 5 times the light yield without wrapping. The wrapping also improves the uniformity of light output and reduces cross talk between the crystals. As readout device, three different systems were used, a PMT, a PIN diode coupled directly to the crystal and diodes coupled to a wave length shifter.
The light yields of 74 % for a 5 cm diameter PMT (Hamamatsu R669) with multialkali photocathode, coupled to the rear face of the crystal with a minimal air gap, was only given in this article relative to a cubic CsI:Tl standard crystal (25 mm edge length). They measured the uniformity of light output for 18 different positions of a ^{137}Cs source (662 keV) for the PMT, being within $\pm$2%.
Thereafter two Hamamatsu S2744-08 diodes (10x20 mm^2 active area) were coupled with optical grease and glue to the rear face of the crystal. This readout yields around 8500 photoelectrons/MeV with en electronic noise level of 110 keV at the 1275 keV line of ^{22}Na. The photo peak position of a ^{137}Cs source could not be determined with the diode readout.
Finally two Hamamatsu S 3588-03 (mod 5400) with 3x3 mm^2 active area were coupled via a wave length shifter to the crystal rear face. The wave length shifter consisted of fluorescent dyes, dissolved in 3 mm thick lucite (PMMA) plates and covered the hole rear crystal surface. The tested BASF Lumogen F red 300 and Roehm 2466 P have maximum absorption at 440, 530-540 and 560-570 nm and the fluorescence emission at around 625 nm, where the quantum efficiency of photodiodes is higher. The WLS plate was coupled via an air gap of 0.5 mm to the crystal and one (and later two) S 3588-03 (mod 5400) photodi-

odes were coupled to the lateral faces of the WLS plate. The rear face of the WLS was covered with Tyvec and the lateral faces were painted with reflective paint NE 561. The photoelectron yield with two photodiodes increased by a factor 1.5 compared to photoelectron yield with one diode. The readout with two diodes reaches a maximum photoelectron yield of 5900 photoelectrons/MeV.

For very small CsI:Tl scintillators the readout with PIN diodes is competitive to the PMT readout. Kim et al. [59] reported energy resolutions of 7.9 % at 662 keV and 4.9 % at 1330 keV with a 1x1x2 cm^3 CsI:Tl crystal and a 1x2 cm^2 Hamamatsu 3590-08 diode.

A mismatch of the readout area and the crystal face reduces the number of detected photons. Liu et al. [32] measured the energy resolution of CsI:Tl crystals of 2.54 cm diameter and 2.54 cm length with a PMT with bialkali photocathode (29 cm diameter) and a diode readout (Hamamatsu S2744-08 with Canberra 2006 pre-amplifier). There the FWHM resolution at 662 keV was 8.4 % with the PMT and 14.3 % with the diode. The electronic noise threshold also increases form $\approx$ 10 keV for the PMT to $\approx$ 100 keV for the PD. They established that the combined electronic noise of the 2x1 cm^2 diode (Hamamatsu S2744-08) and the Preamplifier (Canberra) is 580 photoelectrons. For experiments with events on the keV range, PMTs give a superior performance due to their low noise level of a few photoelectrons (pe).

The TEXONO collaboration developed 40 cm long CsI:Tl crystals with a hexagonal front and rear side of 2 cm edge length. They achieved a FWHM resolution of 11 % at 660 keV with a PMT readout at the front and rear side of the crystal. A longitudinal position resolution of 2 cm was possible by analyzing the ratio of the difference of both PMT signals ($Q_1 - Q_2$) and the sum of both signal ($Q_1 + Q_2$) [32]. Also, Deniz et al. [57] reported for the TEXONO collaboration obtained more than 99 % γ/α discrimination down to about 100 keV, a resolution of 4 % root mean square (RMS)and less than one cm position resolution at 660 keV.

Bernabei et al. [37] obtain 5.5 to 7.5 pe/keV with a 9.7 kg NaI:Tl crystal (10.2x10.2x25.4 cm^2) couplet to two PMTs. This corresponds to a resolution of 4.5 % sigma at 662 keV..

The KIMS Collaboration uses CsI:Tl crystal of 8x8x23 cm^3 with two low background quartz window PMTs with PbCs photocathode. The PMTs with PbCs photocathode yield with, 5.5 pe/keV, 50 % more photoelec-

trons than a standard PMT with bialkali photocathode [42]. The collaboration reported in [55] the resolution of a 8x8x30 cm^3 (8x8x23 cm^3) crystal coupled to two PMTs (9269A from Electron Tube Ldt., PbCs photocathode, quartz window) as 3.5 % (4.6 %) RMS at 662 keV with a photoelectron yield of 5.6 (4.5) pe/keV. Kim et al. [43] report further resolution (RMS at 662 keV) ranging from 4.0 to 5.6 % of crystal with a length of 30 cm and front and rear surfaces ranging from 55x55 to 70x70 cm^2, using two 3-in Pmts (ET D726UK).

Renker [60] reported energy resolutions of scintillation detectors with APD for LSO crystals of 12.1 % FWHM, 22.4 % FWHM for BGO at 511 keV and 4.3 % FWHM with YAP:Ce crystals at 662 keV.

Ikagawa et al. [61] CsI:Tl 10x10x10 mm^3 with Hamamatsu APD S8664-1010N (10x10 mm^2) reached 4.9 % FWHM at 662 keV in comparison with 5.9 % (FWHM at 662 keV) with the PMT R7899EG (Hamamatsu, 1 inch diameter). 28 primary pe/keV were produced in APD. Ikagawa et al. [61] reported that APD can efficiently detect weak scintillation light of big crystals, even if the scintillator and APD size do not match. They couple an APD via a light guide to the rear face of a 48x3x300 mm^3 big BGO plate and reached a energy resolution of 20.9 % (FWHM at 662 keV and -20°) in comparison to 7.1 % (FWHM at 662 keV and -20°) for a 10x10x10 mm APD and an equal APD. At room temperature (20°) the APD readout of the small BGO crystals showed a resolution of 8.3 % and 10.4 % for the PMT readout (FWHM at 662 keV). Asano et al. [62] CWO crystal (5x5x5 mm^3) with APD (Hamamatsu S8664-55, 5x5 mm^2) and Hamamatsu PMT (R6231HA). Best results were obtained at -30°C with 6.4 and 7.0 % (FWHM at 662 keV). At 20° the APD and PMT had resolutions of around 9.2 and 7.6 % (FWHM at 662 keV).

Appendix B

SECOND APPENDIX

Further plots of ranges of photons discussed in chapter 5.1.1—"Scintillator size" are shown in the next section. A short description of the Geant4 toolkit, Venom and the Scint64 package is given in B.2—"Geant4".

B.1 Scintblock

In figure B.1-B.8 the peak and total absorption efficiencies of NaI, CsI, BGO and CWO for photons of different energies are shown. The derived efficiencies are discussed in chapter 5.1.1—"Scintillator size".

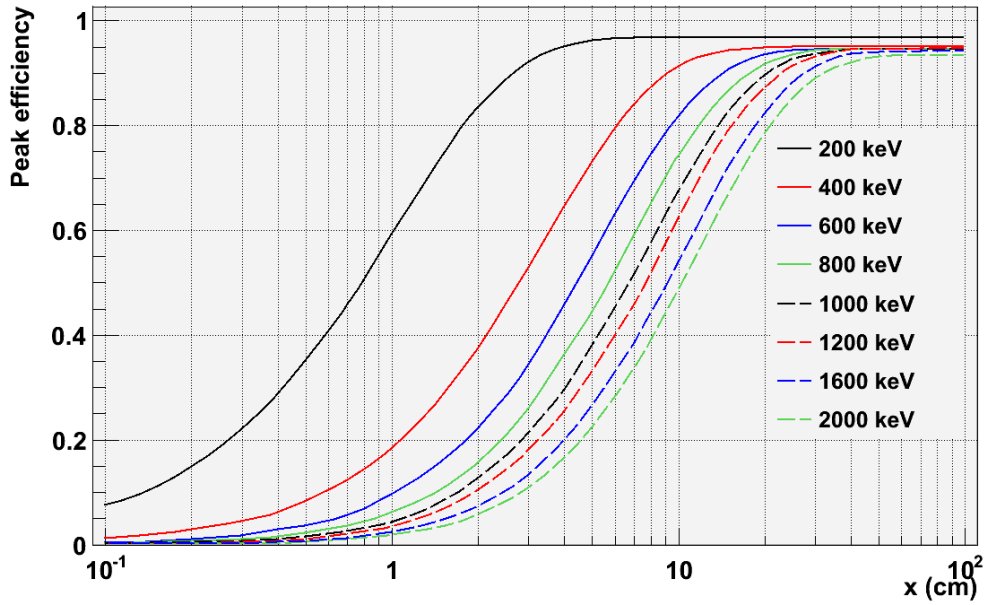

Figure B.1: Amount of events with absorbed full energy of monochromatic photons after various width of NaI.

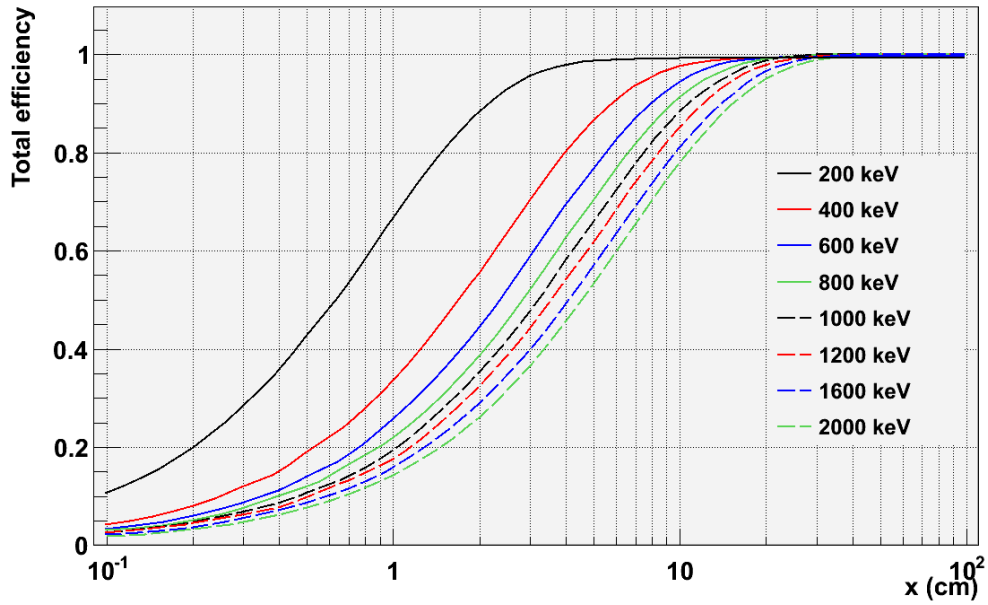

Figure B.2: Total amount of absorbed monochromatic photons after various width of NaI.

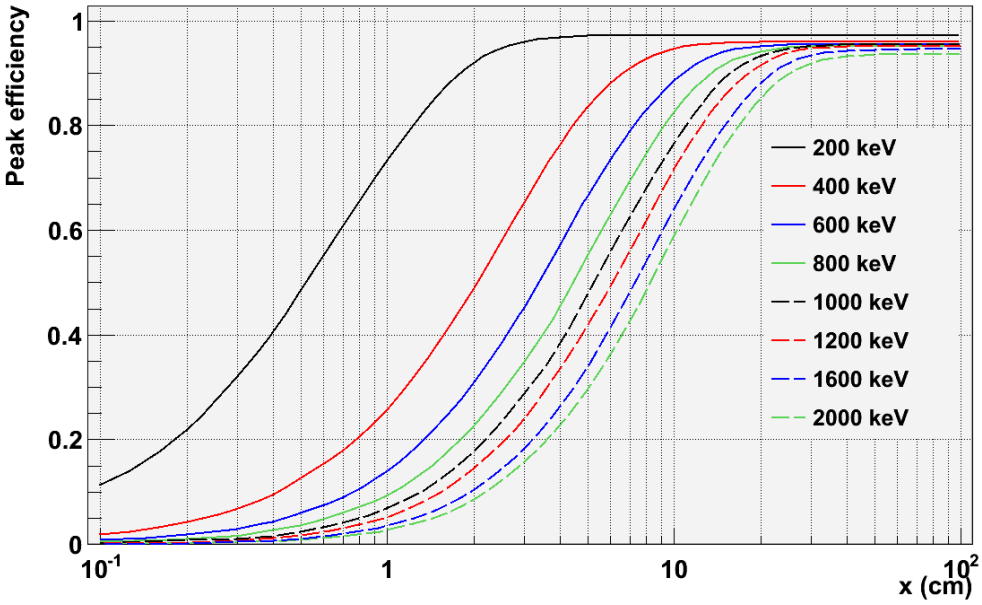

Figure B.3: Amount of events with absorbed full energy of monochromatic photons after various width of CsI.

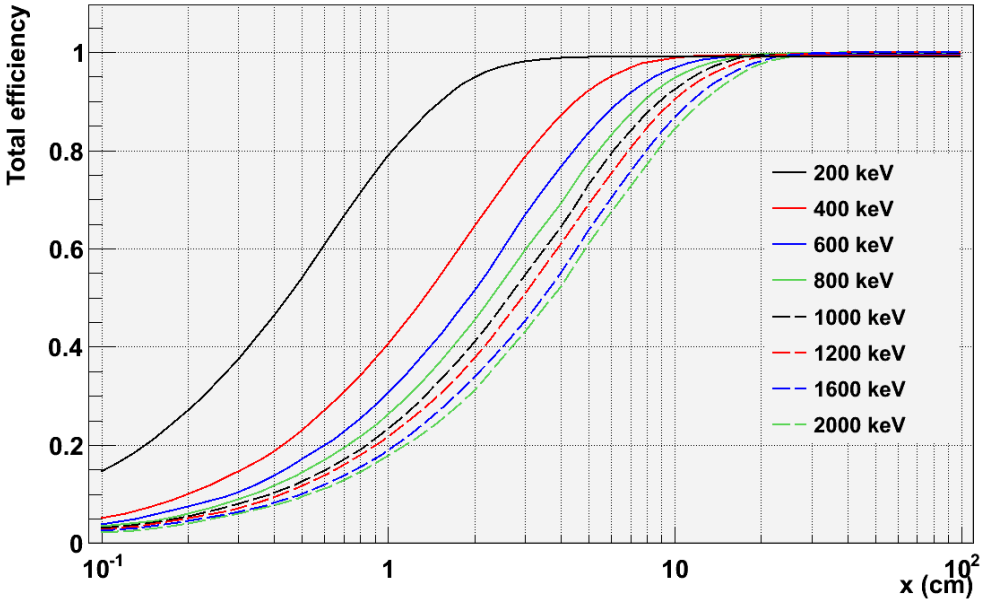

Figure B.4: Total amount of absorbed monochromatic photons after various width of CsI.

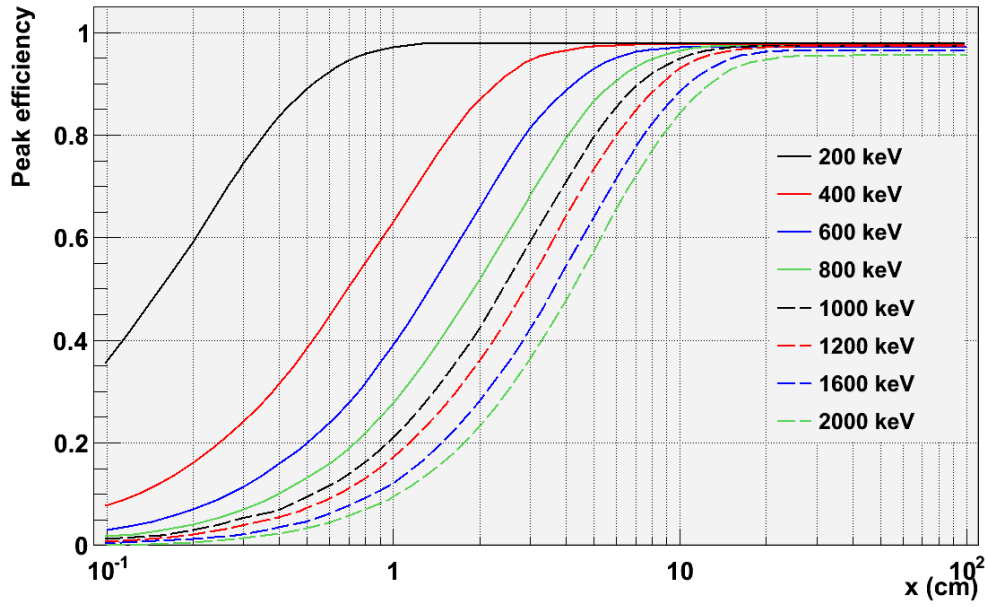

Figure B.5: Amount of events with absorbed full energy of monochromatic photons after various width of BGO.

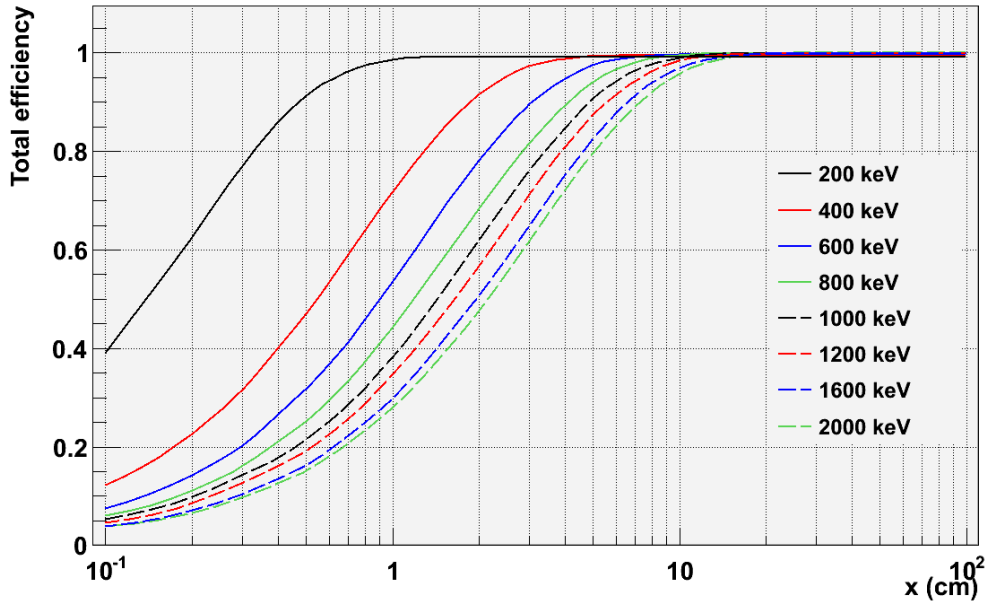

Figure B.6: Total amount of absorbed monochromatic photons after various width of BGO.

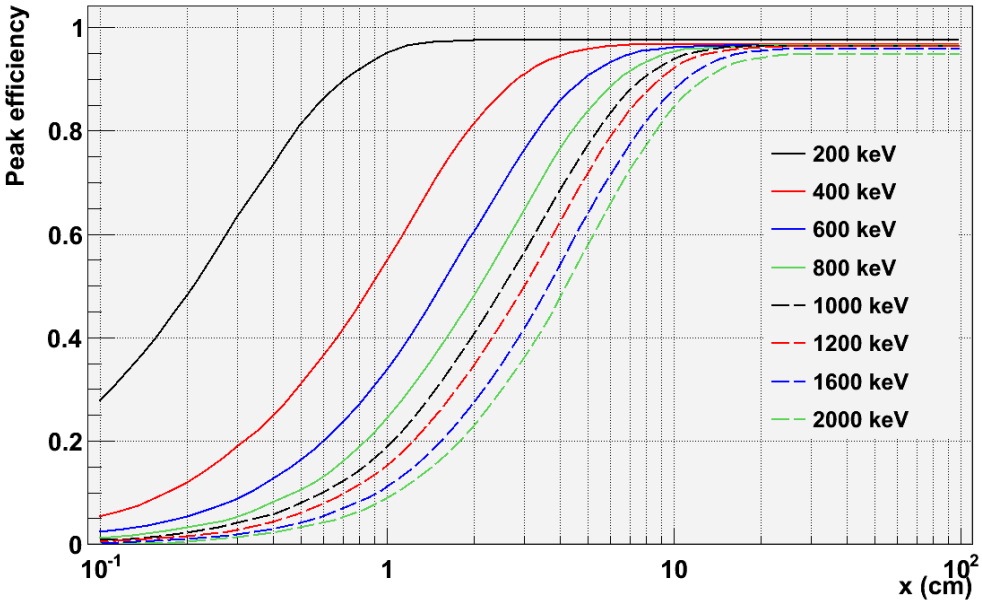

Figure B.7: Amount of events with absorbed full energy of monochromatic photons after various width of CWO.

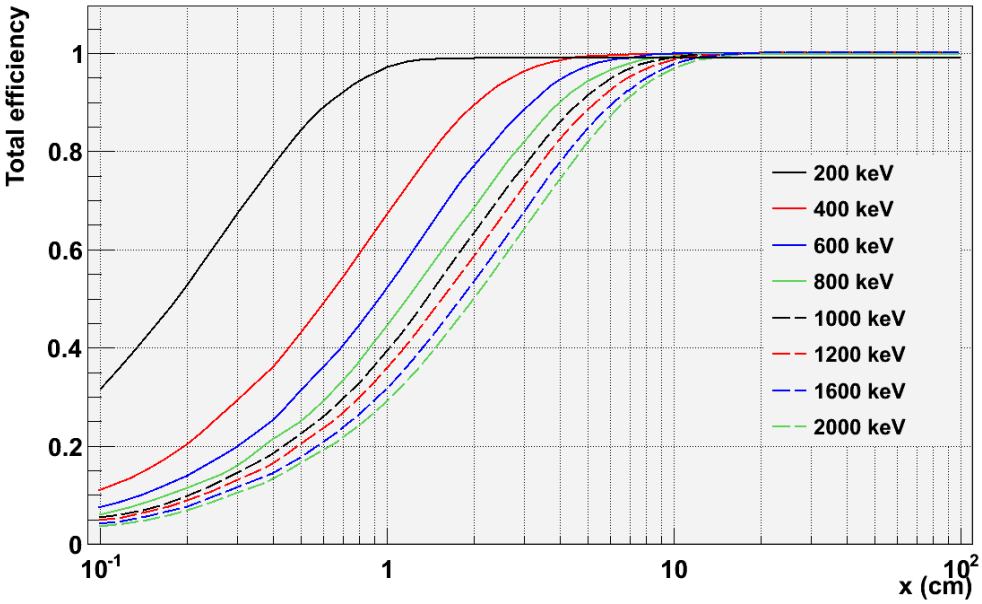

Figure B.8: Total amount of absorbed monochromatic photons after various width of CWO.

B.2 Geant4

Geant4 is an object-oriented toolkit for the simulation of the passage of particles through matter, written in C++. It provides a realistic reproduction of physical processes for an energy region from 250 eV up to a few GeV. The necessary cross sections for the simulations are interpolated from stored values in evaluated databases. The final state depends on the angle and energy distributions and will be calculated with the corresponding theoretical model or interpolated from the database [44].

A main method with two toolkit classes (G4Runmanager and G4UImanager) and three classes, which are derived from toolkit classes (G4Detectorconstruction, G4PhysicsList and G4PrimaryGeneratorAction) are required for building a simulation. The G4Runmanager controls the flow of the program. It manages the initialisation procedures like detector construction, definition of particles and physics processes or initialisation of primary particles. In the user initialised class DetectorConstruction, the geometry and material of the detector are defined by the user.

In the PhysicsList, the user defines the particles and physical processes, which shall be regarded. The initial state of the event is defined with the PrimaryGeneratorAction. This implies the particle type, energy, position, direction and number of initialised particles. A RUN is defined as a set of events. The user has control at the Begin and End of each run (class RunAction), the Begin and End of each event (class EventAction), the begin and End of each track (class TrackingAction) and at the End of each step (class SteppingAction). A HIT is a record, track per track (and even step per step), of a set of user defined information needed to simulate and analyse the detector response. Only interactions in volumes, specified as sensitive detectors can be handled as hits and be stored in the HitsCollection. The HitsCollection is printed at the end of event (via the method TrackerSD::EndOfEvent()), under the control of the command:`/hits/verbose 1`. A visualisation of the event is possible with the G4VisManager. Used visualisation systems are OpenGL, Heprep or Dawn. Geant4 applications can run in batch mode, where macro commands, being read at the beginning of a run, can be used. An interactive mode, driven by command lines or via a graphical user interface is also possible. [48]

VENOM is the Cobra simulation framework, first developed by H. Kiel [8] and redesigned by J. Wilson and B. Morgan [53]. It is a

Geant4 application, enabling reproducible simulations of signal and background physics processes in the detector for all COBRA collaborators. Venom contains packages, which can be added and extended by the user. All packages use the same physics class (`VXPhysicsList`) and material class (`VXMaterials`). Geometry, action, readout and generator classes can be added by writing new packages. Venom uses factory classes to enable runtime configurations of the geometry, the run action, the data readout and the event generator. A granular build system makes compiling of individual packages possible before linking them to the main application. The main application contains the `VXDetectorConstruction`, `VXPrimaryGeneratorAction`, `VXPhysicsList`, `VXVisManager` and `VXActionManager` classes. This is the minimal set of classes required by Geant4 to run. The `VXDetectorConstruction` constructs the `VXMaterials` class and only places the world logical volume. The construction of the world logical volume and all subvolumes is performed by `VXVGeoComponent`. This is an abstract base class, which places the component, and again leaves the construction of the components (which can consist of subcomponents) to their individual classes. The `VXPrimaryGeneratorAction` generates the primary events. The particle guns Decay0, Bkkgen, Chaingen and GPS can be chosen by using the `SetPrimaryGenerator()` method. The particle gun Decay0 uses the input files of the Decay0 software, initialising the energy and angular distributions of the electrons, positrons of gamma rays of double beta decays. The Bkkgen initialises decays of single isotopes, whereas Chaingen sets decays belonging to decay chains and GPS initialises particles. The `VXVisManager` is a standard visualisation manager supporting OpenGl, Heprep and Dawn. The `VXActionManager` allows to change run, event, stepping, stacking and tracking action classes at run time.
Venom provides no time information. The deposited energy in each sensitive detector volume is written to a Root file. The Array64 Root output file consist of a tree containing four leaves, the deposited energy edep, the shelf-ID and board-ID (used for K64Array) and the crystal ID. The crystal Id ranges from 1 to 16 and the shelf-ID from 1 to 4.

THE SCINT64 PACKAGE was written as part of this diploma thesis. It is a new Venom package, constructing the previously described simplified scintillator upgrade.

The Scint64 package uses the class `array64paintedcrystal` from the Array64 package and contains the classes `scint64Nest`, `scint64Scintillator`, `scint64PaintedScintillator`, `scint64ScintillatorCube`, `scint64PaintedScintillator-`

Cube, scint64ScintillatorHolder and scint64Shield.
In the centre of the detector is the scint64Nest, which contains 64 array64paintedcrystal volumes. They are placed on delrin holders in a delrin box with one open side and a wall thickness of 2 mm. The Nest parameters can be changed as in the Array64 package with a /scint64/nest/ command.
The scint64Scintillator and scint64ScintillatorCube are classes, defining a 5x5x20 and 5x5x5 cm^3 volume of CsI. The classes scint64PaintedScintillator and scint64Painted-ScintillatorCube contain the scint64Scintillator or scint64ScintillatorCube volumes, reflector and PMT volumes. The scint64PaintedScintillator volumes contain beside the scint64Scintillator volume, four reflector volumes of MgO (20x5x0.05 cm^3) and two borosilicate glass volumes (5x5x0.2 cm^3) representing PMT windows. The scint64PaintedScintillator-Cube contains five reflector volumes and only one PMT window volume.
The class scint64ScintillatorHolder contains the subcomponents scint64PaintedScintillator and scint64Painted-ScintillatorCube. All scintillator volumes are placed with the PMT window volumes facing the front and back side of the assembly.

The scint64ScintillatorHolder and scint64Nest volumes are finally contained in the scint64Shield class. The scint64Nest is placed in the middle standing upon two scint64Painted-Scintillator volumes. The scint64ScintillatorHolder sourrounds the scint64Nest. Then one 5 cm thick copper and one 10 cm thick lead layer are constructed and placed around the scint64-ScintillatorHolder. The final dimensions of this assembly are 51.4 x 51.4 x 50.6 cm^3. The material and thickness of the Cu and Pb shielding can be changed with the commands /scint64/Cuwidth and /scint64/Pbwidth.

Scint64 uses the default data structure for the CZT crystals and a slightly shorter output for the scintillators. The classes scint64Scintillator and scint64ScintillatorCube have own sensitive detector classes and data classes. The final Root output file holds three trees, containing the array64crystal data, the scint64Scintillator data and the scint64ScintillatorCube data. The latter two Root trees have each three branches, storing the deposited energy, the the scintillator ID (ranging from 1 to 20) and the type of the ionizing particle. Each event is stored in one vector and the information of different detectors are stored as vector components of the corresponding event.

The vectors of one event have the same length in all three branches, connecting the vector components bijective with the other branches. The `scint64Scintillator` houses the data of scintillators with the scintillator ID 1-5, 10, 11 and 16-20. The `scint64ScintillatorCube` data contains the scintillator IDs 6-9 and 12-15.
The kind of ionizing particle is important for the particle dependent scintillator response. It determines the signal height and form of the scintillation detector response. 99 % of all alpha particles in the CsI scintillator can be identified with a pulse shape discrimination [32]. The particle type information can therefore be used to veto the majority of all alpha decays in the scintillator volume. In this package, the quenching of the scintillation light output for alpha particles is also considered and used a Birks factor of $kB = 2.3 \cdot 10^{-3}$ gMeV^{-1}cm^{-2} as reported by Tretyak [31]. At run time a for alpha particles, according to their stopping power, reduced energy is added after each step to the Hitscollection.

Bibliography

[1] Kai Zuber. *Neutrino Physics*. Institude of Physics Publishing, 2004. ISBN 0-7503-0750-1.

[2] `http://pdg.lbl.gov`; visited on Sep 5th 2010.

[3] M. Hirsch, K. Muto, T. Oda, and H. V. Klapdor-Kleingrothaus. Nuclear structure calculation of $\beta^+\beta^+$, β^+/EC and EC/EC decay matrix elements. *Zeitschrift fur Physik A Hadrons and Nuclei*, 347:151–160, 1994.

[4] W. Pauli. Brief an die Radioaktiven. 1930.

[5] F. Reines and C. L. Cowan. Detection of the free neutrino. *Phys. Rev.*, 92(3):830–831, 1953.

[6] Raymond Davis, Don S. Harmer, and Kenneth C. Hoffman. Search for neutrinos from the sun. *Phys. Rev. Lett.*, 20(21):1205–1209, 1968.

[7] M. Goeppert-Mayer. Double beta-disintegration. *Phys. Rev.*, 48(6): 512–516, 1935.

[8] H. Kiel. *Determination of the half lives of rare decays of Cd, Te and Zn isotopes for the COBRA experiment*. PhD thesis, University of Dortmund, Germany.

[9] W. C. Haxton and G. J. Stephenson. Double beta decay. *Progress in Particle and Nuclear Physics*, 12:409–479, 1984.

[10] W. H. Furry. On transition probabilities in double beta-disintegration. *Phys. Rev.*, 56(12):1184–1193, 1939.

[11] Kai Zuber. Personal communication. Technical University Dresden, 2009.

[12] A. Piepke et al. Investigation of the $\beta\beta$ decay of ^{116}Cd into excited states of ^{116}Sn. *Nuclear Instruments and Methods in Physics Research Section A*, 577:493, 1994.

[13] H. V. Klapdor-Kleingrothaus et al. Latest results from the HEIDELBERG-MOSCOW double beta decay experiment. *European Physical Journal A*, 12:147–154, 2001.

[14] H. V. Klapdor-Kleingrothaus, I. V. Krivosheina, A. Dietz, and O. Chkvorets. Search for neutrinoless double beta decay with enriched ^{76}Ge in Gran Sasso 1990-2003. *Physics Letters B*.

[15] Hiroyasu Ejiri. Double beta decays and neutrino nuclear responses. *Progress in Particle and Nuclear Physics*, 64(2):249–257, 2010.

[16] Richard B. Firestone. *Table of Isotopes*. Teubner-Studienbcher, 1996. ISBN 3-519-03058-6.

[17] G. Anton et al. Cobra progress report, 2009.

[18] G. Heusser. Low-radioactivity background techniques. *Annual Review of Nuclear and Particle Science*, 45:543–590, 1995.

[19] C. Reeve. *Data analysis and background studies for the COBRA neutrinoless double-beta decay experiment*. PhD thesis, University of Sussex, Brighton, UK, 2009.

[20] Daniel Münstermann. Measurements of the Rn concentration within the COBRA cabin at LNGS, 2009. COBRA note # 2009-a.

[21] Sandra Oehl. A shielding system against neutrons fo the COBRA-experiment and characterisation of CdZnTe detectors with the Transient current technique. Diploma thesis, Universität Dortmund, 11 2004.

[22] S. Nisi. Semi qualitative analysis on CdZnTe-crystal. COBRA memo, 2007.

[23] Daniel Gehre. Personal communication. Technical University Dresden, 2010.

[24] J. V. Dawson et al. Cobra progress report, 2007.

[25] P. N. Luke. Unipolar charge sensing with coplanar electrodes application to semiconductor detectors. *IEEE Trans. Nucl. Sci*, 42:207–213, 1995.

[26] Paul Lecoq et al. *Inorganic Scintillators for Detector Systems*. Springer-Verlag, 2006. ISBN 978-3540277668.

[27] John B. Birks. *The Theory and Practice of Scintillation Counting*. Pergamon Press, 1964.

[28] William R. Leo. *Techniques for Nuclear and Particle Physics Experiments: A How-to Approach*. Springer-Verlag, 1994. ISBN 978-3540572800.

[29] Glenn F. Knoll. *Radiation Detection and Measurement*. John Wiley & Sons, Inc., 2000. ISBN 978-0471073383.

[30] Konrad Kleinknecht. *Detektoren für Teilchenstrahlung*. Teubner-Studienbücher, 1984. ISBN 3-519-03058-6.

[31] V. I. Tretyak. Semi-empirical calculation of quenching factors for ions in scintillators. *Astroparticle Physics*, 33:40–53, 2010.

[32] Y. Liu et al. Studies of prototype CsI(Tl) crystal scintillators for low-energy neutrino experiments. *Nuclear Instruments and Methods in Physics Research Section A*, 482:125–143, 2002.

[33] L. E. Dinca et al. Alpha-gamma pulse shape discrimination in CsI:Tl, CsI:Na and BaF_2 scintillators. *Nuclear Instruments and Methods in Physics Research Section A*, 486(1-2):141–145, 2002.

[34] M. S. Zucker and N. Tsoupas. An n-gamma pulse discrimination system for wide energy ranges. *Nuclear Instruments and Methods in Physics Research Section A*, 299:281 – 285, 1990.

[35] E. Armengau et al. Proceedings of the 1st International Workshop 'Radiopure Scintillators for EURECA' (RPScint'2008). 2009.

[36] `http://www.detectors.saint-gobain.com/MaterialsGasTubes.aspx`; visited on Jan 14th 2010.

[37] R. Bernabei et al. The DAMA/LIBRA apparatus. *Nuclear Instruments and Methods in Physics Research Section A*, 592:297–315, 2008.

[38] Y. N. Zheng et al. *Inorganic Scintillators And Their Applications: Scint'95*, page 247, 1996.

[39] J. Brose, G. Dahlinger, and K. R. Schubert. Properties of CsI(Tl) crystals and their optimization for calorimetry of high energy photons. *Nuclear Instruments and Methods in Physics Research Section A*, 417:311–324, 1998.

[40] `http://www.refractiveindex.info`; visited on July 1th 2010.

[41] `http://www.hamamatsu.de`; visited on Jan 14th 2010.

[42] H. S. Lee et al. First limit on WIMP cross section with low background CsI(Tl) crystal detector. *Physics Letters B*, 633:201–208, 2006.

[43] T. Y. Kim et al. Study of the internal background of CsI(Tl) crystal detectors for dark matter search. *Nuclear Instruments and Methods in Physics Research A*, 500:337–334, 2003.

[44] Geant4.9.2. Physics Reference Manual; 2008.

[45] `http://www.helgesonsa.es/m02/firmas/SCIONIX/index.html`; visited on Jul 23th 2010.

[46] Yan V. Vsiliev. Nikolaev Institute of Inorganic Chemistry, Chrystal Production Lab, viv@che_nsk.su, personal communication (2009).

[47] Yue Qian. yueq@mail.tsinghua.edu.cn, personal communication (2009).

[48] Geant4.9.2. User Manual; 2008.

[49] `http://www.lcsim.org/software/geant4/doxygen/html/classes.html`; visited on Jul 7th 2010.

[50] Edward D. Palik. *Handbook of optical constants of solids*. Academic Pr., 1991. ISBN 0-12-544422-2.

[51] Joachim Ebert. Personal communication. University Hamburg, 2010.

[52] C. Cozzini et al. Cobra progress report spring, 2005. Submitted to LNGS scintific comittee.

[53] The COBRA Collaboration. *The Venom Simulation Framework for COBRA*, 2007.

[54] Marcel Heine. Eine Suche nach Doppelbeta-Zerfällen von Cadmium-, Zink- und Tellur-Isotopen mit Positronen-Emission. Diploma thesis, Technische Universität Dresden, 12 2009.

[55] H. S. Lee et al. Development of low-background CsI(Tl) crystals for WIMP search. *Nuclear Instruments and Methods in Physics Research Section A*, 571:644–650, 2007.

[56] Y. D. Kim et al. Inhibition of contamination in cesium iodide. *Nuclear Instruments and Methods in Physics Research Section A*, 552:456–462, 2005.

[57] M. Deniz et al. Measurement of neutrino-electron scattering cross-section with a CsI(Tl) scintillating crystal array at the Kuo-Sheng Nuclear Power Reactor. *Phys. Rev.*, D81:072001.

[58] J. Wilson. Contamination measurements of materials used in COBRA. COBRA memo, 2006.

[59] H. S. Kim et al. Fabrication and performance characteristics of a CsI(Tl)/PIN diode radiation sensor for industrial applications. *Applied Radiation and Isotopes*, 67:1463–1465, 2009.

[60] Dieter Renker. Properties of avalanche photodiodes for applications in high energy physics, astrophysics and medical imaging. *Nuclear Instruments and Methods in Physics Research Section A*, 486: 164–169, 2002.

[61] T. Ikagawa et al. Study of large area hamamatsu avalanche photodiode in a γ-ray scintillation detector. *Nuclear Instruments and Methods in Physics Research Section A*, 538(1-3):640 – 650, 2005.

[62] S Asano et al. Soft gamma-ray detector using CdWO4/ZnWO4 crystal with avalanche photodiodes. *Nuclear Science Symposium Conference Record, 2005 IEEE*, 3:1356–1359.

Typeset September 29, 2010